Title

K- -Neutron Elastic Scattering from K-d ®-K-d and K-d® K-pn at 1 BeV/C

Author

Jew, Nathan Nay Shew

Publication Date

1969-10-01

UCRL-19359

cy. 2

K^--NEUTRON ELASTIC SCATTERING FROM $K^-d \to K^-d$ AND $K^-d \to K^-pn$ AT 1 BeV/c

Nathan Nay Shew Jew
(Ph.D. Thesis)

October 1969

AEC Contract No. W-7405-eng-48

LAWRENCE RADIATION LABORATORY
UNIVERSITY of CALIFORNIA BERKELEY

UCRL-19359
cy. 2

DISCLAIMER

Contents

K^--NEUTRON ELASTIC SCATTERING FROM $K^-d \to K^-d$ AND $K^-d \to K^-pn$ at 1 BeV/c

Nathan Nay Shew Jew

Lawrence Radiation Laboratory
University of California
Berkeley, California

October 1969

ABSTRACT

We present experimental angular distributions for $K^-d \to K^-d$ and $K^-d \to K^-pn$ at incident K^- momenta of 810, 910, 1010, and 1110 MeV/c. These distributions are analyzed simultaneously in terms of free nucleon scattering parameters, using Glauber's impact parameter formalism as starting point. This formalism was modified to make it applicable to our data, which contained a proton momentum cut made during scanning. In addition, we incorporated into our analysis two other modifications to this formalism. One of these arose from the difference in flux factors between K^-d and K^--nucleon scattering, the other from the smearing of the nucleon cross-sections due to Fermi momentum. Finally, this formalism was extended to include spin dependence. The method of analysis required both the K^-p and K^-n elastic scattering amplitudes. We input the K^-p amplitudes from two models based on experiment. These were held fixed during the fitting. We then parametrized the K^-n amplitudes and fitted our data by varying the K^-n parameters to get a minimum for the fitting χ^2. The analysis included both the single and double scattering effects.

I. INTRODUCTION

We present here a bubble chamber study of K^--deuteron scattering at four K^- momenta: 810, 910, 1010, and 1110 MeV/c. We study both the elastic scattering reaction and the reaction in which the K^- breaks up the deuteron into a neutron and a proton. Out of the 219 000 pictures scanned, we obtained 44 000 2-prong events. After applying selection criteria to these, we have a total of 7800 elastic scattering events and 24 000 break-up events. These numbers are for the four incident momenta combined.

We analyze our data samples simultaneously in terms of free nucleon scattering parameters, using Glauber's impact parameter formalism to do this. We need to modify this formalism to make it applicable to our data, which contain a proton momentum cut made during scanning. This cut affects the break-up reaction cross-section data. The modification to the break-up cross-section formula is obtained via a diagrammatic method. We find two other modifications which we incorporate into our fitting procedure. One of these arises from the difference in flux factors between K^-d and K^--nucleon scattering. The other arises from Fermi momentum smearing of the nucleon cross-sections. Finally, we extend this formalism to include spin dependence.

Our analysis require both the K^-p and K^-n elastic scattering amplitudes. We input the K^-p amplitudes from two models based on experiment. These are held fixed during fitting. We then parametrize the K^-n amplitudes and fit our data through a variation of the parameters in the K^-n amplitude to minimize the fitting χ^2. Our analysis also includes double scattering effects.

The contents of the main sections of this report consist of the

following. In Section II, we give the relevant details of the experimental procedure. In Section III, we present the impact parameter formalism for K^-d scattering, followed by modifications which are needed in order to apply this formalism to our data. We conclude this section with an extension of this formalism to include spin. In Section IV, we discuss the details of the procedure of analyzing our data. This includes the choice of a deuteron form factor, details of the K^-p elastic scattering models, the parametrization of the K^-n elastic scattering amplitudes, and the various steps of the fitting procedure. This section ends with a discussion of the results obtained in our analysis.

II. EXPERIMENTAL DETAILS

A. Collecting and Processing of Data

1. The K^- Beam

This experiment was done with a two-stage separated K^- beam, using the Lawrence Radiation Laboratory 25-inch bubble chamber as detector. The beam was designed to operate in the momentum range 800 to 1200 MeV/c. The K^- particles were produced from a copper target in the Bevatron external proton beam and were extracted at 0°. They were separated from the other particles by two stages of separation. The layout of the beam is shown in Fig. 1, and is described in Ref. 1. From a delta-ray count, the beam in the bubble chamber was found to contain between 90 and 95% K^- (depending on momentum). About 85% of the contamination was muons, the rest being pions. (See Section II-B.)

2. Scanning and Measuring

A total of 219,000 pictures were taken at incident K^- momenta of 810 MeV/c (23,000 pictures) 910 MeV/c (76,000 pictures), 1010 MeV/c (54,000 pictures), and 1110 MeV/c (66,000 pictures). We scanned for 2-prong events which had a positive track of projected length $\geq$ 1mm. About 1/2 the film (80%, 33%, 72%, 49% for the four incident momenta, respectively) was scanned with just this cut. The remaining half was scanned with the additional restriction that the positive track be of projected length $\leq$ 9 cm and hence must stop within the bubble chamber. The fiducial volume was such that apart from very steep tracks, the origins were more than 9 cm (projected on the scan table) from the chamber boundaries. The number of events found in the portion of the film scanned with no upper limit on the positive track length was about 2.3 times that of the other half. The lower cut was imposed to

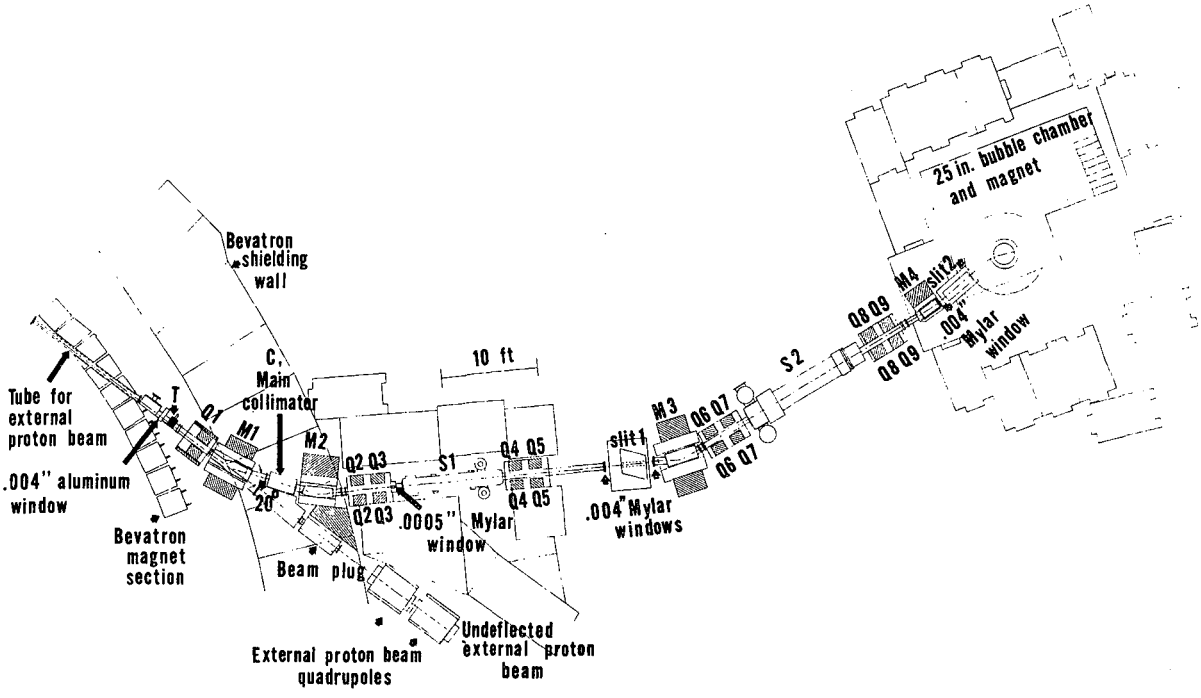
25 in. bubble chamber and magnet
Bevatron shielding wall
C, Main collimator
10 ft
Tube for external proton beam
.004" aluminum window
Bevatron magnet section
T
Q1
M1
M2
Q2 Q3
S1
Q4 Q5
slit 1
M3
Q6 Q7
S2
Q8 Q9
M4
slit 2
.004" Mylar window
20°
.0005" Mylar window
.004" Mylar windows
Beam plug
External proton beam quadrupoles
Undeflected external proton beam
MUB-3362

Fig. 1

avoid picking up counterfeit events, the short prong of which being really a low energy delta-ray. In the case of K^--deuteron elastic scattering, this cut limits our angular distributions to regions away from the forward direction ($-t \geq 0.02$ (BeV/c)^2). It presents no difficulties in our analysis of the elastic scattering data. However, in the case of the reaction in which the deuteron is broken up into a free proton and a free neutron, corrections must be put in to account for this cut. This point requires a modification of the theoretical formula we will use in our analysis. We discuss this in detail in Section III-B.

Due to the large number of events in the film containing a sigma and one other prong, and also due to the difficulty of measuring the momenta of short tracks from curvature, we rejected all events which had a scatter or kink occurring within the beginning 4 cm (projected) of the out-going tracks. From the known pd, dd, and K^-d total cross-sections, we estimate that this criterion rejected 4 ± 2% of the genuine events in the break-up reaction and 3 ± 2% in the K^-d elastic reaction.

Any event with a V pointing at the origin of the 2-prong interaction was rejected at the time of scanning. In cases of ambiguous origins, the event was accepted for measuring and fitting.

All the scanned film was used to obtain the K^-d elastic scattering cross-sections. The half of the film scanned with no upper limit imposed on the length of the positive track was used to obtain distributions for the break-up reaction. We also used this portion of film to check whether the upper limit on the length of the positive track made any difference in the K^-d elastic scattering angular distribution. The results showed that within our statistics the cut did not affect the distrubutions. Consequently, we used all the scanned film to get the

K^-d elastic scattering cross-sections without having to introduce a correction for this cut.

The scanning yielded a total of 44,000 2-prong events. These were then measured on the Franckenstein measuring system. About half of these events were measured before these measuring machines went under automatic computer control. The remaining half was measured with these machines under computer control provided by the COBWEB system.[2] The momenta of all stopping tracks were obtained from range measurements. Events that failed at either the measuring stage or the spatial re-construction stage were remeasured. We estimate that less than 1% of the scanned events were missing after the remeasurements.

3. Event Processing

The measured events were processed through the FOG-CLOUDY-FAIR system of geometry re-construction, kinematic fitting, and data selection computer programs.[3]

In the fitting procedure, we subjected each event to the following hypotheses:

$$K^-d \rightarrow K^-d$$
$$\rightarrow K^-pn$$
$$\rightarrow \pi^-p\Lambda \quad (\Lambda \text{ not seen})$$

The first of these is a 4-constraint fit (4-C), the second and third are 1-C fits. For each of these hypotheses, CLOUDY calculated a goodness-of-fit parameter M^*, which is defined as

$$M^* = \sum_{i=1}^{n} \left[\frac{x_i - x_i^m}{\Delta_i} \right]^2 - \sum_{\ell=1}^{4} \lambda_\ell F_\ell(x_j) \quad ,$$

where x_i are the parameters to be varied in the fitting procedure,

x_i^m the actual measured values corresponding to x_i, Δ_i the errors for x_i^m, λ_ℓ are Lagrangian multipliers, and F_ℓ the energy-momentum conservation constraints. In the case in which $\Sigma\lambda_\ell F_\ell$ is 0, M^* is the usual definition of a χ^2. This would be the case whenever the energy and momentum balance was satisfied to within the pre-set limits of 0.1 MeV and 0.1 MeV/c, respectively.

After processing the events through CLOUDY, various physical quantities of interest were abstracted and additional ones calculated in FAIR. This system of computer programs outputs the data in the convenient forms of histograms, scatter plots, lists, or tapes.

In addition to constraining the events to the three hypotheses mentioned above, we also constrained them to the following two hypotheses:

$$\pi^- d \rightarrow \pi^- d$$
$$\rightarrow \pi^- pn \quad .$$

This was done in an effort to estimate what fraction of the small pion contamination of the beam (see Section II-B) fitted the K^-d hypotheses.

B. Beam Flux Normalization

1. Beam Count

We used the track-counting method to obtain the normalization for the beam flux. The tracks of incoming particles were counted every fifty frames in each roll of film. The criteria by which we judged beam tracks were obtained from previously measured and constrained events of the type

$$K^- d \rightarrow \pi^- \Lambda\ (p) \quad ,$$

in which the Λ decay was seen. Using plots of these constrained events,

we determined the beam momentum bite and its azimuthal angular spread at the bubble chamber entrance window. Together with an exact knowledge of the position of the entrance window, this information enabled us to construct a beam track template for each incident momentum. Also included on the template was the start of the fiducial volume limits by which we accepted events. A track was counted as a beam track if it entered through the entrance window, was within the azimuthal angular acceptance at the entrance window, and reached the start of the fiducial volume without scattering or decaying. Bending of the beam particle tracks by the bubble chamber magnetic field was taken into account.

On the average 35 frames per roll were counted. The average number of beam tracks per frame was calculated. From this number we determined the total path length of the K^- tracks used in this experiment.

2. Beam Contamination

A number of corrections were made to the number of counted beam tracks obtained via the procedure described above. One was beam contamination from other particles. This contamination came from negative pions and muons. To determine the extent of this contamination, a delta-ray count was performed on the film taken in a companion hydrogen run which used the same beam conditions and at the same momenta as in this experiment.[4] Because of kinematics, an incident particle can produce delta-rays only up to a certain maximum momentum. This momentum is determined by the maximum kinetic energy T_{max} transferrable to the electron. In terms of the mass m of the incident particle and its momentum p, T_{max} is given by the formula[5]

$$T_{max} = 2\, m_e\, (p/m)^2 \quad ,$$

where m_e is the mass of the electron. In this delta-ray count, we recorded the number of delta-rays of momentum greater than the maximum that can be produced by a K^- at the given incident momentum. The number of tracks which interacted after producing such a delta-ray was also noted. As the muons do not interact strongly, these tracks can be assumed to be pions. From the number counted, we estimated that about 85% of the contamination came from negative muons, the remainder from negative pions. The results for the percentage of combined contamination at each momentum are shown in Table I. We have checked these results by doing a separate delta-ray count on 10% of the deuterium film used in this experiment. The results obtained agreed with the results of the delta-ray count on the hydrogen film.

3. Beam Attenuation

A second correction made on the beam count comes from the attenuation of the beam as it traverses the liquid in the bubble chamber. The main contribution to this attenuation comes from K^--deuteron scattering. The total cross-sections for K^- incident on deuterons have been accurately measured in counter experiments.[6] Within the momentum interval covered by our experiment, these total cross-sections range from 65 mb to 85 mb. (See Fig. 2.) The number of interactions in the K^-beam was thus expected to be large, thus appreciably depleting the number of beam tracks going through the entire bubble chamber. We corrected for this attenuation by using the measured values of the total cross-sections. From the values given in Ref. 6, we calculated the mean free path, using the formula

$$\lambda = \frac{1}{n\sigma_t} \quad ,$$

Table I. Normalization and correction factors.

Beam Momentum (Mev/c)	810	910	1010	1110
No. of Incident K^-:				
in K^-d ($\times 10^5$)	1.55	6.76	5.04	6.42
in K^-pn ($\times 10^5$)	1.10	2.21	3.63	3.20
π-μ Contamination (%)	4.9	6.0	5.3	9.1
Fid. Vol. Length (cm) (corrected for beam attenuation)	28.8	28.6	28.5	28.7
K^-d χ^2 Correction Factor	1.12	1.17	1.18	1.13
Scan Efficiency (%)				
for K^-d	97.9	96.8	97.3	96.5
for K^-pn	91.7	92.8	92.4	89.6

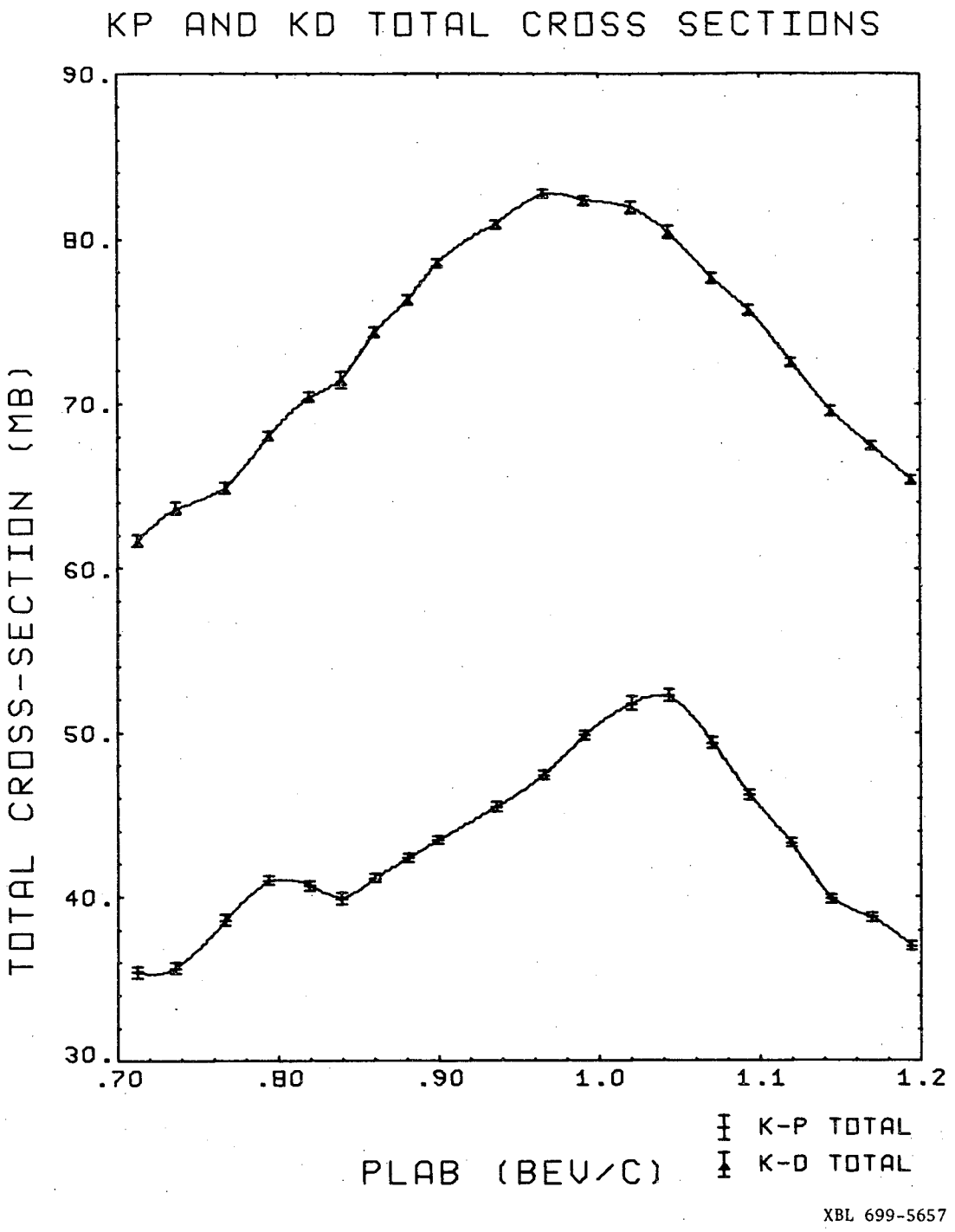

Fig. 2. K^-d and K^-p total cross-sections. The data points are from Ref. 6. The smooth curves are interpolations of the data points.

where σ_t is the total cross-section, n the number of scatterers per unit volume. In our case, the density of deuterium was 0.1352 gm/cm^3.[7] Together with Avogadro's number, this gives

$$\frac{1}{n} = 2.456 \times 10^4 \text{ cm-mb} \quad .$$

The average length a track goes before undergoing one interaction is given by

$$L = \lambda \, (1-e^{-\ell/\lambda}) \quad ,$$

where ℓ is the length of the interaction fiducial volume. In this experiment, the length of beam track within this volume was 30 cm. The track lengths corrected for beam attenuation at each incident momentum are shown in Table I. The corrections range from 4.1% in the case of 810 MeV/c events to a high of 5.8% for the 1010 MeV/c events, at which momentum the total cross-section is near the highest value for K^-d scattering.

C. Selection of Events

1. χ^2 Selection

Of the 44,000 two-prong events that came through the system of fitting programs, the break down into the number of events fitting the three interactions hypothese

$$K^-d \rightarrow K^-d \qquad \text{(H1)}$$

$$\rightarrow K^-pn \qquad \text{(H2)}$$

$$\rightarrow K^-p\Lambda \qquad \text{(H3)}$$

are displayed in Venn diagrams in Fig. 3. The criteria we used for these selections had been the χ^2 for each fit. In particular, we had used the

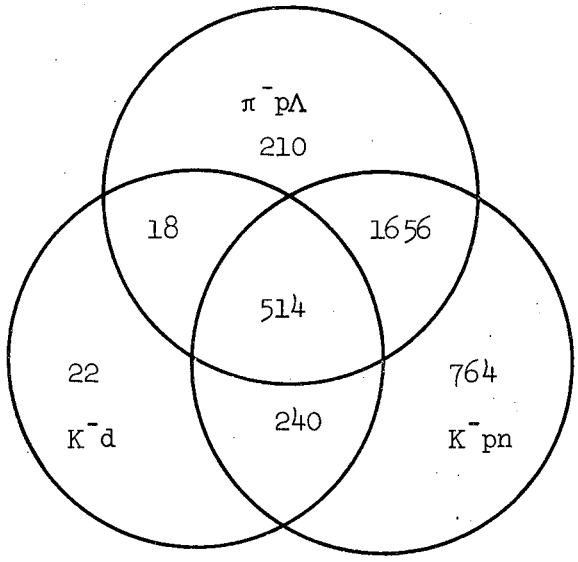

810 MeV/c

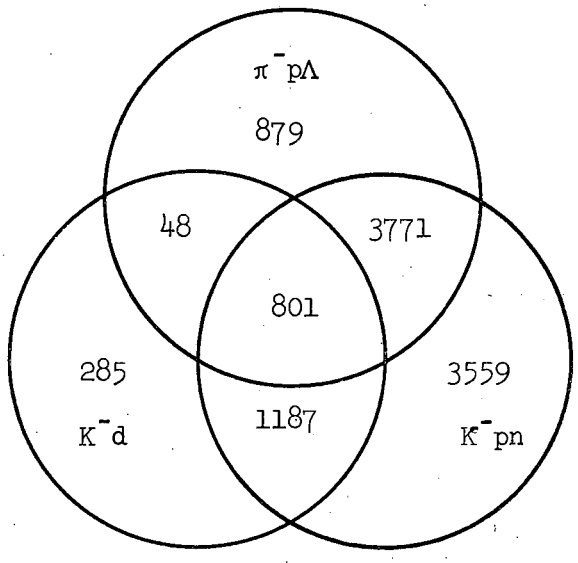

910 MeV/c

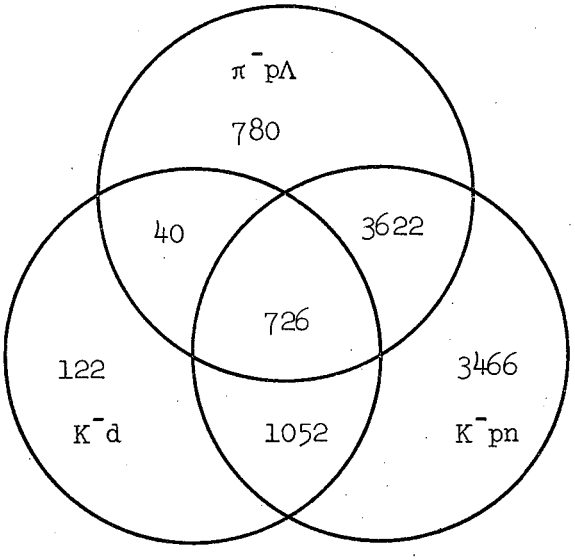

1010 MeV/c

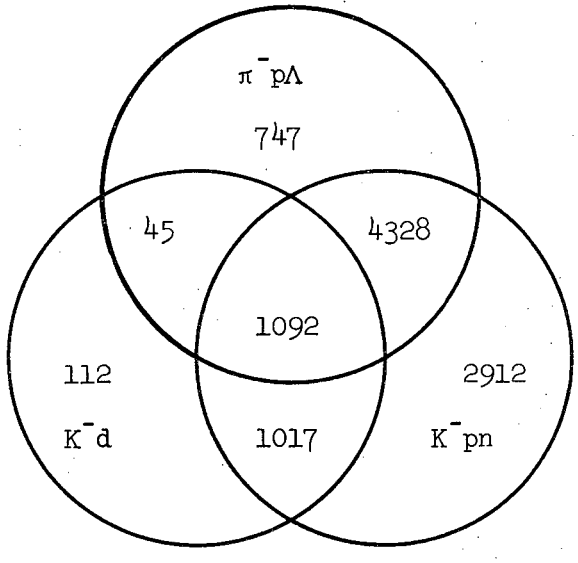

1110 MeV/c

Fig. 3. Break-down of the number of events fitting the different hypotheses.

following:

$$\chi^2 (K^- d) \leq 10 \quad , \quad 4C$$
$$\chi^2 (K^- pn) \leq 4 \quad , \quad 1C$$
$$\chi^2 (\pi^- p\Lambda) \leq 4 \quad , \quad 1C$$

These cut-off values for the χ^2 are the limits within which approximately 95% of the area under the theoretical χ^2 distributions are included.

As can be seen from the diagrams in Fig. 3, a majority of the events (~86% for the four momenta together) fitting the elastic scattering hypothesis also fit the $K^- pn$ hypothesis. This is not an unexpected result, since the deuteron can simulate the break-up reaction, with the neutron and the proton seen as going off in the same direction. When a deuteron is mistaken for a proton, or vice versa, range measurements give values for the momentum of the track which differ from the actual momentum by 60 to 100 MeV/c. But a one-constraint fitting hypothesis would not be able to distinguish this difference in the majority of cases. This is reflected in good χ^2 values for both hypotheses. The ionization is not of help in the identification either. Both the proton and the deuteron appear as solid, dark tracks in the range of momentum values with which they emerge from the interaction with the incident K^- particle. However, the elastic scattering reaction is a 4-constraint fitting hypothesis, whereas the break-up reaction has only one constraint. To get a sample of elastic events, we made the assumption that all the events fitting the elastic reaction are good $K^- d$ elastic scattering events. In order to include as few break-up events as possible in this sample, we made use of an additional handle. As noted above, the deuteron can simulate the break-up reaction, but only with the proton and neutron seen going off in nearly the same direction. This

means that the angle between the proton and the neutron, when the events are put through the break-up hypothesis, should be around 0° for genuine elastic scattering events. The real break-up events should have a uniform distribution in this angle, since in this case the neutron and the proton are not strongly correlated. In Fig. 4, we have plotted the distribution of events as a function of the cosine of the angle between the proton and the neutron for the K^-d elastic scattering events obtained with just the χ^2 cut applied to all the events that came through the system. We note that almost all the events (~84%) fall within the interval between 0.9 and 1.0. As our final sample of K^-d elastic scattering events we took only the events in the interval between 0.5 and 1.0. These were subsequently corrected for biases and losses (to be considered below). The resulting angular distributions were then used in our analysis.

As our sample of break-up events, we took all the events that satisfied hypothesis H2 (as determined by the χ^2) and subtracted out those that also fitted the K^-d elastic scattering criteria described above. In Fig. 5, we have plotted the histograms of the cosine of the angle between the proton and the neutron for these events. The excess of events in the forward boxes represents K^-d elastic scattering events which have a $\chi^2 > 10$ for hypothesis H1. These large χ^2 events occur at small momentum transfers in the break-up distributions. We removed this contamination by using only the part of the break-up distribution above $-t = 0.06$ $(\text{BeV}/c)^2$ in our analysis. Since our analysis takes into account break-up events regardless of the length of the proton track, we have included in our sample of $K^-d \rightarrow K^-pn$ events only those from film scanned with no upper limit on the length of the outgoing proton track.

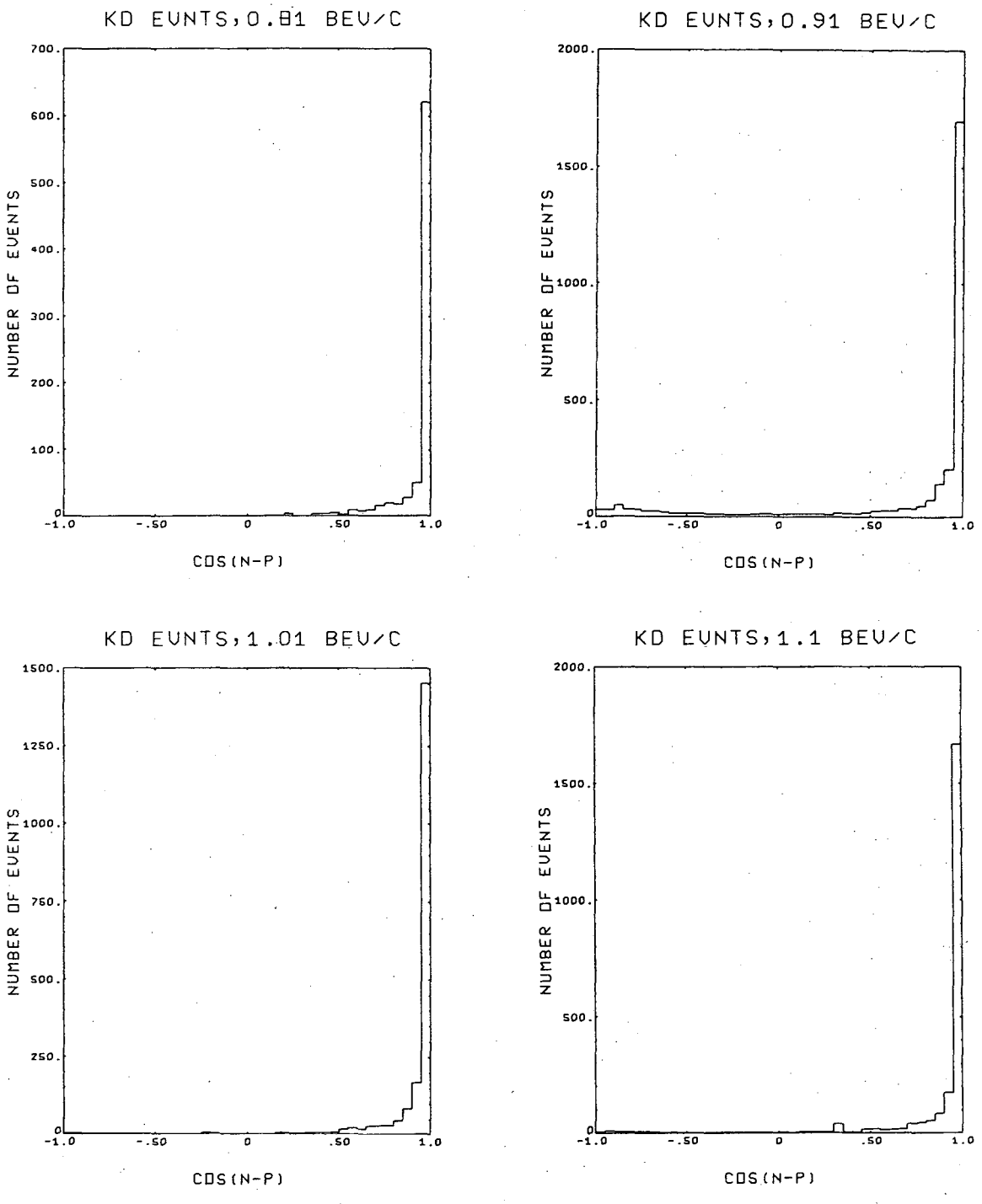

XBL 699-5647

Fig. 4. Histograms of the cosine of the angle between the proton and the neutron for K^-d elastic scattering events going through the $K^-d \rightarrow K^-pn$ hypothesis.

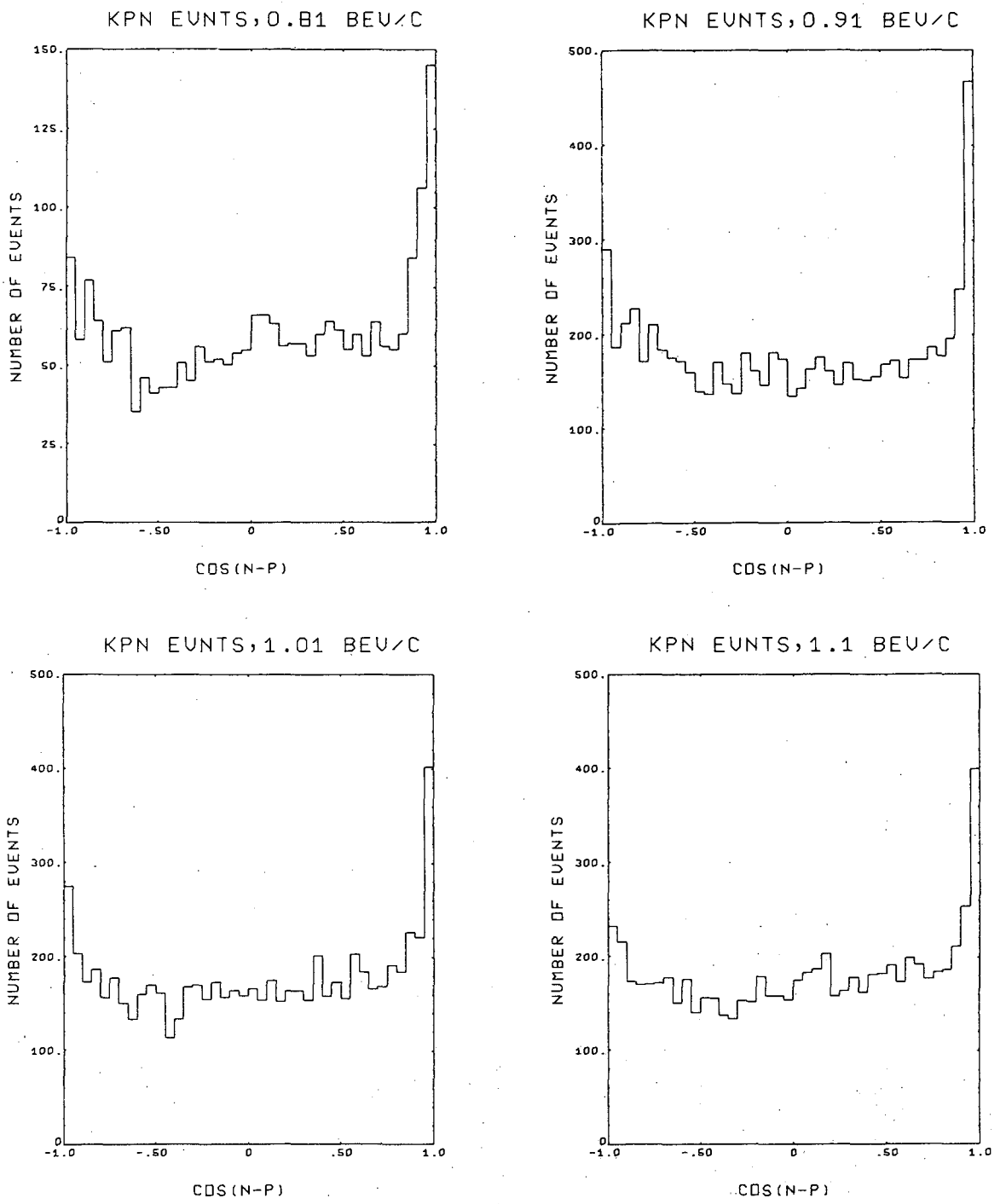

XBL 699-5660

Fig. 5. Histograms of the cosine of the angle between the proton and the neutron for $K^- d \rightarrow K^- pn$ events.

2. Lambda Contamination

From the diagrams in Fig. 3, we see that a large number (~40%) of the K^-d elastic scattering events fit also the $\pi^-p\Lambda$ hypothesis H3. To determine what fraction of this number represents actual $\pi^-p\Lambda$ events, we examine Fig. 6. This is a missing-mass histogram resulting from having all the events that satisfied hypothesis H1 put through the fit for hypothesis H3. We see that for each momentum the mass peak is below the lambda rest mass. This is consistent with mis-identifying the K^-d elastic scattering events as $\pi^-p\Lambda$ events. From the absence of a bump near the lambda rest mass, we estimate that the lambda contamination was negligible (less than 1%) in our sample of K^-d elastic scattering events.

In the case of the break-up reaction, we can estimate the contamination from the $\pi^-p\Lambda$ events in another way. It was found in Ref. 8 that there should be 1350 $\pi^-p\Lambda$ events and 480 $\pi^-p\Sigma^o$ events in the 1.11 BeV/c film which had a spectator proton track between 1.5 mm and 6 cm in length. The two numbers include both the visible and invisible decay modes of the lambda. They also include corrections to bring their cross-sections into agreement with other experiments considered in Ref. 8. From a separate scan, we also found that there were 590 events fitting $\pi^-p\Lambda$ and 530 fitting $\pi^-p\Sigma^o$, with the spectator proton track longer than 6 cm. Combining these numbers gives 2950 events with a lambda in the final state. Only 1/3 of these lambdas (~980) decay via the invisible mode $n\pi^o$. Since we used only 1/2 the film at 1.11 BeV/c for the break-up reaction, we have included only 1/2 this number of lambdas (~490) in our sample. From the fit of our sample to hypothesis H3, we have 526 events that fitted only this hypothesis. Thus we see that the $\pi^-p\Lambda$ events are separated out by the χ^2 section. We conclude that the lambda contamination is also small in the break-up reaction (less than 2%) of the 1.11 BeV/c sample. We

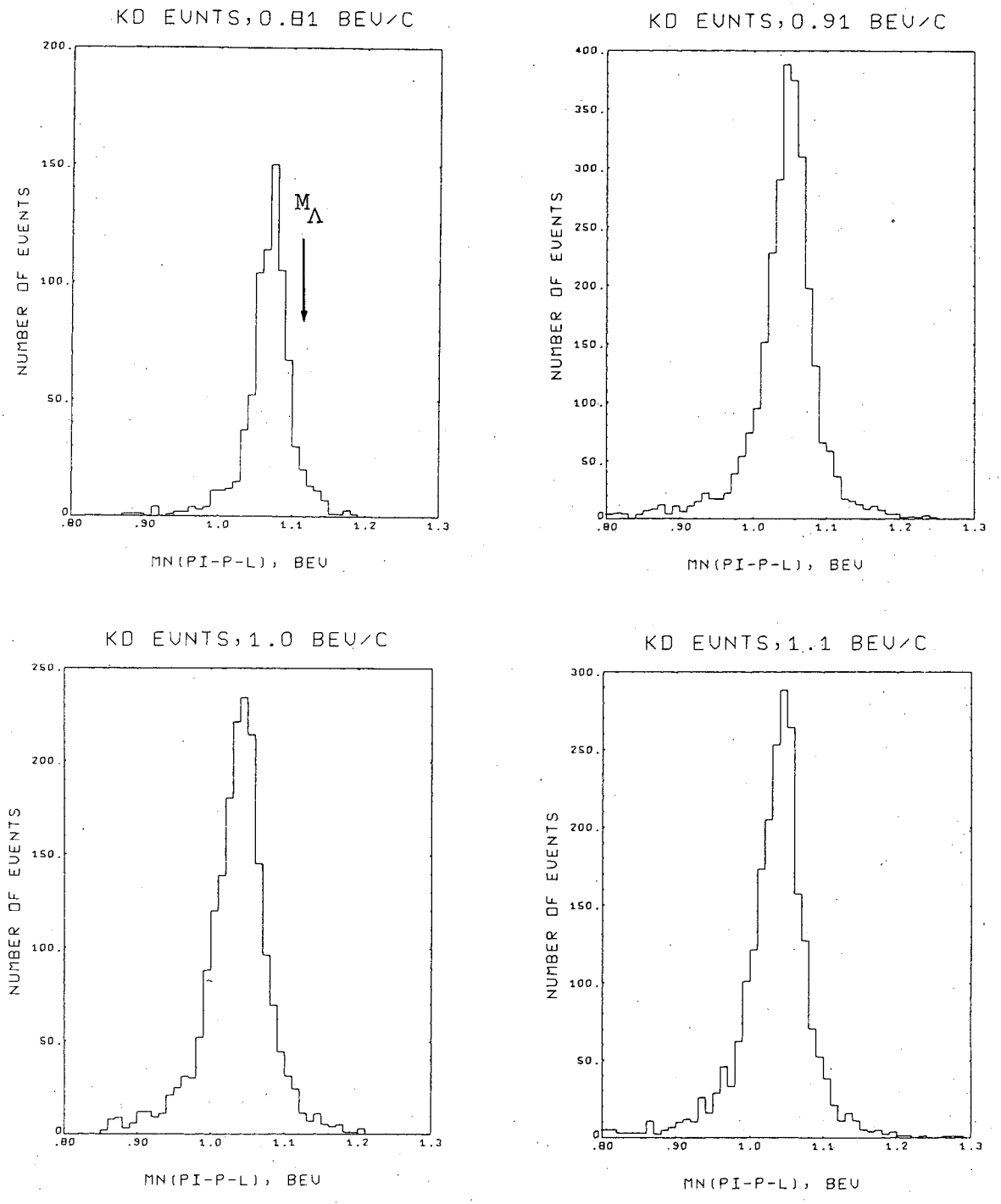

XBL 699-5650

Fig. 6. Missing mass histograms for K^-d elastic scattering events going through the $K^-d \rightarrow \pi^- p\Lambda$ hypotheses.

have not scanned for $\pi^- p\Lambda$ events with long spectator proton for the remaining three momenta. But from the number of events fitting only hypothesis H3 in these momenta, we estimate the Λ contamination to be about the same as in the 1.11 BeV/c sample.

D. Correction of Biases and Losses

1. Azimuthal Angle Scanning Bias

In scanning for events for this experiment, we had imposed the criterion that each event must have a positive track longer than 1mm. This cut was imposed for measuring purposes. Unfortunately, this introduced a bias against events with a short positive track pointing along the camera axis, which was up-and-down with respect to the bubble chamber. (The beam entered the chamber in a horizontal plane at mid-chamber. The three cameras were positioned at the bottom, looking vertically up.) These events appeared fore-shortened on film. A distribution of events as a function of the azimuthal angle of the positive track about the beam axis shows clearly this scan bias. This is shown in Figs. 7 and 8. If there were no biases, these distributions would be uniform. The large number of events missing around 0° and 180°, corresponding to the up-down direction, indicates such a bias. This bias is against short tracks. It causes a depletion of events in the forward direction in the angular distributions, thus effectively flattening their slope. To avoid this bias, we have included in our distributions only those events with the positive track coming out of the interaction vertex within 45° of the horizontal plane. The only exception to this is the distribution for the break-up reaction at 0.81 BeV/c. Since we do not have many events at this incident momentum and since the azimuthal angular distribution for the break-up reaction at this

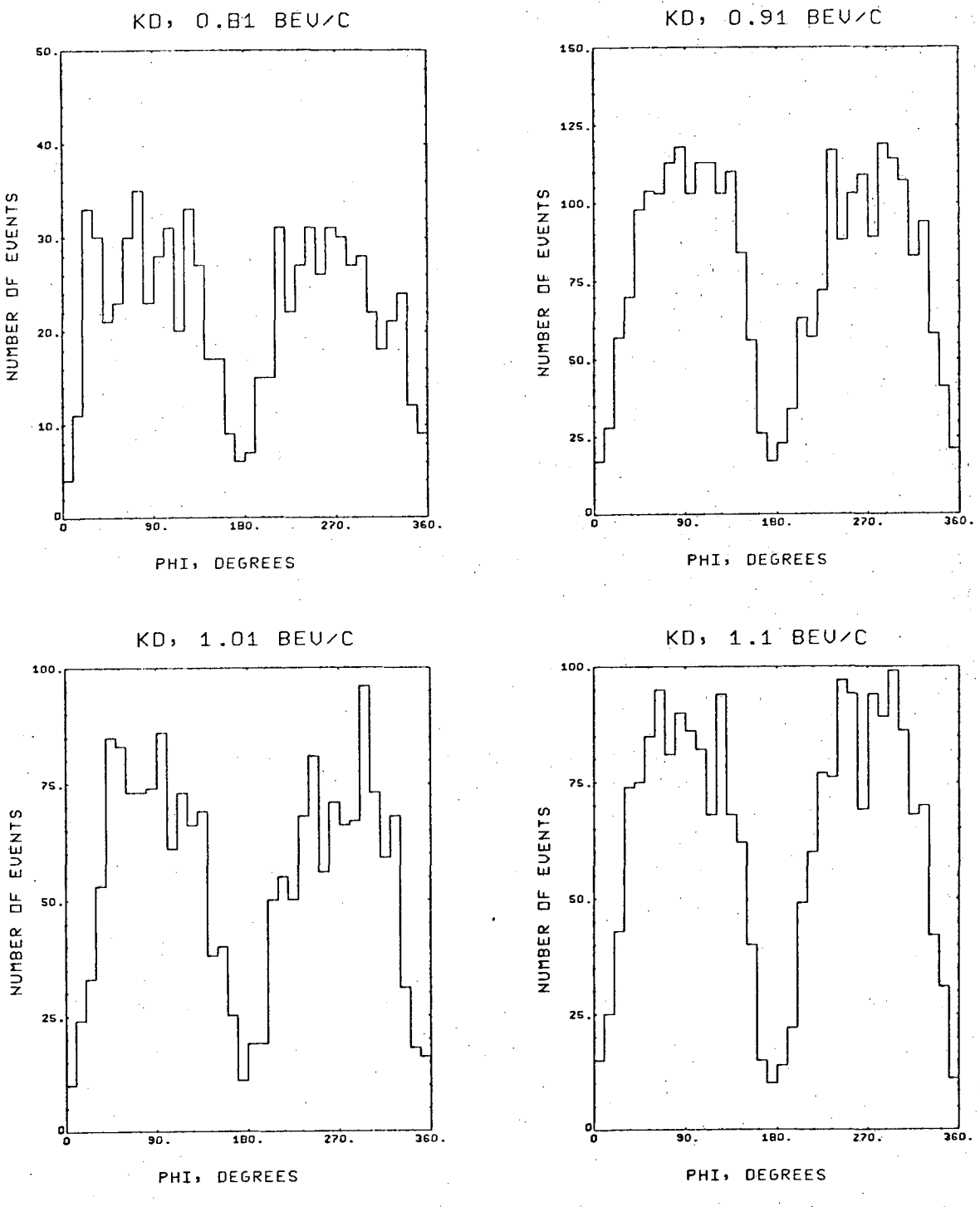

Fig. 7. Histograms of the azimuthal angle of the positive track about the beam axis for $K^-d \to K^-d$ events.

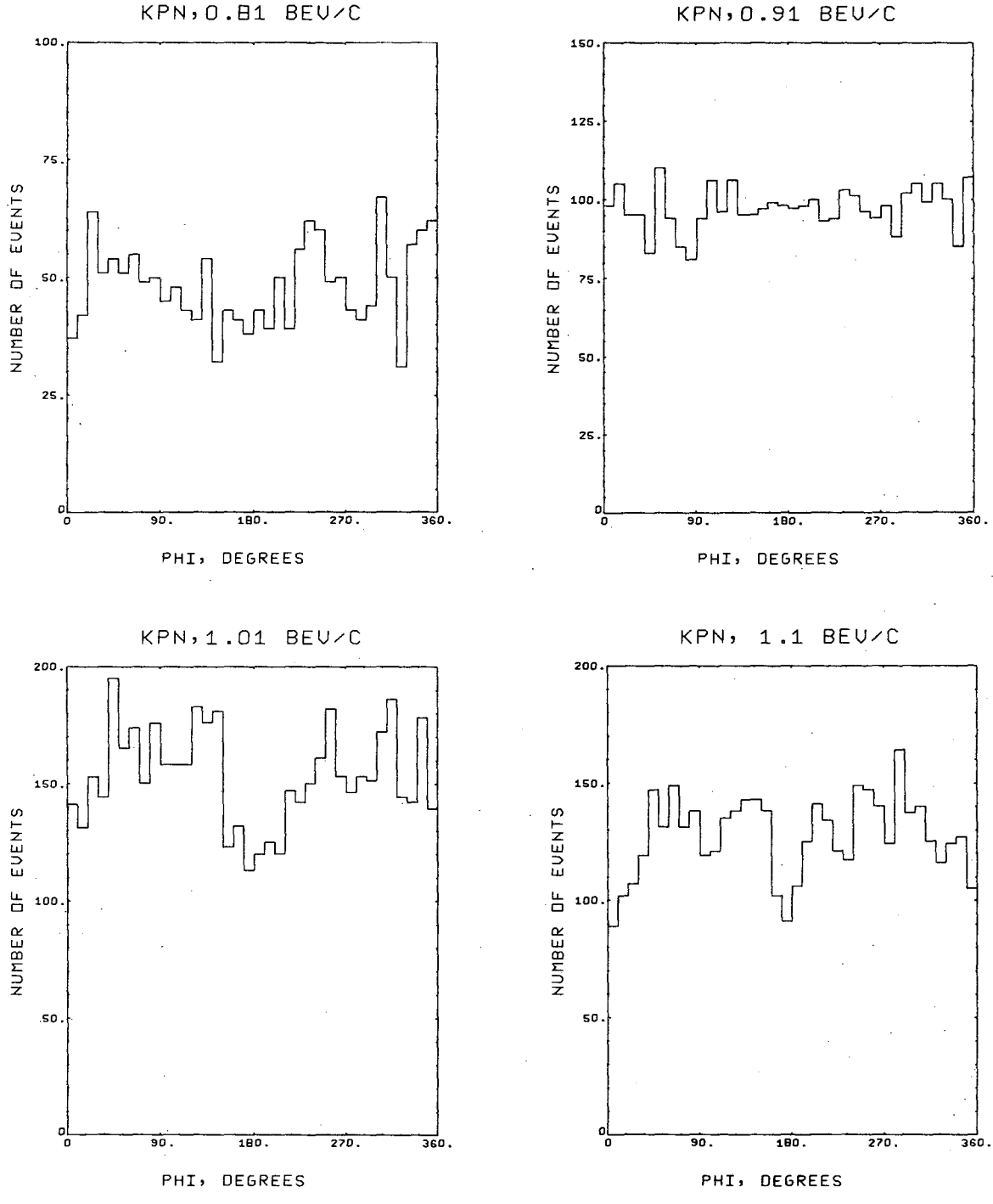

Fig. 8. Histograms of the azimuthal angle of the positive track about the beam axis for $\bar{K}d \rightarrow \bar{K}pn$.

momentum does not show a serious bias, we have included all the events in this case for analysis.

As an illustration of the change in the angular distribution arising from this scan bias, we show in Fig. 9 two histograms of the angular distribution for K^-d elastic scattering at 1.11 BeV/c. Events in Fig. 9a have their positive track come out of the interaction vertex within 45° of the horizontal plane. Events in Fig. 9b have this track come off with an angle of more than 45°.

2. χ^2 Distribution Correction

The experimental χ^2 distributions for the K^-d elastic scattering hypothesis at the four incident momenta are shown in Fig. 10. As is quite common, these experimental distributions have a large tail. One way to correct for this long tail effect is to accept events up to a $\chi^2 = 20$ as K^-d elastic scattering events. We have decided to accept events up to a $\chi^2 = 10$, which is normal for a χ^2 of 4 degrees of freedom. We account for the events in the tail by correcting the number of events thus obtained by the excess of events in the experimental tail over those in the theoretical tail (defined by the interval $10 \leq \chi^2 \leq 20$). The correction factor at each incident momentum is shown in Table I.

To consider the effect of this χ^2 cut on the break-up reaction events, we look at Fig. 5. This gives histograms of the cosine of the angle between the proton and the neutron in the break-up reaction. We see that there is an excess of events in the forward bins. These are K^-d elastic scattering events with a $\chi^2 > 10$. To eliminate these high $\chi^2 K^-d$ elastic scattering events from our sample of break-up events, we exclude from our sample of the latter those events which have the cosine of the angle between the proton and the neutron within the interval (0.9, 1.0). This cut removed some real break-up events. But these

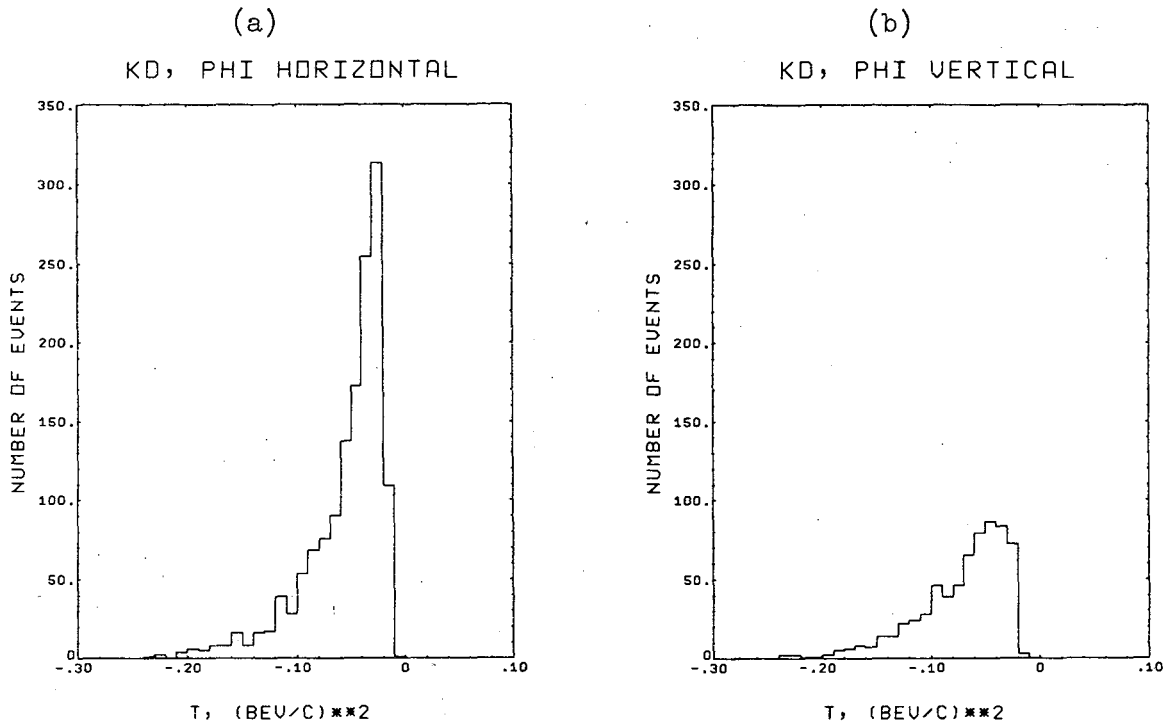

XBL 699-5661

Fig. 9. (a) t-distribution for $K^-d \to K^-d$ events with the outgoing deuteron within 45° of the bubble chamber horizontal plane; (b) within 45° of the vertical plane.

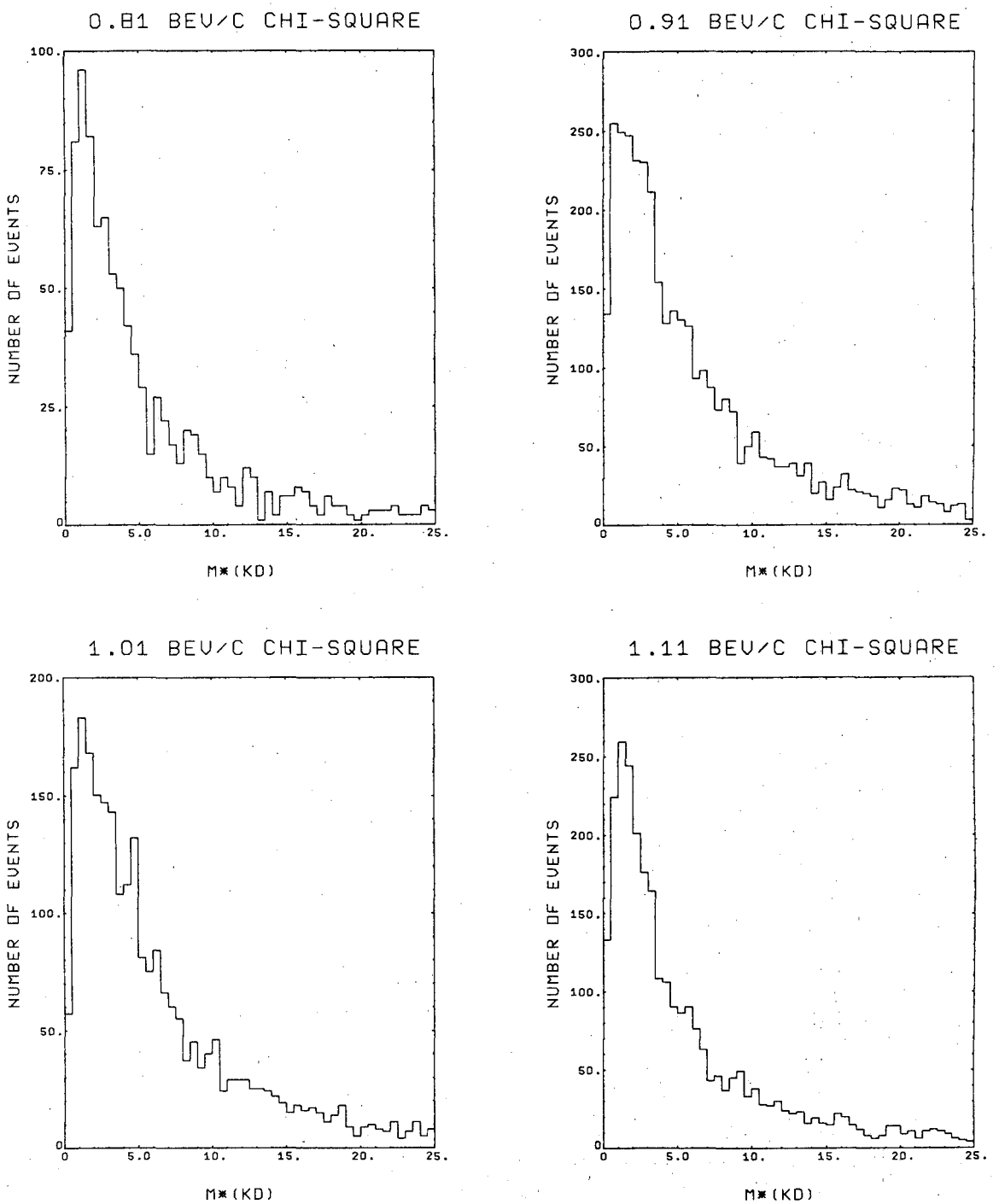

Fig. 10. χ^2 distributions for the $K^-d \to K^-d$ hypothesis.

events have predominantly small momentum transfers to the K^-. We correct for this bias by using only the part of the momentum transfer distribution with $-t \geq 0.06$ $(BeV/c)^2$ in our analysis.

3. Scan Efficiency

We rescanned portions of our film to check for scan biases. All of the film which were scanned the first time with an upper cut on the positive track length were rescanned completely. This portion of our film was used to obtain the sample of K^-d elastic scattering events. Of the portion of film scanned with no upper cut on the positive track length, approximately 1/3 was rescanned. This portion was used to obtain the break-up reaction events.

To estimate the scan efficiency for the elastic scattering reaction, we use the method described in Ref. 9 for the case of two scans. The over-all efficiency is given by

$$E = \frac{(\mu_{12} - 1)(4 - \mu_{12})}{\mu_{12}}$$

where $\mu_{12} = \frac{1}{\lambda_1} + \frac{1}{\lambda_2}$ and λ_i is the efficiency of scan i. The individual efficiencies λ_i are estimated through the relations

$$\lambda_1 = \frac{N_{12}}{N_2} \text{ and } \lambda_2 = \frac{N_{12}}{N_1} ,$$

where N_i is the number of events found in scan i and N_{12} is the number of events found in both scans. The overall efficiency E for the elastic scattering reaction calculated with this method are given in Table I for each incident momentum.

Since we did not rescan completely the film used for the break-up

reaction, we just used the rescan to estimate the efficiency of the first scan and correct our data according to this. The efficiencies for this reaction are also shown in Table I.

III. FORMALISM FOR K^--DEUTERON SCATTERING

Having obtained the data in the form of angular distributions for the elastic scattering and the break-up reactions, we wish to analyze these distributions in detail in terms of a theoretical model of deuteron interactions. The particular model we have chosen is based on the impact parameter formalism as developed by R. J. Glauber.[10] We present in Section III-A this formalism in some detail, neglecting, however, the complications due to spin. In Section III-B, we modify this formalism in order to make it applicable to our data, which contains a cut on the proton momentum. We conclude in Section III-C by extending the formalism to include spin effects.

A. The Impact Parameter Formalism

The impact parameter method of treating high energy collisions of composite particles was developed by R. J. Glauber[10] and more recently discussed by V. Franco and R. J. Glauber,[11] C. Wilkin,[12] and others.[13] We first discuss in this section this formalism for the case of particle-nucleus scattering. After having done this, we then specialize the results to K^--deuteron scattering. We consider both the K^-d elastic scattering and the break-up reactions.

1. Particle-Nucleus Scattering

The basic idea of the impact parameter method stems from the close analogy between wave mechanics and classical optics. As is well known,[14] the Schrödinger equation (mass $m=1/2$, $\hbar=c=1$)

$$\left[\nabla^2 + E - V(\bar{r}) \right] \psi(\bar{r}) = 0$$

has the same form as the wave equation of light propagation, with the index of refraction given by

$$n = \sqrt{E - V} \quad .$$

The Glauber approximation corresponds to the eikonal method of solving the wave equation. (See Ref. 10). The solution is given by

$$\psi(\bar{r}) = \exp\left[-\bar{k}_i \cdot \bar{r} - \frac{i}{2k} \int_{-\infty}^{z} dz' \, V(z'^2 + \bar{b}^2) \right], \qquad \text{(III-1)}$$

where z' is along the direction of the incident momentum $\bar{k}_i$, and $k = |\bar{k}_i| = \sqrt{E}$. The vector $\bar{b}$ is perpendicular to $\bar{k}_i$ and has the interpretation of an impact parameter in classical scattering theory. The equation for the scattering amplitude (see Appendix A) is given by

$$A(\bar{k}_f, \bar{k}_i) = -\frac{1}{4\pi} \int d^3\bar{r} \, e^{i\bar{k}_f \cdot \bar{r}} \, V(\bar{r}) \, \psi(\bar{r}) \qquad \text{(III-2)}$$

Putting Eq. III-1 into Eq. III-2, we obtain

$$A(\bar{q}) = -\frac{1}{4\pi} \int d^3\bar{r} \, V(\bar{r}) \, e^{i\bar{q}\cdot\bar{r}} \exp\left[\frac{-i}{2k} \int_{-\infty}^{z} dz' V(z'^2 + \bar{b}^2) \right],$$

where we have put $\bar{q} = \bar{k}_f - \bar{k}_i$. For small angle scattering, $\bar{q}\cdot\bar{r} \cong \bar{q}\cdot\bar{b}$, and we can rewrite $A(\bar{q})$ in the form

$$A(\bar{q}) = -\frac{1}{4\pi} \int d^2\bar{b} \, e^{i\bar{q}\cdot\bar{b}} \int_{-\infty}^{\infty} dz \, V(\bar{r}) \exp\left[\frac{-i}{2k} \int_{-\infty}^{z} dz' \, V(z'^2 + \bar{b}^2) \right]. \qquad \text{(III-3)}$$

The integration with respect to z can be carried out, and it gives

$$\frac{-2k}{i} \exp\left[\frac{-i}{2k} \int_{-\infty}^{z} dz' \, V(z'^2 + \bar{b}^2) \right]_{-\infty}^{\infty} = 2ik \left\{ \exp\left[\frac{-i}{2k} \int_{-\infty}^{\infty} dz' \, V(z'^2 + \bar{b}^2) \right] - 1 \right\}$$

Putting this back into Eq. III-3, we arrive at the equation given by Glauber,

$$A(\bar{q}) = \frac{ik}{2\pi} \int d^2\bar{b} \, e^{i\bar{q}\cdot\bar{b}} \left[1 - e^{2i\chi(\bar{b})} \right].$$

where we have defined

$$\chi(\bar{b}) = -\frac{1}{4k}\int_{-\infty}^{\infty} dz\, V(z^2+\bar{b}^2) \ . \qquad \text{(III-4)}$$

In the absence of absorption, $V(\bar{r})$ is real, and $\chi(\bar{b})$ can be interpreted as a change of phase arising from the scattering by the potential $V(\bar{r})$. In the case of scattering from two scattering centers located at $\bar{r}_1$ and $\bar{r}_2$,

$$V(\bar{r}) = V_1(\bar{r}-\bar{r}_1) + V_2(\bar{r}-\bar{r}_2) \ .$$

We have from this and Eq. III-4 the relation that

$$\chi(\bar{b}) = \chi_1(\bar{b}-\bar{s}_1) + \chi_2(\bar{b}-\bar{s}_2) \ .$$

In other words, the scattering phases due to different scatterers are additive. Here χ_j are similarly defined as $\chi(\bar{b})$ in Eq. III-4, and $\bar{s}_j$ are projections of $\bar{r}_j$ onto the x-y plane. The z direction is taken along the beam axis $\bar{k}_i$. The fact that the <u>phases</u> rather than the <u>amplitudes</u> add coherently gives rise to double scattering terms in this formalism, as we shall see below. If we make the simplifying assumption that, in scattering a particle off a nucleus of mass number A, the phases $\chi_j(\bar{b}-\bar{s}_j)$ arising from scattering by the individual nucleons j add coherently; i.e. if we assume that

$$\chi(\bar{b}) = \sum_{j=1}^{A} \chi_j(\bar{b}-\bar{s}_j) \ ,$$

then the particle-nucleus scattering amplitude would be given by

$$A(\bar{q}) = \frac{ik}{2\pi}\int d^2\bar{b}\ e^{i\bar{q}\cdot\bar{b}}\left[1 - \prod_{j=1}^{A}\exp\left\{2i\chi_j(\bar{b}-\bar{s}_j)\right\}\right] \ .$$

To account for the motion of the nucleons within the nucleus, we form the expectation value of the amplitude between the initial and final

nuclear states and have

$$A_{fi}(\bar{q}) = \frac{ik}{2\pi}\int d^2\bar{b}\; e^{i\bar{q}\cdot\bar{b}} \langle f|\left[1 - \prod_{j=1}^{A} \exp\left\{2i\chi_j(\bar{b}-\bar{s}_j)\right\}\right]|i\rangle$$

Writing this in terms of the center of mass position variables of the nucleons and nuclear wave functions, we have equivalently

$$A_{fi}(\bar{q}) = \frac{ik}{2\pi}\int d^2\bar{b}\; e^{i\bar{q}\cdot\bar{b}}\int \prod_{\ell=1}^{A} d^3\bar{r}_\ell\; \psi_f^*(\bar{r}_1,\cdots,\bar{r}_A)\psi_i(\bar{r}_1,\cdots,\bar{r}_A)\delta^3\left(\frac{1}{A}\sum_{j=1}^{A}\bar{r}_j\right) x$$
$$x\left[1 - \prod_{j=1}^{A} \exp\left\{2i\chi_j(\bar{b}-\bar{s}_j)\right\}\right]. \qquad \text{(III-5)}$$

The 3-dimensional δ-function comes from the fact that not all of the $\bar{r}_j$ are linearly independent. They are constrained by the center-of-mass relation

$$\sum_{j=1}^{A} \bar{r}_j = 0 .$$

For scattering of the incident particle by the individual nucleon j, we can also write the amplitude as

$$A_j(\bar{q}) = \frac{ik}{2\pi}\int d^2\bar{b}\; e^{i\bar{q}\cdot\bar{b}}\left[1 - \exp\left\{2i\chi_j(\bar{b})\right\}\right].$$

An approximate inversion of this formula is given by

$$\exp\left\{2i\chi_j(\bar{b})\right\} = 1 - \frac{1}{2\pi ik}\int d^2\bar{q}\; A_j(\bar{q})\; e^{-i\bar{q}\cdot\bar{b}} \quad . \qquad \text{(III-6)}$$

This is a good approximation for small angle scattering. In such cases, $A_j(\bar{q})$ is peaked in the forward direction (small $\bar{q}$), and $\bar{q}$ and $\bar{b}$ would be approximately coplanar. Putting Eq. III-6 into Eq. III-5 yields finally the multiple scattering series,

$$A_{fi}(\bar{q}) = \frac{ik}{2\pi}\int d^2\bar{b}\; e^{i\bar{q}\cdot\bar{b}} \int \prod_{\ell=1}^{A} d^3\bar{r}_\ell \psi_f^*(\bar{r}_1,\ldots,\bar{r}_A)\psi_i(\bar{r}_1,..,\bar{r}_A)\delta^3(\tfrac{1}{A}\textstyle\sum_{j=1}^{A} \bar{r}_j) \times \qquad \text{(III-7)}$$

$$\times\left[1 - \prod_{j=1}^{A}\left\{1 - \frac{1}{2\pi ik}\int d^2\bar{q}'\; A_j(\bar{q}')\exp\left[-i\bar{q}\cdot(\bar{b}-\bar{s}_j)\right]\right\}\right].$$

Expanding the product within the square bracket gives rise to terms which can be interpreted as due to single-, double-, and triple-scattering, and so on.

2. Specialization to K^--Deuteron Scattering

We now specialize this multiple scattering formula and apply it to K^--deuteron scattering. The deuteron and the nucleons will be treated as spinless particles. We extend this formalism to include spin in Sec. III-C.

Let $\bar{r}$ be the relative coordinate vector pointing from the neutron to the proton. Thus we have for the proton and neutron center-of-mass coordinates $\bar{r}_p = \bar{r}/2$ and $\bar{r}_n = -\bar{r}/2$. We let $\bar{s}$ be the projection of $\bar{r}$ onto the x-y plane. After using the 3-dimensional δ-function to integrate out one of the space volume integrals in Eq. III-7 (A = 2 in this case), the scattering amplitude becomes

$$A_{fi}(\bar{q}) = \frac{ik}{2\pi}\int d^2\bar{b}\; e^{i\bar{q}\cdot\bar{b}} \int d^3\bar{r}\; \psi_f^*(\bar{r})\,\psi_i(\bar{r})\left[1 - \right. \qquad \text{(III-8)}$$

$$\left.\left\{1 - \frac{1}{2\pi ik}\int d^2\bar{q}'\; A_n(\bar{q}')\, e^{-i\bar{q}'\cdot(\bar{b}-\bar{s}/2)}\right\}\left\{1 - \frac{1}{2\pi ik}\int d^3\bar{q}'\; A_p(\bar{q}')e^{-i\bar{q}'\cdot(\bar{b}+\bar{s}/2)}\right\}\right].$$

Carrying out the indicated integrations with respect to $\bar{b}$ and $\bar{r}$ (see Appendix B), this can be rewritten as

$$A_{fi}(\bar{q}) = G_{fi}(\bar{q}/2)\, A_n(\bar{q}) + G_{fi}(-\bar{q}/2)\, A_p(\bar{q}) + \frac{i}{2\pi k}\int d^2\bar{q}'\, G_{fi}(\bar{q}')\, A_n(\bar{q}'+\bar{q}/2)\, A_p(-\bar{q}'+\bar{q}/2) \qquad \text{(III-9)}$$

where

$$G_{fi}(\bar{q}) = \int d^3\bar{p}\, \varphi_f^*(\bar{p})\, \varphi_i(\bar{p} - \bar{q}) \quad . \qquad \text{(III-10)}$$

$\varphi_f(\bar{p})$ and $\varphi_i(\bar{p})$ are the Fourier transforms of $\psi_f(\bar{r})$ and $\psi_i(\bar{r})$, respectively. The first two terms of Eq. III-9 are the single scattering contributions to K^--deuteron scattering. These correspond to the impulse approximation contributions. The third term gives the double scattering correction to the impulse approximation.

3. K^-d Elastic Scattering

We next consider K^--deuteron elastic scattering. In this case we have $\varphi_f(\bar{p}) = \varphi_i(\bar{p}) = \varphi_D(\bar{p})$, the deuteron momentum space wave function. We define the deuteron form factor as

$$G(\bar{q}) = \int d^3\bar{p}\, \varphi_D^*(\bar{p})\, \varphi_D(\bar{p}-\bar{q}) \quad .$$

This is the convolution integral giving the Fourier transform of the product $|\psi_D(\bar{r})|^2$; i.e. we also have

$$G(\bar{q}) = \int d^3\bar{r}\, e^{i\bar{q}\cdot\bar{r}} |\psi_D(\bar{r})|^2$$

where $\psi_D(\bar{r})$ is the deuteron coordinate space wave function. In cases where $\psi_D(\bar{r})$ depends only on the magnetude of $\bar{r}$, we have $G(\bar{q}) = G(-\bar{q})$. Thus from Eq. III-9, the elastic scattering amplitude becomes

$$A_{el}(\bar{q}) = G(\bar{q}/2)\left[\, A_n(\bar{q}) + A_p(\bar{q}) \,\right] + \frac{i}{2\pi k}\int d^2\bar{q}'\; G(\bar{q}')\, A_n(\bar{q}' + \bar{q}/2)\, A_p(-\bar{q}' + \bar{q}/2) \qquad \text{(III-11)}$$

The elastic scattering cross-section is given by

$$\left(\frac{d\sigma}{d\Omega}\right)_{el} = |A_{el}(\bar{q})|^2 \quad .$$

Written out explicitly, this is

$$\left(\frac{d\sigma}{d\Omega}\right)_{el} = G^2(\bar{q}/2)\left[\, |A_n(\bar{q})|^2 + |A_p(\bar{q})|^2 + 2\mathrm{Re}\left\{A_n(\bar{q})\, A_p^*(\bar{q})\right\}\right] - \frac{G(\bar{q}/2)}{\pi k}\ \mathrm{Im}\left[\left\{A_n^*(\bar{q}) + A_p^*(\bar{q})\right\}\int d^2\bar{q}'\; G(\bar{q}')\, A_n(\bar{q}_+)\, A_p(\bar{q}_-)\right] + \frac{1}{(2\pi k)^2}\left|\int d^2\bar{q}'\; G(\bar{q}')\, A_n(\bar{q}_+)\, A_p(\bar{q}_-)\right|^2 , \qquad \text{(III-12)}$$

where $\bar{q}_\pm = \pm\,\bar{q}' + \bar{q}/2$.

4. Total Cross-Sections and Cross-Section Defect

To obtain the total cross-section for K^--deuteron scattering in terms of the total cross-sections for K^--nucleon scattering, we note from the optical theorem that the K^-d total cross-section is given by

$$\sigma_d = \frac{4\pi}{k}\ \mathrm{Im}\, A_{el}(0) \quad .$$

Similarly, the K^--nucleon total cross-sections are given by

$$\sigma_j = \frac{4\pi}{k}\ \mathrm{Im}\, A_j(0), \qquad j = p,\ n \quad .$$

Because of the normalization of the deuteron wave function, $G(0) = 1$.

Taking the imaginary part of Eq. III-11, we find that

$$\sigma_d = \sigma_n + \sigma_p - d\sigma \quad ,$$

where the cross-section defect $d\sigma$ is defined by

$$d\sigma = -\frac{2}{k^2}\int d^2\bar{q}\; G(\bar{q})\; \mathrm{Re}\left[A_n(\bar{q})\; A_p(-\bar{q})\right] . \qquad \text{(III-13)}$$

Thus the K^-d total cross-section is not simply the sum of the single nucleon total cross-sections. It has an additional contribution $d\sigma$ coming from the double scattering effects arising from the composite structure of the deuteron. Depending on the relative phases of the nucleon amplitudes $A_n(\bar{q})$ and $A_p(\bar{q})$, this contribution can be either positive or negative.

5. Break Up of the Deuteron

Finally, we turn our attention to the reaction in which the deuteron is broken up into a free neutron and a free proton in the final state. The amplitude is still given by Eq. III-9. Though in the present case we still have $\varphi_i(\bar{p}) = \varphi_D(\bar{p})$, $\varphi_f(\bar{p})$ is unknown. The usual approximation introduced to handle this has been the closure approximation.[11] It assumes that the set of final states $\varphi_f(\bar{p})$ is complete. With this assumption, we then have

$$\sum_f \varphi_f^*(\bar{p})\; \varphi_f(\bar{p}') = \delta^3(\bar{p} - \bar{p}') \quad . \qquad \text{(III-14)}$$

The differential cross-section is given by

$$\left(\frac{d\sigma}{d\Omega}\right)_{Kpn} = \sum_f \left|A_{fi}(\bar{q})\right|^2 \quad . \qquad \text{(III-15)}$$

Using the closure relation and Eq. III-10, we have

$$\sum_f G^*_{fi}(\bar{q}') \, G_{fi}(\bar{q}) = \sum_f \int d^3\bar{p} \; d^3\bar{p}' \; \varphi_f(\bar{p}') \, \varphi^*_i(\bar{p}'-\bar{q}') \, \varphi^*_f(\bar{p}) \, \varphi_i(\bar{p}-\bar{q})$$

$$= \int d^3p \; d^3\bar{p}' \; \varphi^*_i(\bar{p}'-\bar{q}') \, \delta^3(\bar{p}'-\bar{p}) \, \varphi_i(\bar{p}-\bar{q}) \qquad \text{(III-16)}$$

$$= \int d^3\bar{p} \; \varphi^*_i(\bar{p}-\bar{q}') \, \varphi_i(\bar{p}-\bar{q})$$

With a change of the variables of integration, the last integral can be rewritten as

$$\int d^3\bar{p} \; \varphi^*_i(\bar{p}) \, \varphi_i(\bar{p} - (\bar{q} - \bar{q}')) \quad .$$

This is just the deuteron form factor $G(\bar{q}-\bar{q}')$. Thus we have

$$\sum_f G^*_{fi}(\bar{q}') \, G_{fi}(\bar{q}) = G(\bar{q} - \bar{q}') \qquad \text{(III-17)}$$

Using this relation and Eqs. III-9 and III-15, we obtain the cross-section for the break-up reaction

$$\left(\frac{d\sigma}{d\Omega}\right)_{Kpn} = G(0)\left|A_n(\bar{q})\right|^2 + G(0)\left|A_p(\bar{q})\right|^2 + 2G(\bar{q}) \, \mathrm{Re}\left[A_n(\bar{q}) \, A^*_p(\bar{q})\right]$$

$$- \frac{1}{2\pi k} \, \mathrm{Im}\left[A^*_n(\bar{q}) \int d^2\bar{q}' \; G(\bar{q}'-\bar{q}/2) \, A_n(\bar{q}_+) \, A_p(\bar{q}_-)\right] \qquad \text{(III-18)}$$

$$- \frac{1}{2\pi k} \, \mathrm{Im}\left[A^*_p(\bar{q}) \int d^2\bar{q} \; G(\bar{q}'+\bar{q}/2) \, A_n(\bar{q}_+) \, A_p(\bar{q}_-)\right]$$

$$+ \frac{1}{(2\pi k)^2} \int d^2\bar{q}' \; d^2\bar{q}'' \; G(\bar{q}'-\bar{q}'') \, A^*_n(\bar{q}_+) \, A^*_p(\bar{q}_-) \, A_n(\bar{q}'_+) \, A_p(\bar{q}'_-)$$

where $\bar{q}'_\pm = \pm \bar{q}'' + \bar{q}/2$, and $\bar{q}_\pm$ are defined previously.

As noted before, $G(0) = 1$. Eq. III-18 is essentially the formula we used in fitting our break-up reaction data. We now need to modify it to account for the proton momentum cut we made in scanning.

B. Modifications to the Impact Parameter Formalism

We wish to apply Eqs. III-12 and III-18 to the analysis of our experimental data. Aside from spin, Eq. III-12 can be applied to our elastic scattering data without any modifications. However, Eq. III-18 as it stands can not be used to analyze our break-up reaction data. In the derivation of this equation, it was assumed that the final states included all the momentum states of the outgoing particles. This was used in the derivation of Eq. III-16, which states that

$$\sum_f G^*_{fi}(\bar{q}') \, G_{fi}(\bar{q}) = \int d^3\bar{p} \, \varphi^*_i(\bar{p}-\bar{q}') \, \varphi_i(\bar{p}-\bar{q}) \qquad \text{(III-19)}$$

The integral on the right hand side is equal to the deuteron form factor $G(\bar{q}-\bar{q}')$ only if the integration over $\bar{p}$ is taken over the whole 3-momentum space. We have used this fact to arrive at Eq. III-18, expressing the break-up cross-section in terms of the deuteron form factor. On the other hand, we have made a cut on the minimum length of the proton track in our scanning. This implies that the limits of integration in Eq. III-19 no longer extend over the whole space. Consequently Eq. III-18 must be modified to reflect this. For example, the single nucleon scattering terms in Eq. III-18 must be weighted by a factor other than $G(0)$. This factor depends on the limit of integration chosen for the integral in Eq. III-19. However, the integration variable $\bar{p}$ in Eq. III-19 does not correspond to the spectator momentum exactly. Consequently, we run into difficulties in trying to define the limits of integration that correspond to our experimental cut. In an

attempt to clarify this, we adopt a different approach to the problem in the following. As a consequence of this approach, two other modifications to Eq. III-18 also emerge. One of these is Fermi momentum smearing; the other is the flux factor effect. We discuss these at length later.

1. Modifications to the Break-Up Reaction Formula

The approach we use in this section to modify the break-up reaction cross-section formula is based on the method of Feynman diagrams. Such a diagrammatic method has already been used to discuss the elastic scattering of deuterons.[15,16] We start with the expression giving the cross-section for the interaction of two incoming particles, yielding three particles in the final state. Fig. 11a gives a schematic diagram of such a reaction together with the particle labeling scheme. The differential cross-section for this process can be written as[17]

$$\frac{d\sigma(s,t)}{dt} = \frac{1}{2\sqrt{\lambda(s,m_k^2,m_d^2)}} \frac{1}{(2\pi)^5} \int d^4p_1 d^4p_2 d^4p_3 \prod_{j=1}^{3} \theta(p_j)\, \delta(p_j^2-m_j^2) \times$$

$$\times\, \delta^4(p_k+p_d-p_1-p_2-p_3)\, |T|^2\, \delta(t-(p_k-p_1)^2) \qquad \text{(III-20)}$$

where T is the invariant transition matrix, and $s = (p_k+p_d)^2$. $\lambda(x,y,z)$ is the completely symmetric function given by

$$\lambda(x,y,z) = x^2+y^2+z^2 - 2(xy + xz + yz) \quad ,$$

and

$$\theta(p) = \begin{cases} 0 & \text{if } p_o < 0 \\ 1 & \text{if } p_o \geq 0 \end{cases} \quad .$$

We take particle 1 to be the out-going K^- particle. To express Eq. III-20

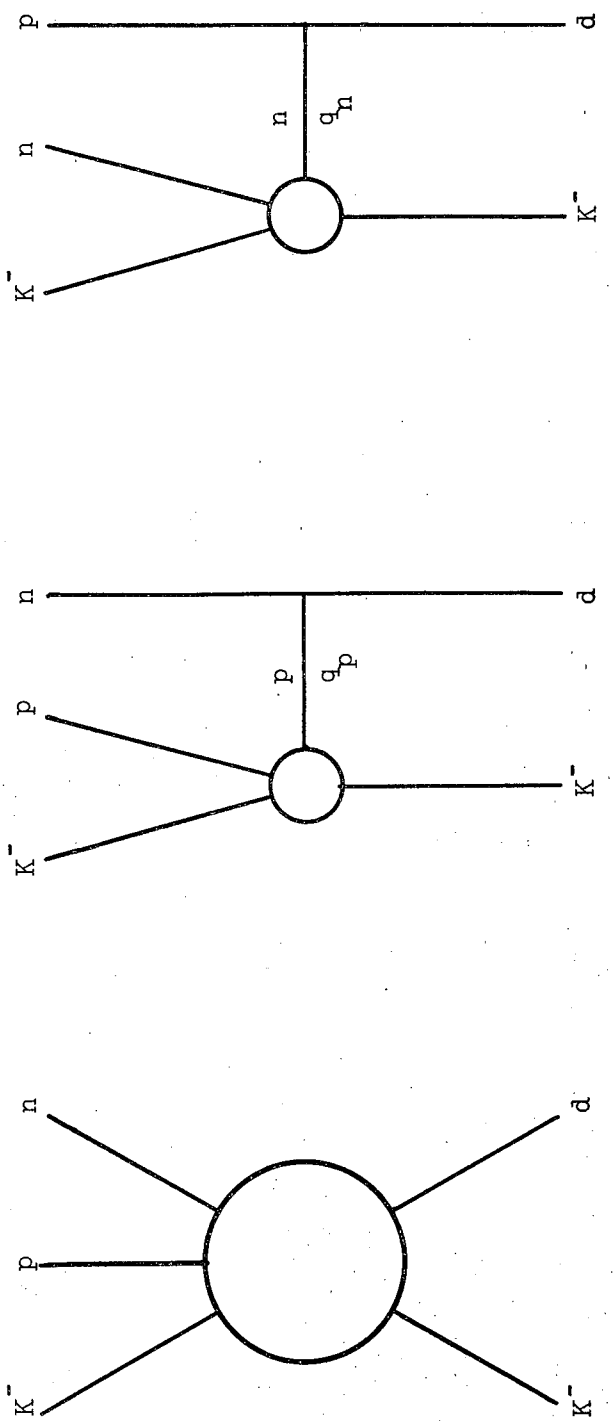

Fig. 11

in terms of 2-body cross-sections, we note that the 3-body phase space is given by

$$R_3(s) = \int d^4p_1 d^4p_2 d^4p_3 \prod_{j=1}^{3} \theta(p_j)\, \delta(p_j^2-m_j^2)\, \delta^4(p_k+p_d-p_1-p_2-p_3) \quad .$$

This can be written recursively in terms of the 2-body phase space $R_2(s')$ as[18]

$$R_3(s) = \int d^4p_3\, \theta(p_3)\, \delta(p_3^2-m_3^2)\, R_2(s') = \int \frac{d^3\bar{p}_3}{2E_3}\, R_2(s')$$

where $R_2(s')$ is defined by

$$R_2(s') = \int d^4p_1 d^4p_2 \prod_{j=1}^{2} \theta(p_j)\, \delta(p_j^2-m_j^2)\, \delta^4(p_k+p_d-p_3-p_1-p_2)$$

and $s' = (p_k+p_d-p_3)^2$ is the total energy squared of the two-particle system. Using this recursion relation, Eq. III-20 can be rewritten as

$$\frac{d\sigma(s,t)}{dt} = \frac{1}{2\sqrt{\lambda(s,m_k^2,m_d^2)}}\, \frac{1}{(2\pi)^5} \int \frac{d^3\bar{p}_3}{2E_3}\, R_2(s')\, |T|^2\, \delta(t-(p_k-p_1)^2). \quad \text{(III-21)}$$

We consider the single scattering contributions to T. They come from the two diagrams in Figs. 11b and 11c. The amplitude can be written as

$$T = g \left[\frac{T_n(s_n,t)}{q_n^2 - m^2} + \frac{T_p(s_p,t)}{q_p^2 - m^2} \right],$$

where

$$q_n = p_d-p_p \quad , \qquad s_n = (p_k+q_n)^2 \quad ,$$

$$q_p = p_d-p_n \quad , \qquad s_p = (p_k+q_p)^2 \quad .$$

$T_n(s_n,t)$ and $T_p(s_p,t)$ are the single nucleon scattering amplitudes, m the nucleon mass, and g the d-n-p coupling constant. The amplitude squared is given by

$$|T|^2 = g^2\left\{\frac{|T_n(s_n,t)|^2}{(q_n^2-m^2)^2} + \frac{|T_p(s_p,t)|^2}{(q_p^2-m^2)^2} + \frac{T_n^*T_p+T_nT_p^*}{(q_n^2-m^2)(q_p^2-m^2)}\right\} \qquad \text{(III-22)}$$

We consider the terms in this equation separately. Putting the first term into Eq. III-21, taking $\bar{p}_3$ in Eq. III-21 to be the spectator proton momentum and writing it as $\bar{p}$, we get for the neutron single scattering contribution to the K^-pn cross-section

$$\left.\frac{d\sigma(s,t)}{dt}\right|_n \frac{1}{2\sqrt{\lambda(s,m_k^2,m_d^2)}} \frac{1}{(2\pi)^5}\int\frac{d^3\bar{p}}{2E_p} \frac{g^2}{(q_n^2-m^2)^2} R_2(s_n)|T_n(s_n,t)|^2\delta(t-(p_k-p_l)^2) \qquad \text{(III-23)}$$

(Note: all terms to the right of R_2 come under the integrals involved in R_2.) We can also write the cross-section for two initial particles going into two particles in the final state as[19]

$$\frac{d\sigma_n(s_n,t)}{dt} = \frac{1}{2\sqrt{\lambda(s_n,m_k^2,m^2)}} \frac{1}{(2\pi)^2} R_2(s_n)\ |T_n(s_n,t)|^2\ \delta(t-(p_k-p_l)^2)$$

Using this we can rewrite Eq. III-23 as

$$\left.\frac{d\sigma(s,t)}{dt}\right|_n = \frac{1}{2\sqrt{\lambda(s,m_k^2,m_d^2)}} \frac{1}{(2\pi)^3}\int\frac{d^3\bar{p}}{2E_p} \frac{g^2}{(q_n^2-m^2)^2} \ 2\sqrt{\lambda(s_m,m_k^2,m^2)}\ \frac{d\sigma_n(s_n,t)}{dt} \qquad \text{(III-24)}$$

Since $\lambda(s,m_k^2,m_d^2)$ is an invariant, we can evaluate it in any coordinate system. In the laboratory system in particular, we have

$$\sqrt{\lambda(s,m_k^2,m_d^2)} = 2m_dP_{lab} \quad ,$$

where P_{lab} is the incident K^- lab momentum. Aside from energy factors coming from the normalization of the initial state, $\sqrt{\lambda(s,m_k^2,m_d^2)}$ is essentially the flux factor for K^- incident on a deuteron. The coupling constant g is related to the deuteron wave function by[20]

$$\frac{1}{\sqrt{2m_d(2\pi)^3}} \quad \frac{g}{(q_n^2-m^2)} = \varphi_D(\bar{p}) \quad ,$$

where $\bar{p}$ is the momentum of the spectator in the deuteron rest system. Putting this into Eq. III-24 we get

$$\left.\frac{d\sigma(s,t)}{dt}\right|_n = \int d^3\bar{p} \; |\varphi_D(\bar{p})|^2 \; \frac{\sqrt{\lambda(s',m_k^2,m^2)}}{2E_p P_{lab}} \; \frac{d\sigma_n(s',t)}{dt} \qquad \text{(III-25)}$$

We emphasize in particular that the integration involved in this equation is over the spectator proton momentum. In a similar manner, the second term in Eq. III-22 gives a contribution corresponding to proton single scattering to the $K\bar{p}n$ cross-section (Eq. III-21) of the form

$$\left.\frac{d\sigma(s,t)}{dt}\right|_p = \int d^3\bar{p} |\varphi_D(\bar{p})|^2 \frac{\sqrt{\lambda(s',m_k^2,m^2)}}{2E_p P_{lab}} \; \frac{d\sigma_p(s',t)}{dt} \quad . \qquad \text{(III-26)}$$

$\bar{p}$ in this case corresponds to the spectator neutron momentum. In both Eqs. III-25 and III-26, $s' = (p_d+p_k-p)^2$, where p is the spectator 4-momentum $(\bar{p},\sqrt{m^2+\bar{p}^2})$. The third term of Eq. III-22 gives an interference between the neutron and proton single scattering amplitudes

$$\left.\frac{d\sigma(s,t)}{dt}\right|_{np} = \int d^3\bar{p}\ \varphi_D^*(\bar{p})\ \varphi_D(\bar{p}-\bar{q})\ \frac{\left[\lambda(s_n,m_k^2,m^2)\lambda(s_p,m_k^2,m^2)\right]^{1/4}}{2E_p P_{lab}}\ x$$

$$x\left[A_n^*(s_n,t)\ A_p(s_p,t) + c.c.\right] \qquad \text{(III-27)}$$

Here $\bar{p}$ corresponds to the proton lab momentum, and $\bar{q} = \bar{p}_k - \bar{p}_{lab}$, $\bar{p}_{lab}$ and $\bar{p}_k$ the lab momentum of the incident K^- and outgoing K^-, respectively. $A_n(s_n,t)$ and $A_p(s_p,t)$ are defined so that they are related to the nucleon cross-sections by

$$\frac{d\sigma_i}{dt}(s_i,t) = |A_i(s_i,t)|^2 \ , \qquad i = n,\ p \ .$$

2. Consequences of the Modifications

Summing up Eqs. III-25, III-26, and III-27, we get the single scattering contributions to the break-up reaction cross-section. These terms correspond to the first three terms of Eq. III-18. Eqs. III-25, III-26, and III-27 contain three modifications to Eq. III-18. We now discuss each of these in turn.

By examining Eqs. III-25, III-26, and III-27, it can be seen how Eq. III-18 is modified to take Fermi momentum smearing into account.[21] We see from these equations that the nucleon cross-sections are not evaluated at an energy that corresponds to a K^- incident on a nucleon at rest in the lab. They are evaluated at an energy given by

$$s' = (p_k+p_d-p)^2 \ ,$$

which depends on the variable of integration $\bar{p}$, the spectator momentum. Thus the single scattering contributions to the break-up reaction

cross-section consist of weighted averages of the nucleon cross-sections, the weight being essentially the Fermi momentum distribution of the deuteron.

A second modification to Eq. III-18 arises from the flux factors. We refer to Eq. III-25 to discuss this. The effect is contained in the ratio

$$R(\bar{p}) = \frac{\sqrt{\lambda(s', m_k^2, m^2)}}{2E_p P_{lab}}$$

appearing under the integral in Eq. III-25. If we assume that the target nucleon was initially at rest in the lab, we have

$$\sqrt{\lambda(s', m_k^2, m^2)} = 2m\, P_{lab} \quad .$$

Because $|\varphi_D(\bar{p})|^2$ peaks at small values of $\bar{p}$ and falls off rapidly with increasing $\bar{p}$, we can make the replacement $E_p = \sqrt{m^2+\bar{p}^2} \sim m$ under the integral in Eq. III-25. In this case the ratio becomes $R(\bar{p}) = 1$, and the integral in Eq. III-25 is just

$$\int d^3\bar{p}\ |\varphi_D(\bar{p})|^2$$

which, due to the normalization of the deuteron wave function, is unity. Thus Eq. III-25 reduces to the first term of Eq. III-18 exactly in this approximation. Similarly Eq. III-26 and III-27 go over exactly to the second and third term of Eq. III-18, respectively. In the general case where we do not assume the target nucleon to be at rest, $R(\bar{p})$ differs from unity. It is a decreasing function of the magnitude of $\bar{p}$. A graph of $R(\bar{p})$ verses $|\bar{p}|$ (the angular dependence of R on $\bar{p}$ has been integrated out) is given in Fig. 12 for incident K^- momenta of 0.81, 1.11, and 5.0 BeV/c. For a given $|\bar{p}|$, we see that $R(\bar{p})$ deviates more

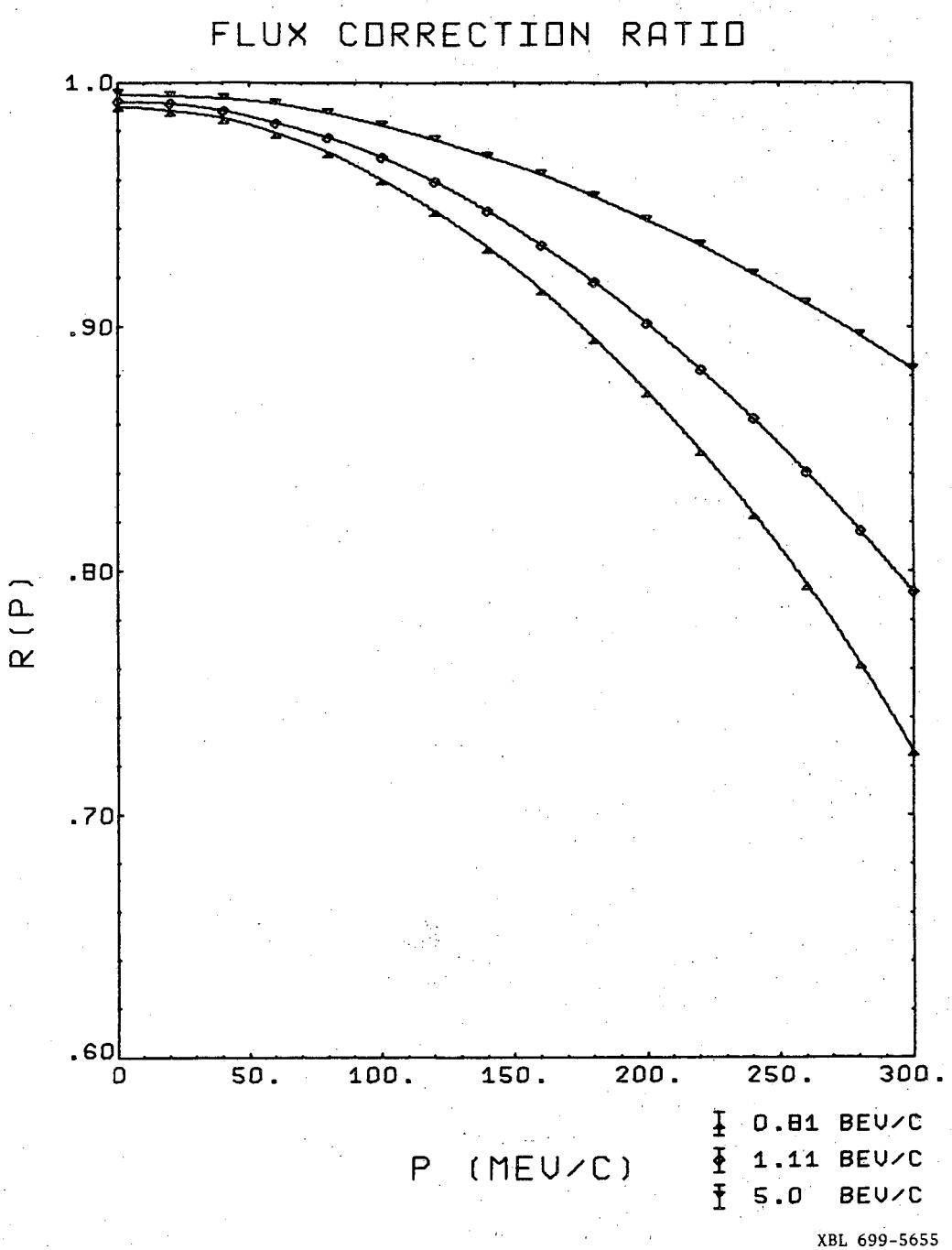

Fig. 12. Ratio of flux factors vs. Fermi momentum at 3 incident K^- momenta.

from unity at the smaller incident K^- momentum than at the larger incident momenta. This implies that the flux factor effect is small at higher energies. For a fixed incident momentum, $R(\bar{p})$ decreases as $|\bar{p}|$ increases. The net effect of this is to depress the tail of the Fermi momentum distribution by 10 to 20%. This in turn affects the integrated cut-off corrections, which we discuss below.

The third modification shown by Eqs. III-25, III-26, and III-27 is the way we account for the proton momentum cut made in our scanning. We first discuss the proton single scattering term, given by Eq. III-26. The integral in Eq. III-26 is over the spectator neutron momentum. We have included in our sample of break-up events those with all possible spectator neutron momentum. Consequently the limits of this integral should be taken over all momentum space. As far as the proton single scattering contribution is concerned, the main effect of the proton momentum cut made in our scanning is to cut out the events scattered into the forward direction ($-t \leq 0.06$ $(\text{BeV}/c)^2$). The distribution at larger $-t$ values are unaffected. As pointed out in Sec. II-C, we are not using the forward part of our experimental distributions. Consequently Eq. III-26 can be used directly to describe the proton single scattering contribution to our experimental break-up reaction, with the integral occurring in this equation taken over all momentum space. This means that we can replace the factor $G(0)$ in the second term of Eq. III-18 by unity. However, because of the presence of the ratio of flux factors in Eq. III-26, we should replace $G(0)$ by

$$\int d^3\bar{p}\ |\varphi_D(\bar{p})|^2\ \frac{\sqrt{\lambda(s', m_k^2, m^2)}}{2E_p P_{lab}} \qquad \text{(III-28)}$$

The value of this integral turns out to be around 0.96 in the range of

incident momenta covered by our experiment (see Fig. 13).

In the case of neutron single scattering and its interference with proton single scattering (Eqs. III-25 and III-27, respectively), we need to put in a lower integration limit that corresponds to the lower cut on the proton momentum in our scanning. In both Eqs. III-25 and III-27, the variable of integration is the proton momentum. Consequently, the correction needed is just to set the lower integration limit equal to the lower proton momentum cut value. The lower curve on each graph in Fig. 13 shows the integrated corrections, given by Eq. III-28, as a function of the lower integration limit p_o. The upper curve in each graph is a plot of the integrated corrections using the deuteron wave function alone (Eq. III-28 without the ratio of flux factors). The value on the lower curve at a particular momentum cut p_o is to be used in place of G(0) appearing in the first term of Eq. III-18. As can be seen from this figure, the net effect of the flux factors is to lower the integrated corrections by 3 to 4%. This difference becomes smaller at higher incident momenta.

C. Spin Dependence

To generalize the results of Sec. III-A to include spin, we take as starting point Eq. III-9,

$$A_{fi}(\bar{q}) = G_{fi}(\bar{q}/2)\, A_n(\bar{q}) + G_{fi}(-q/2)\, A_p(\bar{q}) + \frac{i}{2\pi k} \int d^2\bar{q}'\; G_{fi}(\bar{q}')\, A_n(\bar{q}'+\bar{q}/2)\, A_p(-\bar{q}'+\bar{q}/2) \; .$$

Because the K^- has 0 spin, we can assume that $A_n(\bar{q})$ and $A_p(\bar{q})$ commute. Thus we need not replace the product $A_n A_p$ in this equation by $\frac{1}{2}$ its anti-commutator in order to get the amplitude $A_{fi}(\bar{q})$ symmetric with respect to both the neutron and the proton. We assume that the nucleon

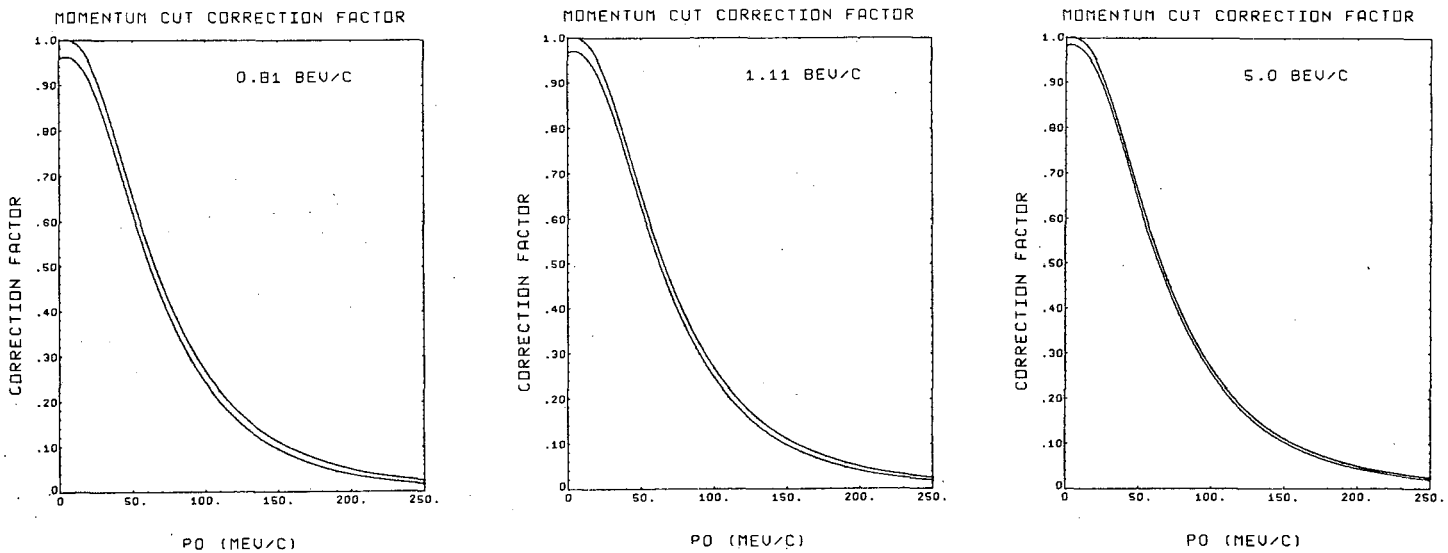

XBL 699-5658

Fig. 13. Spectator momentum cut correction factor as a function of the lower momentum cut. Upper curves are based on the Hulthen distribution alone; lower curves result from modifying the Hulthen distribution with flux factors.

amplitudes $A_j(\bar{q})$ have a spin dependence given by

$$A_j(\bar{q}) = f_j(\bar{q}) + i\ \bar{\sigma}_j \cdot \hat{n}_q\ g_j(\bar{q}) \quad , \qquad j = n,p$$

where $f_j(\bar{q})$ and $g_j(\bar{q})$ are the spin-nonflip and spin-flip amplitudes of K^- scattering on nucleon j, $\bar{\sigma}_j$ the Pauli spin matrices for nucleon j, and $\hat{n}_q$ the unit normal to the scattering plane.

For elastic scattering, we have f = i. The cross-section is given by

$$\left(\frac{d\sigma}{d\Omega}\right)_{el} = |A_{ii}(\bar{q})|^2$$

To get the unpolarized cross-section, we have to average over the initial and sum over the final spin alignments. The result is

$$\left(\frac{d\sigma}{d\Omega}\right)_{el} = \frac{1}{3}\ \mathrm{Tr}\left[P_3 A^+_{ii}(\bar{q})\ P_3 A_{ii}(\bar{q})\right], \qquad \text{(III-29)}$$

where $P_3 = \frac{1}{4}\ (3 + \bar{\sigma}_n \cdot \bar{\sigma}_p)$ is the triplet projection operator, and Tr means the trace in the product spin-space of the nucleons, which is the product of the traces in the individual nucleon spin spaces. The factor $\frac{1}{3}$ comes from averaging over the spin alignments of the deuteron in the initial state. The calculations are presented in Appendix C. The final result is (Eqs. C-11 and C-15 of Appendix C)

$$\left(\frac{d\sigma}{d\Omega}\right)_{el} = \left(\frac{d\sigma}{d\Omega}\right)^{S}_{el} + \left(\frac{d\sigma}{d\Omega}\right)^{SD}_{el} + \text{purely double scattering} \qquad \text{(III-30)}$$

where

$$\left(\frac{d\sigma}{d\Omega}\right)^{S}_{el} = G^2(\bar{q}/2)\left[\left|f_n(\bar{q})+f_p(\bar{q})\right|^2 + \frac{2}{3}\left|g_n(\bar{q})+g_p(\bar{q})\right|^2\right] ,$$

$$\left(\frac{d\sigma}{d\Omega}\right)^{SD}_{el} = -\frac{G(\bar{q}/2)}{\pi k}\,\mathrm{Im}\int d^2\bar{q}'\; G(\bar{q}')\, M_{np}(\bar{q},\bar{q}') \quad .$$

$M_{np}(\bar{q},\bar{q}')$ is given by

$$M_{np}(\bar{q},\bar{q}') = (f^*_n(\bar{q})+f^*_p(\bar{q}))\left[f_n(\bar{q}_+)f_p(\bar{q}_-) - \frac{1}{3}\,g_n(\bar{q}_+)g_p(\bar{q}_-)\hat{n}_{q_+}\cdot\hat{n}_{q_-}\right]$$
$$+ \frac{2}{3}\,(g^*_n(\bar{q})+g^*_p(\bar{q}))\left[g_n(\bar{q}_+)f_p(\bar{q}_-)\hat{n}_q\cdot\hat{n}_{q_+} + g_p(\bar{q}_-)f_n(\bar{q}_+)\hat{n}_q\cdot\hat{n}_{q_-}\right]$$

The definitions of $\hat{n}_q$, $\bar{q}_+$, $\bar{q}_-$, etc. are given in Appendix C. $\left(\frac{d\sigma}{d\Omega}\right)^{S}_{el}$ represents the single scattering contribution to the elastic cross-section. $\left(\frac{d\sigma}{d\Omega}\right)^{SD}_{el}$ represents the contribution coming from the interference between the single scattering and the double scattering amplitudes. We neglect the purely double scattering term, since it gives only a small ($< 1\%$) contribution compared to the other terms. (See Ref. 11; for the definition of this term, see Appendix C.)

The K^-d total cross-section is given by the formula[11]

$$\sigma_d = \frac{4\pi}{k}\;\mathrm{Im}\;\frac{1}{3}\,\mathrm{Tr}(P_3 A_{ii}(0)) \quad . \qquad \text{(III-31)}$$

Carrying out the calculations indicated on the right hand side gives (see Appendix C)

$$\sigma_d = \sigma_n + \sigma_p - d\sigma \quad , \qquad \text{(III-32)}$$

where

$$d\sigma = -\frac{2}{k^2}\int d^2\bar{q}\; G(\bar{q})\;\mathrm{Re}\left[f_n(\bar{q})f_p(-\bar{q}) + \frac{1}{3}\,g_n(\bar{q})\,g_p(-\bar{q})\right]$$

This is the generalization of Eq. III-13 for the cross-section defect.

In the case of the break-up reaction, we again use the closure approximation. For the unpolarized cross-section, the sum over the final spin alignments runs over both the singlet and the triplet spin states of the nucleons. The summation then yields the identity operator rather than the triplet projection operator as in the case of elastic scattering. As a result, it leaves only one triplet projection operator in the cross-section formula, the one arising from the initial deuteron. The cross-section is then given by

$$\left(\frac{d\sigma}{d\Omega}\right)_{Kpn} = \sum_f \frac{1}{3} \mathrm{Tr}\left[P_3 A_{fi}^{+}(\bar{q}) A_{fi}(\bar{q}) \right] \qquad \text{(III-33)}$$

Carrying out the calculations (see Appendix C), we get

$$\left(\frac{d\sigma}{d\Omega}\right)_{Kpn} = \left(\frac{d\sigma}{d\Omega}\right)^{S}_{Kpn} + \left(\frac{d\sigma}{d\Omega}\right)^{SD}_{Kpn} + \text{purely double scattering} \qquad \text{(III-34)}$$

where

$$\left(\frac{d\sigma}{d\Omega}\right)^{S}_{Kpn} = G(0)\left(|f_n(\bar{q})|^2 + |g_n(\bar{q})|^2\right) + G(0)\left(|f_p(\bar{q})|^2 + |g_p(\bar{q})|^2\right)$$
$$+ 2G(\bar{q})\,\mathrm{Re}\left[f_n(\bar{q}) f_p^{*}(\bar{q}) + \frac{1}{3} g_n(\bar{q}) g_p^{*}(\bar{q}) \right]$$

$$\left(\frac{d\sigma}{d\Omega}\right)^{SD}_{Kpn} = -\frac{1}{\pi k}\,\mathrm{Im}\int d^2\bar{q}'\,\left[G(\bar{q}_-)\, M_n(\bar{q},\bar{q}') + G(\bar{q}_+)\, M_p(\bar{q},\bar{q}') \right]$$

M_n and M_p are given by

$$M_n(\bar{q},\bar{q}') = f_n^*(\bar{q}) \left[f_n(\bar{q}_+)f_p(\bar{q}_-) - \frac{1}{3} g_n(\bar{q}_+)g_p(\bar{q}_-)\hat{n}_{q_+}\cdot\hat{n}_{q_-} \right]$$
$$+ g_n^*(\bar{q}) \left[g_n(\bar{q}_+)f_p(\bar{q}_-)\hat{n}_q\cdot\hat{n}_{q_+} + \frac{1}{3} g_p(\bar{q}_-)f_n(\bar{q}_+)\hat{n}_q\cdot\hat{n}_{q_-} \right.$$
$$\left. + \frac{1}{3} g_n(\bar{q}_+)g_p(\bar{q}_-)\hat{n}_q\cdot(\hat{n}_{q_-}\times\hat{n}_{q_+}) \right]$$

$$M_p(\bar{q},\bar{q}') = f_p^*(\bar{q}) \left[f_n(\bar{q}_+)f_p(\bar{q}_-) - \frac{1}{3} g_n(\bar{q}_+)g_p(\bar{q}_-)\hat{n}_{q_+}\cdot\hat{n}_{q_-} \right]$$
$$+ g_p^*(\bar{q}) \left[g_p(\bar{q}_-)f_n(\bar{q}_+)\hat{n}_q\cdot\hat{n}_{q_-} + \frac{1}{3} g_n(\bar{q}_+)f_p(\bar{q}_-)\hat{n}_q\cdot\hat{n}_{q_+} \right.$$
$$\left. + \frac{1}{3} g_n(\bar{q}_+)g_p(\bar{q}_-)\hat{n}_q\cdot(\hat{n}_{q_+}\times\hat{n}_{q_-}) \right]$$

As in the elastic scattering case, here $\left(\frac{d\sigma}{d\Omega}\right)^S_{Kpn}$ represents the single scattering contribution to the break-up reaction, $\left(\frac{d\sigma}{d\Omega}\right)^{SD}_{Kpn}$ represents the interference between the single and double scattering amplitudes. Again, because of its smallness, we neglect the purely double scattering term. Equations III-30, III-32, and III-34 are the generalizations of Eq. III-12, III-13, and III-18 to include spin effects. Except for the modifications to the factors $G(0)$ and $G(\bar{q})$ in Eq. III-34, discussed in Sec. III-B, these were the equations we used to analyze our data. We dicuss the procedure of this analysis in detail in the next section.

IV. ANALYSIS OF DATA

In this section we describe the method we used to analyze our data. It involves using Eqs. III-30, III-32 and III-34 to do a simultaneous fit to our K^-d elastic scattering and break-up reaction data. In order to do this, we need to know the deuteron form factor and the elastic scattering amplitudes for K^- incident on the proton and on the neutron. We assume that the deuteron form factor is obtained from the Hulthén wave function. We take as the K^-p elastic scattering amplitude two models obtained from fits to experimental data. As the K^--neutron elastic scattering amplitude, we assume two parametrizations, the parameters of which we vary to obtain a fit to our experimental data.

A. Deuteron Form Factor

Various forms of the deuteron wave function can be used to obtain the deuteron form factor.[22] We used in our analysis the Hulthén wave function

$$\psi_D(r) = N \frac{e^{-\alpha r} - e^{-\beta r}}{r} ,$$

where

$$N = \left[\frac{\alpha\beta(\alpha+\beta)}{2\pi(\alpha-\beta)^2} \right]^{1/2} ,$$

and

$$\alpha = 0.0457 \text{ BeV/c} ,$$

$$\beta = 0.237 \text{ BeV/c} .$$

The Fourier transform of the Hulthén wave function is given by

$$\varphi_D(\bar{p}) = N \sqrt{\frac{2}{\pi}} \left[\frac{1}{\alpha^2+p^2} - \frac{1}{\beta^2+p^2} \right] .$$

The deuteron form factor is defined by

$$G(\bar{q}) = \int d^3\bar{r}\ e^{i\bar{q}\cdot\bar{r}}\ |\psi_D(\bar{r})|^2 = \int d^3\bar{p}\ \varphi_D^*(\bar{p})\ \varphi_D(\bar{p}-\bar{q})$$

Carrying out the integrations gives

$$G(\bar{q}) = \frac{2\pi N^2}{q}\left\{\tan^{-1}\left[\frac{4\alpha q}{4\alpha^2-q^2}\right] + \tan^{-1}\left[\frac{4\beta q}{4\beta^2-q^2}\right] - 2\tan^{-1}\left[\frac{2q(\alpha+\beta)}{(\alpha+\beta)^2-q^2}\right]\right\}$$

Here q denote the magnetude of $\bar{q}$. A graph of $G(\bar{q})$ as a function of q^2 is given by the upper curve in Fig. 14.

We also need the function

$$G_{p_o}(\bar{q}) = \int_{p_o} d^3\bar{p}\ \varphi_D^*(\bar{p})\ \varphi_D(\bar{p}-\bar{q})$$

$$= \frac{2N^2}{q}\int_{p_o}^{\infty} pdp\left[\frac{1}{\alpha^2+p^2} - \frac{1}{\beta^2+p^2}\right]\log\left[\frac{\{(p+q)^2+\alpha^2\}\{(p-q)^2+\beta^2\}}{\{(p-q)^2+\alpha^2\}\{(p+q)^2+\beta^2\}}\right]$$

This function appears in the proton and neutron single scattering interference term of the break-up reaction, (Eq. III-34). The lower limit p_o corresponds to the lower cut on the proton momentum we made in our scanning. We note that $G_{p_o}(\bar{q}) = G(\bar{q})$ for $p_o = 0$. $G_{p_o}(\bar{q})$ can be integrated numerically for various values of p_o. A plot of $G_{p_o}(\bar{q})$ as a function of q^2 is given by the lower curve in Fig. 14 for $p_o = 0.095$ BeV/c, the value we used for the lower cut on the proton momentum in our sample of break-up events. Comparing the two curves in Fig. 14, we see that the proton momentum cut affects the low momentum transfer events the most.

B. Two Models of K^-p Elastic Scattering

K^--proton elastic scattering with incident K^- momenta around 1 BeV/c has been studied in detail in three experiments.[23, 24, 25] The authors of Ref. 23 have fitted their data to a model of elastic scattering in the form of a background term plus resonances:

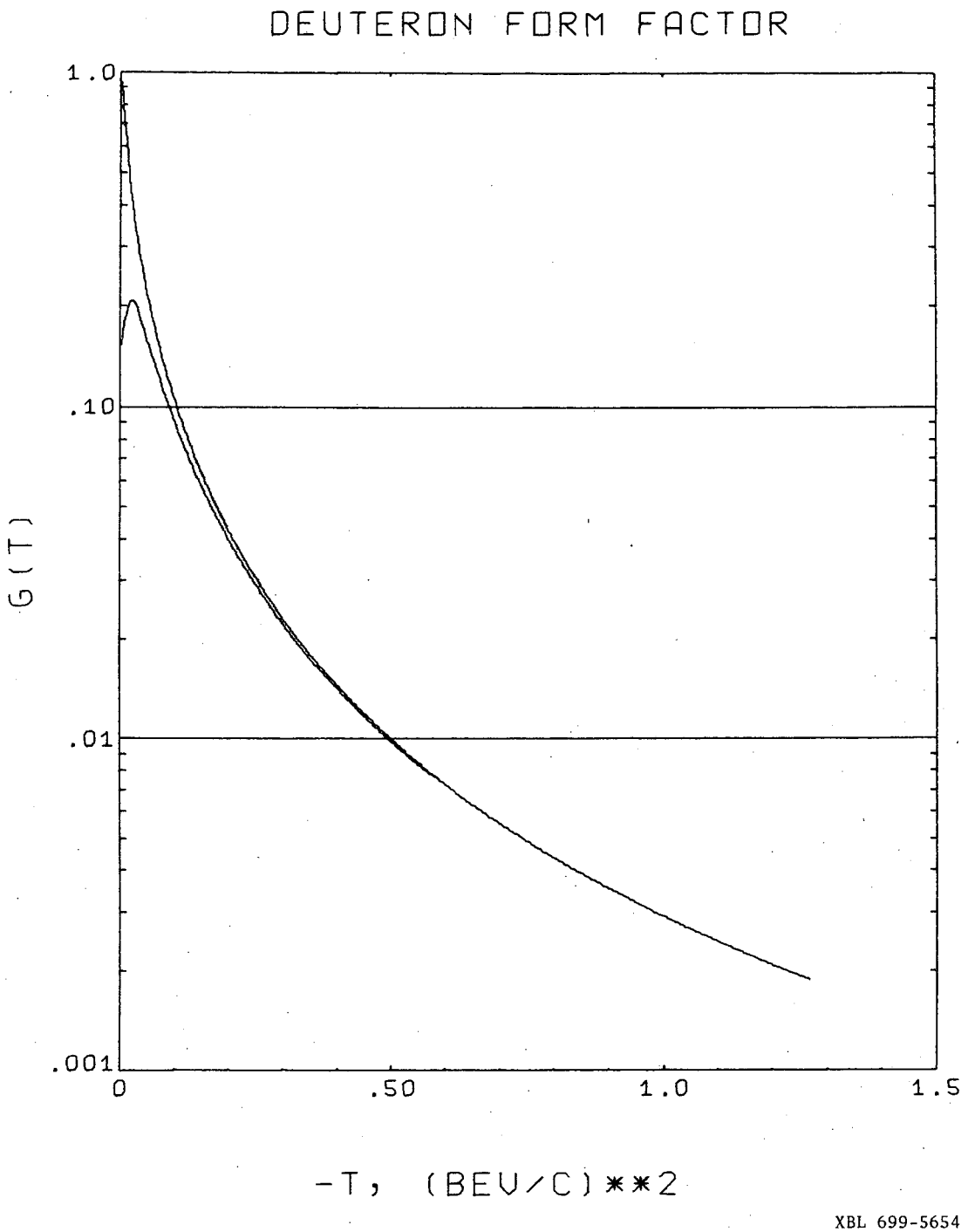

Fig. 14. Upper curve is the deuteron form factor given by the Hulthen wave function. Lower curve is the same form factor modified by the lower spectator momentum cut.

$$f_p = f_b + f_r$$

$$g_p = g_b + g_r \quad .$$

The background terms were parameterized as

$$f_b = \frac{ik\,(a_1 + ia_2)}{\sqrt{\pi k}}\; e^{bt}$$

$$g_b = 0 \quad .$$

The resonant terms were given by

$$f_r = \frac{1}{2}\;(f_1 + f_o)$$

$$g_r = \frac{1}{2}\;(g_1 + g_o) \quad ,$$

where the isospin amplitudes f_I and g_I were given in the standard form

$$f_I = \frac{1}{k}\;\sum_{\ell}\left[(\ell+1)\;T_{I,\ell+} + \ell\;T_{I,\ell-}\right]\;P_\ell(z)$$

$$g_I = \frac{1}{k}\;\sum_{\ell}\left[T_{I,\ell+} - T_{I,\ell-}\right]\;P^1_\ell(z) \qquad \text{(IV-1)}$$

The isospin index I is 0 or 1, z is the cosine of the cm scattering angle, and k the particle momentum in the cm system. For the amplitudes $T_{I,\ell\pm}$ appearing in Eq. IV-1, the authors of Ref. 23 included only the resonant amplitudes of the $Y_1^*(1765)$ and the $Y_0^*(1810)$. All the other terms in Eq. IV-1 were set equal to zero. The resonant amplitudes were parametrized in the usual Breit-Wigner form

$$T = x/(\epsilon - i) \quad ,$$

where $x = \Gamma_e(k)/\Gamma(k)$ is the elasticity of the resonance and $\epsilon = 2(E_R - E)/\Gamma(k)$. The ℓ and k dependences of the widths $\Gamma_e(k)$ and $\Gamma(k)$ were those given in Blatt and Weisskopf.[26] In fitting their data, these

authors varied the parameters b, a_1, a_2, and the resonant masses and widths. From their best fit, they obtained the following values for the resonant parameters:

$$M_2 = 1758 \pm 11 \text{ MeV} \quad , \quad M_3 = 1811 \pm 4 \text{ MeV}$$
$$\Gamma_2 = 113 \pm 25 \text{ MeV} \quad , \quad \Gamma_3 = 73 \pm 10 \text{ MeV}$$
$$x_2 = 0.46 \pm 0.05 \quad , \quad x_3 = 0.67 \pm 0.08$$

where the indices 2 and 3 refer to the orbital angular momentum of the resonances. The values for the parameters of the diffractive background terms were

$$2b = 3.2 \pm 0.13 \text{ (GeV/c)}$$
$$a_1 = 3.73 \pm 0.12 \text{ (mb)}^{3/4}$$
$$a_2 = 0.89 \pm 0.39 \text{ (mb)}^{3/4} \quad .$$

The parametrization of the elastic scattering amplitudes f_p and g_p given above corresponds to separating these amplitudes into contributions from diffractive scattering and from resonances. This combination has been suggested by two experimental facts: 1) The general diffractive nature of the forward portion of the elastic scattering angular distributions and 2) the occurence of numerous resonances within the energy region we are considering. The combination of these two features gives a reasonable description of π-nucleon elastic scattering as well as the K^--nucleon data.[27]

A second model of K^-p elastic scattering has been given in Ref. 24. The full amplitude was given by

$$f_p = (f_1 + f_o)/2$$
$$g_p = (g_1 + g_o)/2 \quad ,$$

where f_I and g_I were defined in Eq. IV-1. To account for the background,

the authors of Ref. 24 assumed that each partial wave amplitude T was a superposition of a background amplitude T_b and a resonant amplitude T_r. (To simplify notation, we suppress the indices I and ℓ that should appear with each T and S occurring in this section.) To insure unitarity, they superposed the two amplitudes by the relation

$$S = S_b \, S_r \quad ,$$

where each S and T are related to δ and η through

$$S = 1 + 2i \, T = \eta \, e^{2i\delta}$$

With this assumption, the partial wave amplitudes turned out to be

$$T = T_b + T_r \, \eta_b e^{2i\delta_b} \quad .$$

The resonant amplitudes T_r were parametrized in the same way as described in the first model. The background amplitudes were given the momentum dependence

$$T_b = a + b_1 \, (P_k - 0.8 \text{ GeV/c}) \quad , \quad \text{for } P_k > 0.8 \text{ GeV/c}$$
$$T_b = a + b_2 \, (P_k - 0.8 \text{ GeV/c}) \quad , \quad \text{for } P_k < 0.8 \text{ GeV/c}$$

where a, b_1, and b_2 are complex parameters varied in the fitting, and P_k the incident K^- lab momentum. The background terms were assumed to come only from the S_{11}, P_{11} and P_{13} waves. Table II lists the different partial waves and their fitted values obtained from the best fit of Ref. 24.

In the analysis of our data, we assume that the K^-p elastic scattering amplitudes are given by either one of the models described above. In the next section, we discuss the two parametrizations for the K^--neutron elastic scattering amplitude.

Table II. Parameters for solution (b) of Ref. 24. The parameter in brackets have been kept fixed. The errors are statistical only.

Non resonant amplitudes	Re a	Im a	Re b_1	Im b_1	Re b_2	Im b_2
S_{01}	0.04 ±0.03	0.81 ±0.02	-0.38 ±0.14	0.01 ±0.06	-	-
S_{11}	0.13 ±0.06	0.55 ±0.02	-0.20 ±0.21	0.34 ±0.09	0.43 ±0.46	0.91 ±0.15
P_{01}	0.11 ±0.04	0.47 ±0.02	-0.76 ±0.20	0.11 ±0.14	-0.31 ±0.30	1.76 ±0.50
P_{11}	0.10 ±0.04	0.02 ±0.01	0.02 ±0.20	0.60 ±0.08	1.07 ±0.06	-0.04 ±0.05
P_{03}	0.38 ±0.03	0.19 ±0.01	-0.49 ±0.09	0.61 ±0.07	0.68 ±0.27	0.40 ±0.08
P_{13}	0.17 ±0.02	0.02 ±0.01	-0.45 ±0.02	0.49 ±0.01	0.79 ±0.22	-0.27 ±0.08

Resonant amplitudes	Mass E_r (MeV)	Width Γ_0 (MeV)	Elasticity
S_{01}	1663 ± 3	26 ± 8	0.14 ± 0.04
D_{03}	1696 ± 3	35 ± 7	0.18 ± 0.03
D_{13}	1668 ± 5	56 ± 18	0.09 ± 0.02
D_{05}	1807 ± 10	123 ± 32	0.09 ± 0.01
D_{15}	1768 ± 2	128 ± 8	0.45 ± 0.01
F_{05}	1817 ± 2	71 ± 4	0.62 ± 0.02
F_{15}	[1910]	[50]	[0.08]
F_{07}	1864 ± 2	39 ± 7	0.12 ± 0.02
F_{17}	[2040]	[150]	[0.25]
G_{07}	[2100]	[160]	[0.25]

C. Parametrizations of the K^--Neutron Elastic Scattering Amplitude

We consider two models for K^--neutron elastic scattering which are similar to the K^-p models described in the previous section. In the first model, we parametrize the K^--neutron amplitude similar to the first K^-p model. We assume the background terms to be given by[28]

$$f_b = \frac{A}{\sqrt{s_n}} \exp(t/4R^2)$$

$$g_b = \frac{B}{\sqrt{s_n}} \left(1 + \frac{t}{4k^2}\right)^{1/2} \sqrt{(-t/4R^2)} \exp(t/4R^2) \quad , \qquad \text{(IV-2)}$$

where the parameters A and B are complex and R is real. R has the interpretation of a root-mean-square radius of interaction, and k is the particle momentum and s_n the K^-n energy in the K^-n center of mass. The constants A, B, and R give us five parameters which we vary to obtain a fit to the data. The full amplitudes is given by

$$f_n = f_b + f_1$$

$$g_n = g_b + g_1$$

where f_1 and g_1 are the isospin 1 resonant amplitudes and are parametrized in the same way as in Eq. IV-1. We include in f_1 and g_1 the resonances $Y_1^*(1660)$, $Y_1^*(1765)$, and $Y_1^*(1910)$. Because of our limited data, the masses and widths of these resonances are not varied in our fitting procedure. They are taken to be those given in Ref. 29. The normalization of f_n and g_n is such that the differential cross-section is given by

$$\frac{d\sigma_n}{d\Omega} = |f_n|^2 + |g_n|^2 \quad .$$

We parametrize our second K^-n elastic scattering model similar to the second K^-p model described in the previous section. Included in the

resonant amplitudes are again the three Y_1^* resonances used in the first K^-n model. Their masses and widths are also fixed at the values given in Ref. 29. As in the K^-p model, we assume the background comes only from the S_{11}, P_{11}, and P_{13} partial waves. Unlike the K^-p model, these waves are not parametrized with an energy dependence. Since we fit each incident momentum separately (see below), this explicit energy dependence can be neglected. We adopt this simpler parametrization in order to reduce the number of fitting parameters. The background waves S_{11}, P_{11}, and P_{13} are considered as complex, thus giving us six parameters with which to fit our data. We take them to be the real and imaginary parts of S_{11}, P_{11}, and P_{13}.

D. Fitting Procedure

1. Definition of the Fitting χ^2

We used a minimization procedure to analyze our data, fitting each incident momentum separately. We assume that the K^-p elastic scattering amplitudes are known and, in fact, are given by either one of the models of Sec. IV-B. This K^-p input is not varied in the fitting. Then using a parametrization of the K^-n amplitudes described in Sec. IV-C, we calculate the K^-d elastic scattering and the break-up reaction cross-sections through Eqs. III-30 and III-34 and compare the results with our experimental data. The comparison is via a χ^2 function, which is defined as

$$\chi^2 = \sum_i \left[\frac{\sigma_i^c - \sigma_i^e}{\Delta\sigma_i} \right]^2 ,$$

where σ_i^c is the calculated cross-section, σ_i^e the corresponding experimental data point, and $\Delta\sigma_i$ the statistical error for the data point. The index i ranges over the experimental data points from both the K^-d elastic scattering and the break-up reaction angular distributions.

The χ^2 is minimized through a variation of the parameters occuring in the K^-n amplitudes. The actual minimization was done by an LRL Computer Library Program VARMIT,[31] a computer routine based on the variable metric method of reaching a minimum of a function.[32]

2. Treatment of Double Scattering Terms

In calculating the K^-d elastic and the break-up reaction cross-sections, we have used Eqs. III-30 and III-34. The double scattering terms in these two equations involve double integrals over intermediate momentum transfers. We neglect the purely double scattering terms, since they contribute less than 1% to the cross-sections.[33] We retain the interference terms between the single and double scattering amplitudes. The double integrations involved in these interference terms have to be carried out numerically during fitting. They require an enormous amount of computer time in each fit (~30 minutes just for checking the gradient of the χ^2 function required for the fitting). Consequently, we adopted an iterative method in order to cut down on running time. In this method, we included only the single scattering terms in our calculation of σ_i^c. These single scattering terms do not involve any integration and so can be computed very quickly. As a 0^{th} order fit, we set the interference terms between single and double scattering amplitudes equal to 0. After completing this fit, we calculated these interference terms and added them to the calculated σ_i^c used for a second fit. After completing the second fit, we re-calculated the interference terms and then added the results to the calculated σ_i^c used for a third fit, and so on. The iterations converged very quickly in the sense that the parameter values and the calculated interference terms did not change very much after the second iteration (less than 5%). In this way, we were able to complete a fit in less than 15 minutes of CDC 6600 computer time.

3. Fermi Momentum Smearing

The effect of Fermi momentum smearing in the break-up reaction shows up in the t-distributions for this reaction. If the target nucleons in the deuteron were at rest, there should be very few events beyond a certain maximum value of -t (corresponding to backward scatters). This maximum value depends on the incident momentum. But experimentally we do see events beyond this maximum value, the number of which can not be ascribed to measurement errors alone. The way to account for this smearing is to take a weighted average of the nucleon cross-sections. This was brought out by Eqs. III-25, III-26, and III-27 and was briefly discussed right after the derivation of these equations in Sec. III-B. As in the case of double scattering, the integrals involved in the smearing procedure require numerical integration. Again this takes up lengthy computer time in each fit. We therefore replaced the integrations by finite sums. Fig. 15 is a typical plot of the Fermi distribution as a function of K^--nucleon cm energy. The highly peaked curve is the distribution without any cut on the spectator momentum. The lower curve is one with a lower cut on the spectator momentum. We note that this latter distribution is essentially flat and is about 120 MeV wide. This is consistent with the energy spread formula

$$\Gamma = 2 P_{lab} \sqrt{\frac{\langle p^2 \rangle}{3m^2}}$$

given by Ref. 21. Here m is the nucleon mass, and $\langle p^2 \rangle$ is the expectation value of p^2 taken between deuteron states. With the Hulthén wave function, $\langle p^2 \rangle = \alpha\beta$, and we get (in BeV units)

$$\Gamma = 0.125 P_{lab} \quad .$$

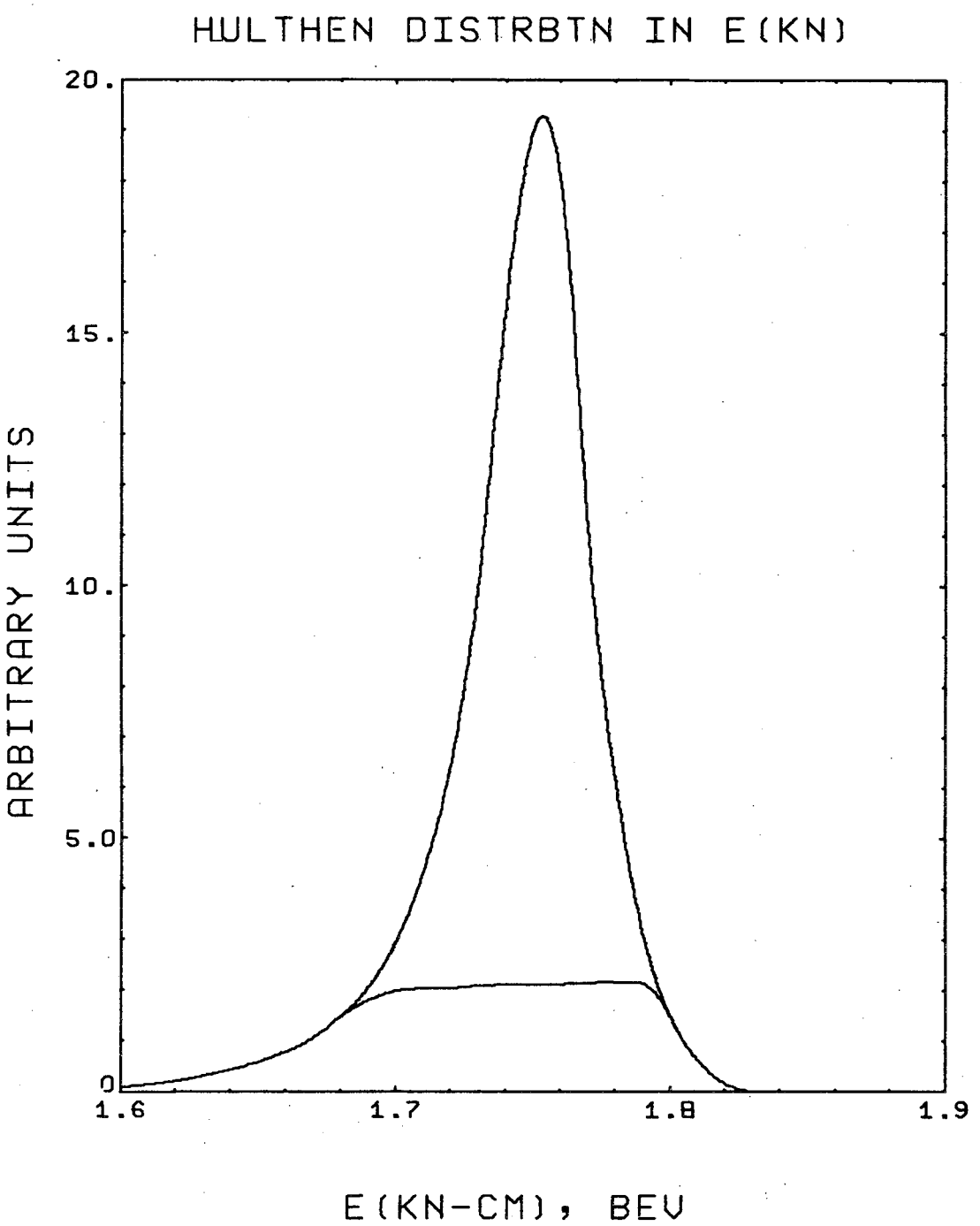

XBL 699-5656

Fig. 15. Upper curve is the Hulthen distribution as a function of the cm energy of the $\bar{K}N$ system at K^- incident momentum 0.91 BeV/c. The lower curve is the same distribution with the low momentum (< 100 MeV/c) spectators excluded.

We subdivided the energy spread interval arising from Fermi motion into smaller intervals and evaluated the nucleon cross-sections at these energy values. We calculated the break-up reaction cross-section by taking a weighted average of these nucleon cross-sections over the entire energy spread. Since the distribution with a spectator momentum cut is essentially flat, we have taken the weights to be equal for each of the energy subintervals. The resulting break-up cross-section was then used in our analysis.

4. Inclusion of Total Cross-Section Data

We have utilized the K^-d and K^-p total cross-section data of Ref. 6 in our analysis. We used these data to fit the total cross-section formula given in Eq. III-32. The extrapolated total cross-sections at our incident momenta were used with the K^-d elastic scattering and break-up reaction data simultaneously in our fit. We note that the cross-section defect $d\sigma$ and the K^-n total cross-section involve fitting parameters. These parameters were varied to obtain an over-all χ^2 for our fit.

E. Results and Discussion

We discuss here the results of our fitting. We have tried the two parametrizations of K^-n elastic scattering given in Sec. IV-C. Using the two models of K^-p elastic scattering discussed in Sec. IV-B with each of these parametriations, we have 4 combinations. For ease of discussion, we denote the 4 cases as follows:

Case I: 1^{st} K^-p model (e^{bt}) with 1^{st} K^-n parametrization (e^{bt})

II: 1^{st} K^-p model (e^{bt}) with 2^{nd} K^-n parametrization (SP wave)

III: 2^{nd} K^-p model (SP wave) with 1^{st} K^-n parametrization (e^{bt})

IV: 2^{nd} K^-p model (SP wave) with 2^{nd} K^-n parametrization (SP wave)

The descriptions within the parentheses pertain to the background amplitudes. Through a comparison of the results obtained in the 4 cases listed here, we first examine to what extend does the fit depend on the model we use. Following this, we discuss what effects does the inclusion of Fermi energy spreading and of double scattering have on our fits. Finally, we display and discuss the angular distributions obtained in the best fit.

1. Comparison of Models

Table III lists the χ^2 of each of the 4 cases of fitting given above, together with the number of degrees of freedom for the χ^2. The χ^2 values given in this table are for the over-all fit to both the K^-d elastic scattering and the break-up reaction data. As can be seen from this table, the χ^2 values are large for the number of degrees of freedom corresponding to them. This is especially noticeable in the case of 910 MeV/c incident momentum. However, as we shall see below, a detailed examination into the fitting gives a better picture. It is found that the K^-d elastic scattering data generally fit well. Large contributions to the χ^2 come from the break-up reaction distributions, especially the large angle region.

One effect due to the choice of K^-p models is evident from Table III. The two fits using the 1^{st} model of K^-p scattering (cases I and II) give smaller χ^2 values than the two using the 2^{nd} K^-p model (cases III and IV).

Table III. Results of fits with Fermi energy spread $\Gamma = 0.125\ P_{lab}$. The errors shown are statistical and do not include those from the K^-p distributions which were taken as input.

Beam Momentum (MeV/c)		810	910	1010	1110
σ_{Kd}^{el} (mb)	I	12.0±0.7	10.7±0.2	11.8±1.6	11.0±0.3
	II	11.7±0.6	11.4±0.7	11.8±0.4	10.3±0.7
	III	11.7±1.4		11.6±0.6	10.6±0.3
	IV	11.5±0.5	11.0±0.8	11.5±0.3	10.5±0.7
σ_{Kn}^{el} (mb)	I	18.3±2.2	13.6±0.7	12.3±2.9	13.6±2.9
	II	16.6±0.7	17.9±1.5	12.8±0.5	14.9±2.4
	III	8.5±1.7		12.9±1.5	15.2±3.4
	IV	10.0±0.6	22.9±1.0	14.2±0.1	14.5±2.4
σ_{Kn}^{tot}(mb)	I	32.5±0.5	39.0±0.4	34.6±0.9	33.0±0.5
	II	33.1±2.2	37.7±2.6	33.3±1.4	31.7±2.3
	III	30.6±0.8		34.7±0.7	33.2±0.2
	IV	31.6±1.8	37.9±2.7	33.5±1.1	31.6±2.3
σ_{Kp}^{tot}(mb)		40.8±0.3	44.1±0.3	50.9±0.4	44.7±0.3
σ_{Kd}^{tot}(mb)		70.4±0.3	79.4±0.3	82.1±0.4	74.0±0.3
χ^2	I	80.7	151.7	25.9	47.2
	II	32.0	148.8	32.6	47.4
	III	109.2		100.2	74.0
	IV	76.8	254.1	59.2	74.7
Degrees of Freedom	I	15	18	18	20
	II	14	17	17	19
	III	15	18	18	20
	IV	14	17	17	19

In fact, the blank entry in this table under 910 MeV/c in case III is due to the fact that we were unable to reach a minimum in this fit. The reason for this was that, using the 2nd K^-p model, the K^-p cross-section gives as large a contribution to the break-up reaction distribution as the experimental data at this incident momentum. Consequently, the fitting would like to make the K^-n contribution as small as possible in order to reduce the χ^2. Case III uses the 1st parametrization of the K^-n amplitude. The parameters that the fit varies in this case are the coefficient and the exponent of the exponential background amplitude (see Sec. IV-C). The coefficient is determined by the total cross-section data to be non-zero. As a result, the only way that the fitting program can minimize the K^-n contribution is to go to as large a negative exponent as possible. This was what actually happened.

Also listed on Table III are the K^-d and K^-n total elastic scattering cross-sections and the K^-n total cross-sections. The elastic cross-sections were obtained from integrating the differential elastic cross-sections calculated in each fit, while the K^-n total cross-sections were obtained from the imaginary part of the K^-n amplitude given by our models. For comparison purposes, we also include in Table III the experimental K^-d and K^-p total cross-sections at the same incident momenta. These values were extrapolated from the data of Ref. 6 (see Fig. 2). As can be seen from Table III, σ_{Kd}^{el} and σ_{Kn}^{tot} remain unchanged (within errors) as we go from Case I through Case IV. This means that these two quantities are model-independent. However, the same can not be said about σ_{Kn}^{el}. Table III indicates that σ_{Kn}^{el} depends on which model of K^-p scattering we use. However, it should be noted also that it is independent of the K^-n models to within errors.

2. Effect of Fermi Energy Spread

To compare the effect of Fermi momentum smearing, we have tried varying the width of the energy spread used in calculating the break-up reaction cross-section. The results in Table III were obtained with a width given by

$$\Gamma = 0.125\ P_{lab}$$

Table IV shows the corresponding results obtained with an energy spread given by

$$\Gamma = 0.085\ P_{lab}$$

Finally, Table V shows the results obtained with no Fermi energy spread (equivalent to having the initial nucleons at rest). As can be seen from a comparison of χ^2 given in Tables III and V, the largest difference between fits with a Fermi energy spread and those with no spread is in the 1010 MeV/c data. On an over-all basis, fits with an energy spread do give a slightly improved χ^2. In all three energy spreads used, the results for σ_{Kd}^{el} and σ_{Kn}^{tot} remain the same within errors. (See Tables III, IV, and V.) This is also true in the case of σ_{Kn}^{el}, even though it was found above to depend on the K^-p models used.

3. Effect of Double Scattering

We plot in Figs. 16 and 17 the interference term between single and double scattering for K^-d elastic scattering and the break-up reaction, respectively. The lower curves in each graph give the negative of the interference term, the upper curves the total value of the corresponding cross-sections. As can be seen from these figures the break-up reaction interference term (which extends below each graph for -t greater than the horizontal intercept) is relatively unimportant. But the elastic scattering interference term range from a few per cent of the complete cross-section

Table IV. Results of fits with Fermi energy spread $\Gamma = 0.085\ P_{lab}$.

Beam Momentum (Mev/c)		810	910	1010	1110
σ_{Kd}^{el} (mb)	I	12.1±0.7	10.6±0.2	11.4±0.6	10.2±0.4
	II	11.5±0.7	11.3±0.8	11.8±0.3	10.3±0.7
	III	11.7±1.4		11.7±1.0	10.4±0.4
	IV	11.5±0.6	11.0±0.8	11.4±0.4	10.5±0.6
σ_{Kn}^{el} (mb)	I	18.4±2.0	13.5±0.7	12.0±1.4	13.9±2.8
	II	15.8±0.8	19.1±1.7	12.7±0.1	14.4±2.0
	III	8.5±1.7		12.4±1.8	15.2±3.0
	IV	10.0±0.7	23.8±1.4	14.6±0.1	14.0±1.9
σ_{Kn}^{tot} (mb)	I	32.5±0.4	39.0±0.3	35.2±0.8	32.8±0.6
	II	33.1±2.2	37.6±2.6	32.9±0.9	31.7±2.2
	III	30.6±0.8		34.6±0.7	33.2±0.4
	IV	31.7±1.9	37.8±2.8	33.3±1.2	31.5±2.1
χ^2	I	62.5	162.0	53.0	42.6
	II	26.0	153.2	49.1	49.9
	III	91.5		151.4	81.1
	IV	65.5	223.5	86.1	81.8

Table V. Results of fits with no Fermi energy spread.

Beam Momentum (Mev/c)		810	910	1010	1110
σ_{Kd}^{el} (mb)	I	12.1±0.6	10.5±0.3	11.6±0.2	10.5±0.4
	II	11.6±0.7	11.3±0.6	11.8±0.3	10.4±0.7
	III	11.9±1.3		11.5±0.6	10.3±0.4
	IV	11.0±0.6	10.9±0.7	11.5±0.3	10.5±0.5
σ_{Kn}^{el} (mb)	I	18.0±2.0	13.0±0.6	14.7±1.4	10.5±0.5
	II	15.8±0.9	21.1±1.3	13.2±0.1	14.2±1.9
	III	8.5±1.6		12.7±1.3	15.8±3.0
	IV	10.4±0.7	25.3±1.1	15.6±0.2	13.6±1.3
σ_{Kn}^{tot} (mb)	I	32.5±0.4	39.0±0.4	34.3±0.8	35.0±0.4
	II	33.1±2.4	37.3±2.0	32.5±1.0	31.9±2.2
	III	30.4±0.7		34.4±0.2	33.2±0.3
	IV	31.7±2.0	37.7±2.4	33.3±1.1	31.4±1.8
χ^2	I	49.8	220.1	158.2	32.4
	II	19.8	185.7	119.4	50.1
	III	94.7		291.6	106.5
	IV	80.9	194.9	152.9	100.7

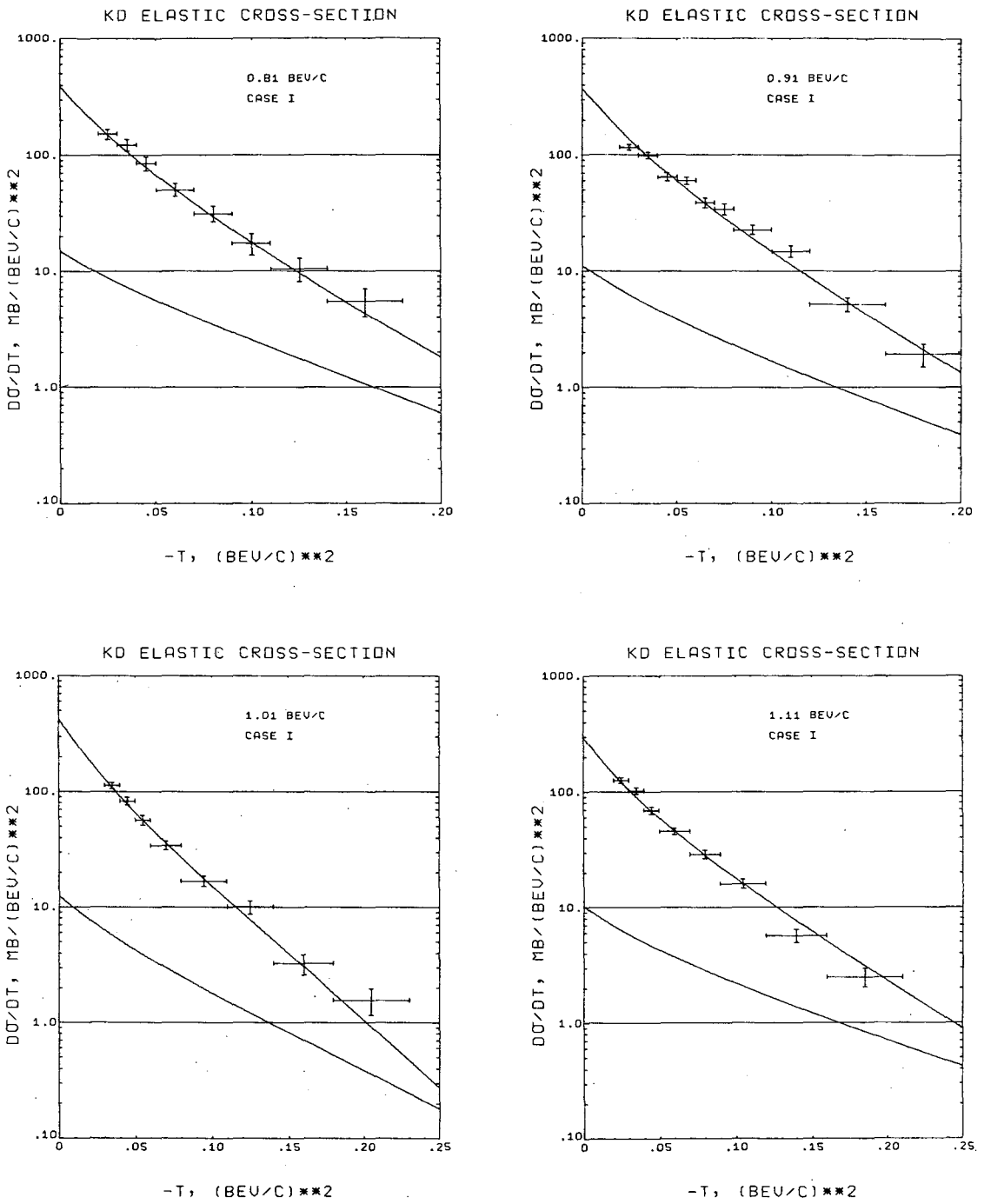

XBL 699-5690

Fig. 16. $K^-d \to K^-d$ angular distributions. Data points are from our experiment. Curves through this data points are from our fits in Case I. Lower curves in each graph give the K^-d elastic single and double scattering interference term.

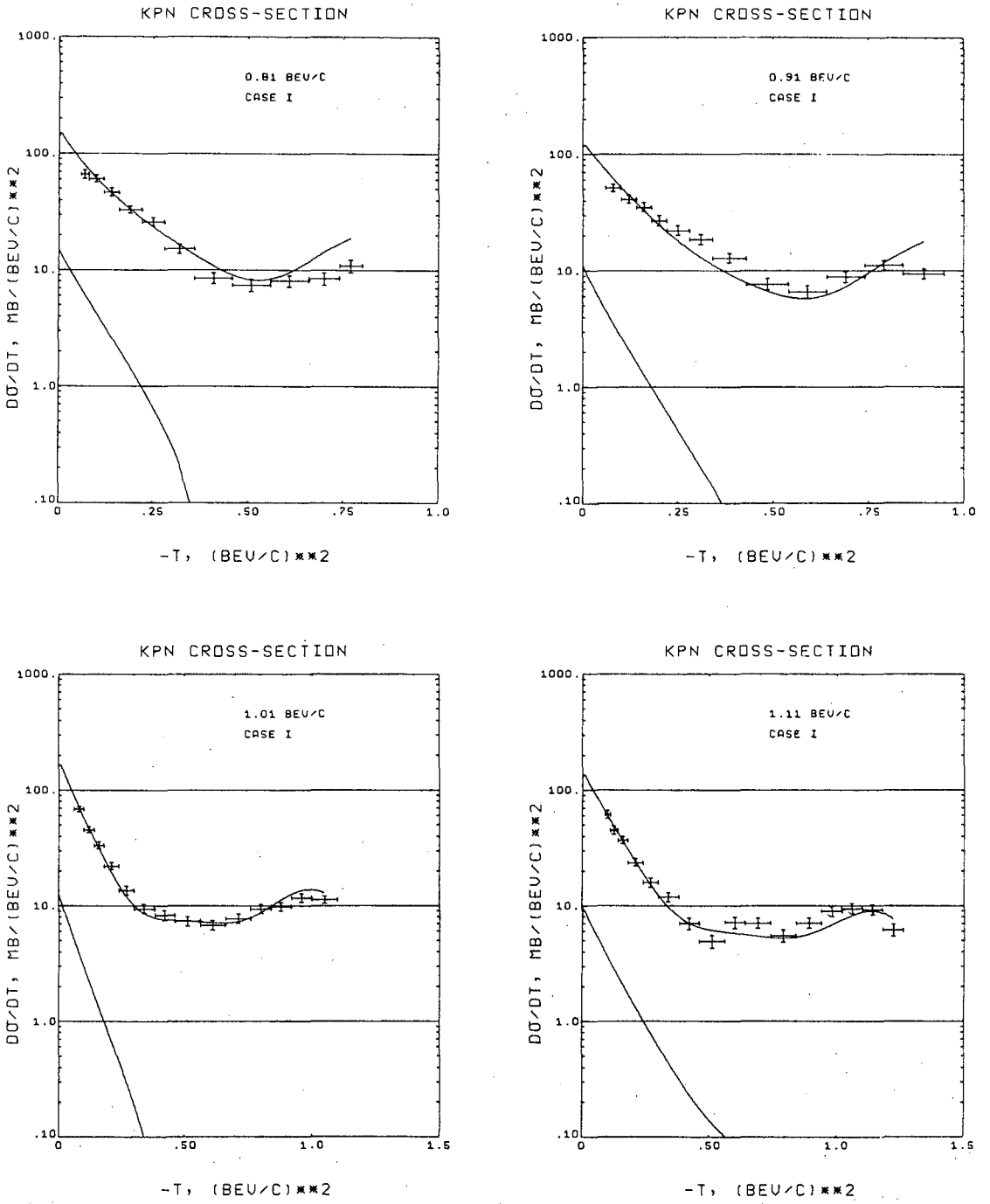

XBL 699-5687

Fig. 17. $\bar{K}d \rightarrow \bar{K}pn$ angular distributions. Data points are from our experiment. Curves through these data points from fit of Case I. Lower curves in each graph give the break-up reaction single and double scattering interference term.

at small angles to above 30% at larger angles. The over-all effect of these interference terms on the fitted curves is barely noticeable when we make a comparison between the distributions fitted with these interference terms and those obtained with no interference terms. This is reflected in the small change in χ^2 values in each case. These χ^2 values are given in Tables VI and VII for cases I and II, respectively. However the fitting parameters, given in Tables VI and VII, are very sensitive to these changes. These results show up in the K^-n angular distributions, which we plot in Fig. 18 for Case I. The solid curves are the K^-n elastic scattering cross-sections obtained from fits which included the interference terms, the dashed curves from fits not using these terms. The data points with error bars are the K^-n distributions obtained from our break-up reaction events with the requirements that the proton momentum is less than 250 MeV/c (i.e. spectator proton) and the neutron momentum is greater than 250 MeV/c (non-spectator nuetron). The data points are normalized to the solid curves within the interval between -1.0 and 0.6.

4. Angular Distributions

Figure 16 shows the angular distributions in -t for the K^-d elastic scattering reaction. The data points shown with error bars are our experimental points. The smooth curves are taken from our simultaneous fits given by Case I. Figure 16 shows that the fits to the K^-d elastic scattering data are generally reasonable. The χ^2 for just these elastic scattering data points turns out to be about the same as the number of these data points. This holds true even for the 910 MeV/c data, though the over-all χ^2 at this incident momentum turned out to be large (see Table III).

This tendency for elastic scattering data to fit well holds true

Table VI. Parameter values obtained in Case I.
R, A, B refer to parameters given in Eq. IV-2.

Fit with single-double scattering interference term.

Momentum (Mev/c)	810	910	1010	1110
$1/(\sqrt{2}\,R)$ $(Bev/c)^{-1}$	3.28±0.20	5.78±0.47	5.04±1.18	2.35±0.18
ReA $(mb\text{-}Bev^2)^{1/2}$	1.00±0.13	-0.46±0.31	-0.38±0.90	0.36±0.10
ImA $(mb\text{-}Bev^2)^{1/2}$	1.55±0.03	0.95±0.03	1.26±0.07	2.00±0.04
ReB $(mb\text{-}Bev^2)^{1/2}$	1.69±0.50	-0.10±1.30	-0.70±1.70	2.61±0.99
ImB $(mb\text{-}Bev^2)^{1/2}$	0.92±0.26	0.39±0.70	0.99±1.05	-1.94±1.17
χ^2	80.7	151.7	25.9	47.2

Fit without single-double scattering interference term.

Momentum (MeV/c)	810	910	1010	1110
$1/(\sqrt{2}\,R)$ $(Bev/c)^{-1}$	3.35±0.24	8.13±1.10	7.75±0.92	3.69±0.19
ReA $(mb\text{-}Bev^2)^{1/2}$	0.85±0.15	-0.57±0.71	-1.49±1.25	1.36±0.12
ImA $(mb\text{-}Bev^2)^{1/2}$	1.55±0.01	0.94±0.03	1.20±0.05	2.14±0.03
ReB $(mb\text{-}Bev^2)^{1/2}$	1.16±0.52	-0.13±1.65	-2.94±4.84	-0.53±0.41
ImB $(mb\text{-}Bev^2)^{1/2}$	0.64±0.30	1.60±1.42	-3.58±5.03	1.00±0.82
χ^2	82.6	153.6	23.5	50.8

Table VII. Parameter values obtained in Case II. S_{11}, P_{11}, P_{13} are the three background waves used in the 2nd K^-n parametrization.

Fit with single-double scattering interference term.				
Momentum (BeV/c)	810	910	1010	1110
Re S_{11}	0.29±0.05	-0.04±0.07	0.17±0.06	0.31±0.05
Im S_{11}	0.23±0.04	-0.24±0.04	0.14±0.04	0.13±0.05
Re P_{11}	0.31±0.03	0.07±0.06	0.11±0.02	0.02±0.07
Im P_{11}	0.26±0.03	0.27±0.05	0.27±0.03	0.45±0.06
Re P_{13}	0.07±0.06	-0.14±0.10	0.06±0.05	-0.04±0.10
Im P_{13}	0.14±0.05	0.23±0.08	0.13±0.05	0.44±0.09
χ^2	32.0	148.8	32.6	47.4
Fit without single-double scattering interference term.				
Momentum (BeV/c)	810	910	1010	1110
Re S_{11}	0.18±0.05	-0.03±0.06	0.20±0.06	0.35±0.05
Im S_{11}	0.22±0.03	-0.29±0.02	0.06±0.05	0.10±0.04
Re P_{11}	0.22±0.03	0.06±0.05	0.11±0.04	0.04±0.06
Im P_{11}	0.24±0.02	0.22±0.03	0.26±0.03	0.45±0.05
Re P_{13}	0.05±0.05	-0.10±0.08	0.03±0.07	-0.01±0.09
Im P_{13}	0.16±0.04	0.34±0.05	0.15±0.05	0.43±0.08
χ^2	52.3	194.6	66.2	76.2

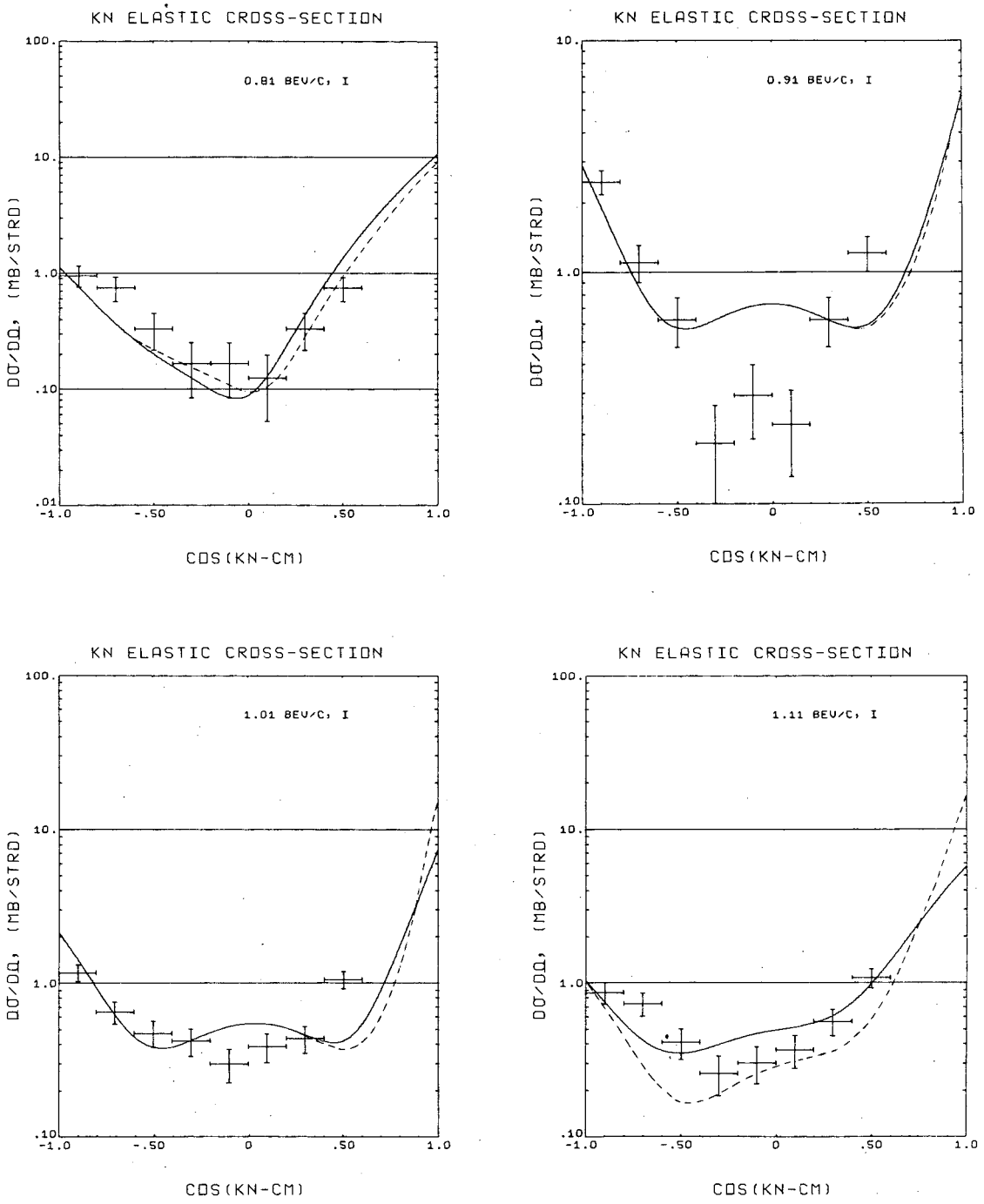

XBL 699-5691

Fig. 18. K^-n elastic scattering angular distributions. Data points are impulse approximation K^-n distributions from our experiment. Solid curves are from fit of Case I with single-double scattering interference terms. Dashed curves are without these terms.

generally for all our fits. The large contributions to the over-all χ^2 come invariably from the break-up reaction distribution, particularly the large -t region. Figure 19 shows the break-up reaction data. Again the points with error bars are the experimental points. The solid curves shown result from fits of Case I with a Fermi energy spread $\Gamma = 0.125\ P_{lab}$. The dashed curves are the break-up reaction cross-sections obtained with no energy spread. Figure 19 shows that the fits to the data at 1010 MeV/c comes out rather well. The fits at 810 MeV/c and at 1110 MeV/c are not as good. And the one at 910 MeV/c is completely off. All these results are reflected in the over-all χ^2 values given in Table III.

As pointed out in the previous paragraph, large χ^2 contributions come from data points at large -t values. In Case I, which gives the results of Fig. 19, we are using a K^-n model with an exponential parametrization for the background amplitude. This term goes as e^{bt} (see Sec. IV-C). At large negative t, this background contribution to the K^-n amplitude is small. Essentially, there are no parameters to vary to fit the data points at large scattering angles. The contributions to the break-up reaction cross-section in this region come mainly from the non-varying resonant part of the K^-n amplitude and from the fixed input of the K^-p distribution. Consequently, there are two possible reasons connected with the large χ^2 contributions coming from data points in this large-angle region. One of these is connected with the K^-p amplitude, the other with the K^-n amplitude. In the case of K^-p, the K^-p elastic scattering distributions given by the K^-p models discussed in Sec. IV-B may be too high in the backward region. This is especially true at 910 MeV/c. We show in Fig. 20 the K^-p distributions used as input in our fitting. The solid curves are from the 1st K^-p model, the dashed curves from the 2nd. The data points shown are from our experiment, obtained with the impulse

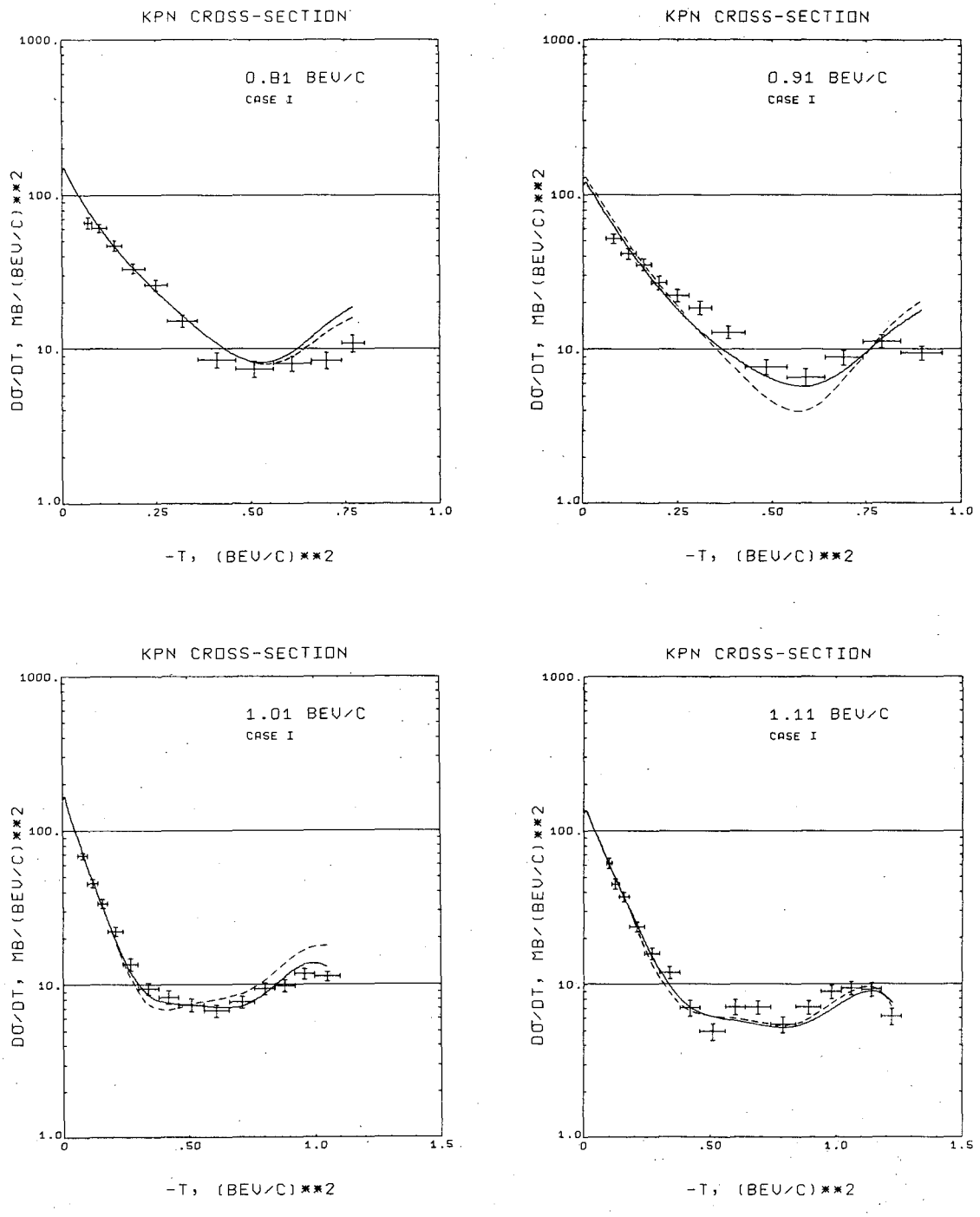

XBL 699-5649

Fig. 19. $K^- d \rightarrow K^- pn$ angular distributions. Data points are from our experiment. Solid curves are from fit of Case I with Fermi energy spread. Dashed curves are without Fermi energy spread.

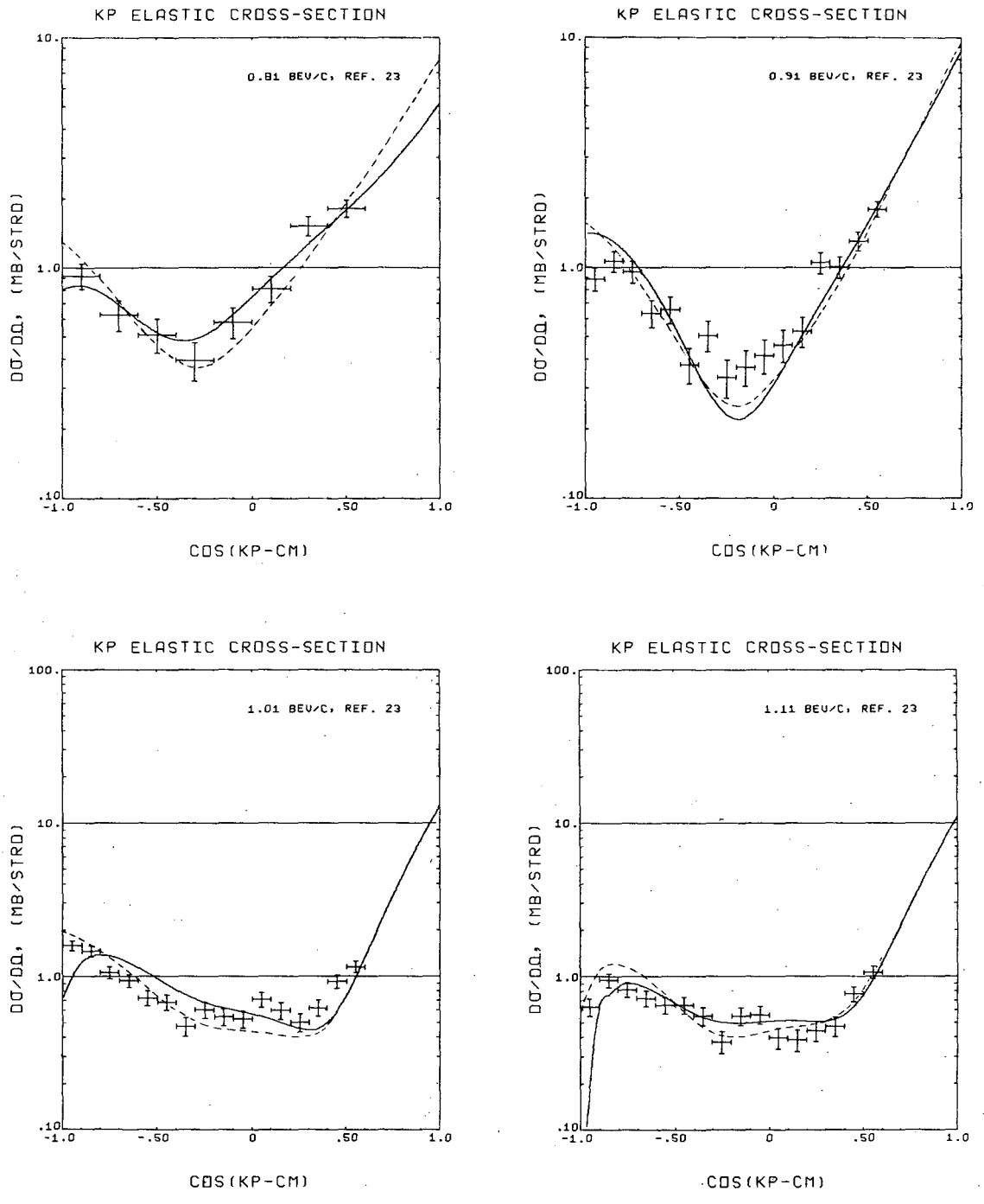

XBL 699-5685

Fig. 20. K^-p elastic cross-sections. Data points are K^-p impulse approximation distributions from our experiment. Solid curves are calculated from the 1st K^-p model, dashed curves from the 2nd K^-p model.

approximation method described in Sec. IV-E-3. We have compared the K^-p angular distribution calculated from the 1st K^-p model at 910 MeV/c momentum with the experimental distribution given by Ref. 25. The results indicate that the calculated distribution is higher by about 20 to 30% in the backward region. This could account for part of the discrepancy at large -t in our fit. In the case of the K^-n amplitude, there are indications that other Y_1^* resonances occur around the 910 MeV/c region besides the $Y_1^*(1660)$ and the $Y_1^*(1765)$ used in our parametrization.[34] If this were the case, our K^-n amplitude should also include these. There is then a possibility that the K^-n amplitude may be different in the backward direction, depending on the spin-parity assignments and the branching-ratio of these new resonances into the $\bar{K}N$ channel. This may also account for part of the discrepancy in our fit.

In contrast to Case I, which has zero degree of freedom in fitting the data points at large -t, Case II does have a certain freedom in this region. In Case II, the K^-p amplitudes remained the same as in Case I. However, the K^-n background amplitude included the S_{11}, P_{11}, and P_{13} waves instead of an exponential. These three partial waves afforded some latitude in fitting the large -t data points. The results of the fitting are given by the solid curves in Fig. 21. The dashed curves in this figure are from the results of Case I. The χ^2 values are improved, as shown in Table III. However, this is accomplished at the expense of the K^-n angular distributions, which we show in Fig. 22. The solid curves in this figure are the K^-n elastic scattering angular distributions obtained in Case I. The dahsed curves are from Case II. The data points are impulse approximation results, as described in Sec. IV-E-3.

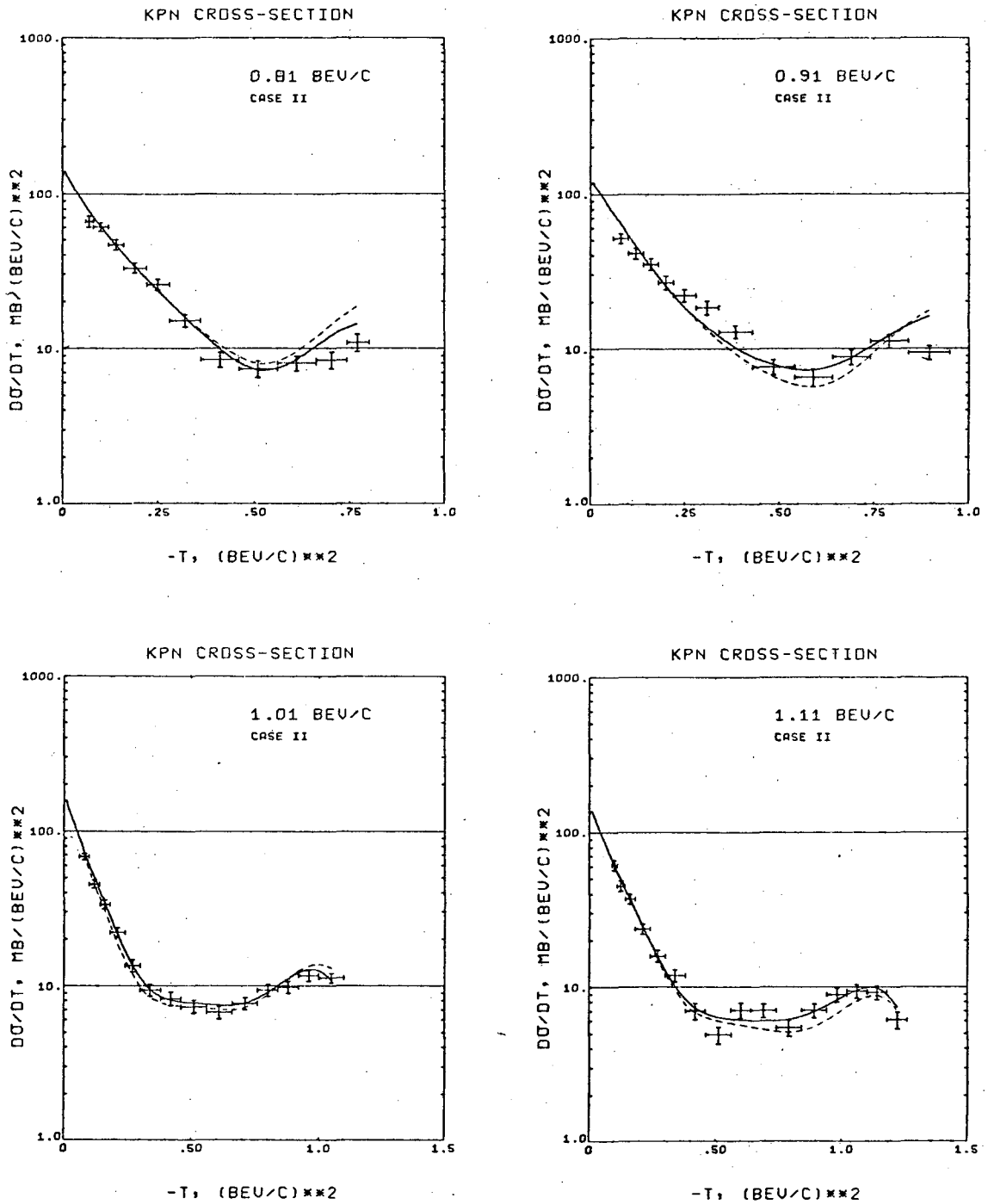

XBL 699-5688

Fig. 21. $K^- d \rightarrow K^- pn$ angulars distributions. Solid curves from fit of Case II, dashed curves from fit of Case I.

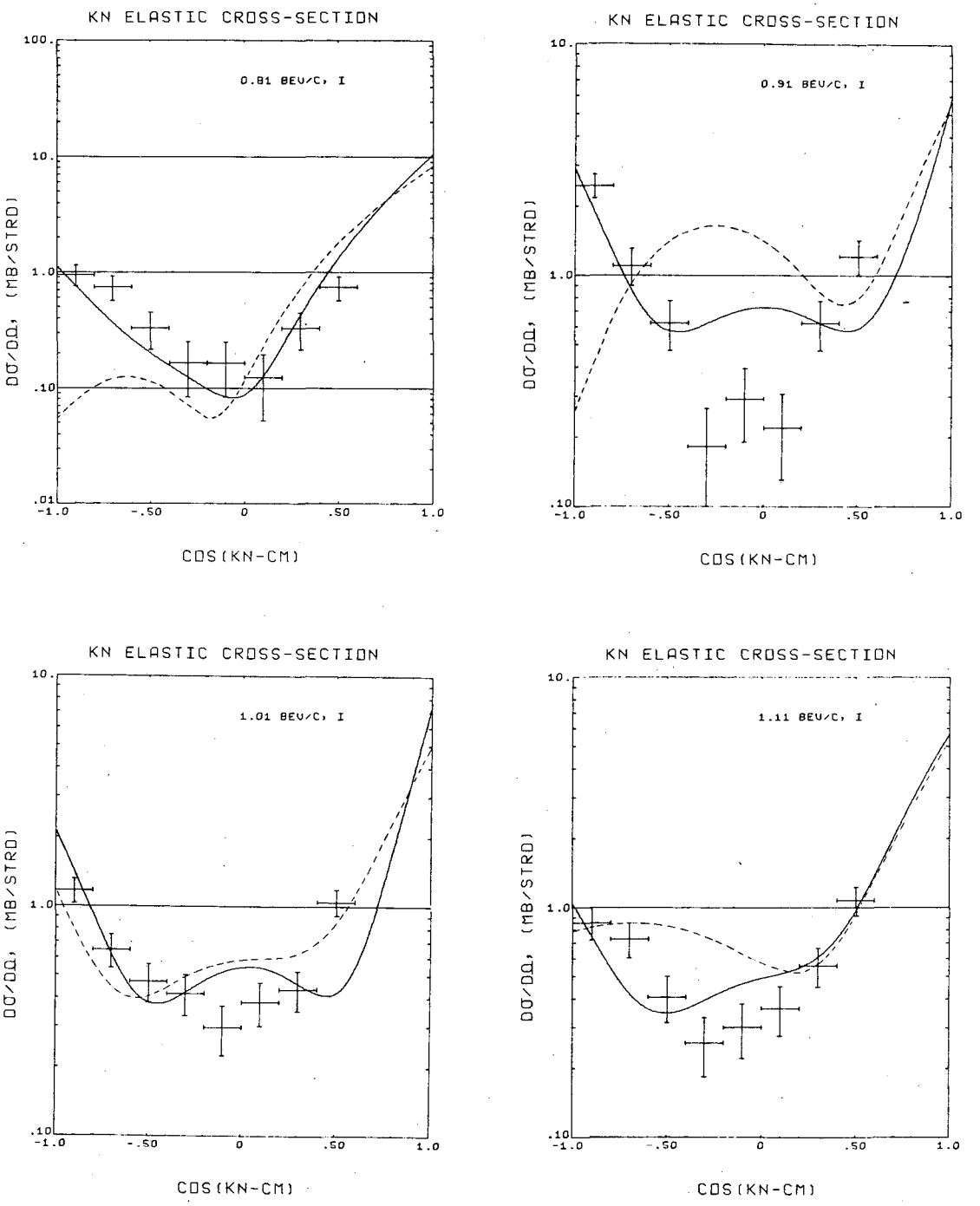

XBL 699-5686

Fig. 22. K^-n elastic cross-sections. Solid curves from fit of Case I, dashed curves from fit of Case II. Data points are the impulse approximation K^-n distributions from our experiment.

From Fig. 22, we see that the Case II distributions (dashed curves) are depressed at large angles so as to give a better fit to the K^-pn distributions in the large angle region. This again reflects the possibility that the input K^-p distributions are high in the large angle region.

For completeness, we include in Table VIII the angular distributions for $K^-d \rightarrow K^-d$. We show in Fig. 23 the calculated $K^-d \rightarrow K^-pn$ angular distributions with no cut on the proton momentum. These curves are from Case I.

Table VIII. K^-d elastic scattering angular distributions.

810 MeV/c		910 MeV/c	
$-t$ $(BeV/c)^2$	$(d\sigma/dt)$ $mb/(BeV/c)^2$	$-t$ $(BeV/c)^2$	$(d\sigma/dt)$ $mb/(BeV/c)^2$
0.02 0.03	150.7±15.3	0.02 0.03	114.6±6.6
0.03 0.04	121.2±13.7	0.03 0.04	97.5±6.1
0.04 0.05	83.9±11.4	0.04 0.05	64.0±5.1
0.05 0.07	49.7±6.2	0.05 0.06	59.4±4.8
0.07 0.09	31.1±4.9	0.06 0.07	38.5±3.8
0.09 0.11	17.1±3.6	0.07 0.08	33.9±3.6
0.11 0.14	10.4±2.3	0.08 0.10	22.5±2.1
0.14 0.18	5.4±1.5	0.10 0.12	14.7±1.7
		0.12 0.16	5.1±0.7
		0.16 0.20	1.9±0.4
1010 MeV/c		1110 MeV/c	
0.03 0.04	111.8±7.6	0.02 0.03	124.1±7.0
0.04 0.05	82.0±6.5	0.03 0.04	100.7±6.3
0.05 0.06	56.2±5.3	0.04 0.05	68.2±5.2
0.06 0.08	33.8±3.0	0.05 0.07	45.0±3.0
0.08 0.11	16.7±1.7	0.07 0.09	28.4±2.4
0.11 0.14	10.0±1.3	0.09 0.12	15.9±1.4
0.14 0.18	3.2±0.6	0.12 0.16	5.7±0.7
0.18 0.23	1.6±0.4	0.16 0.21	2.5±0.4

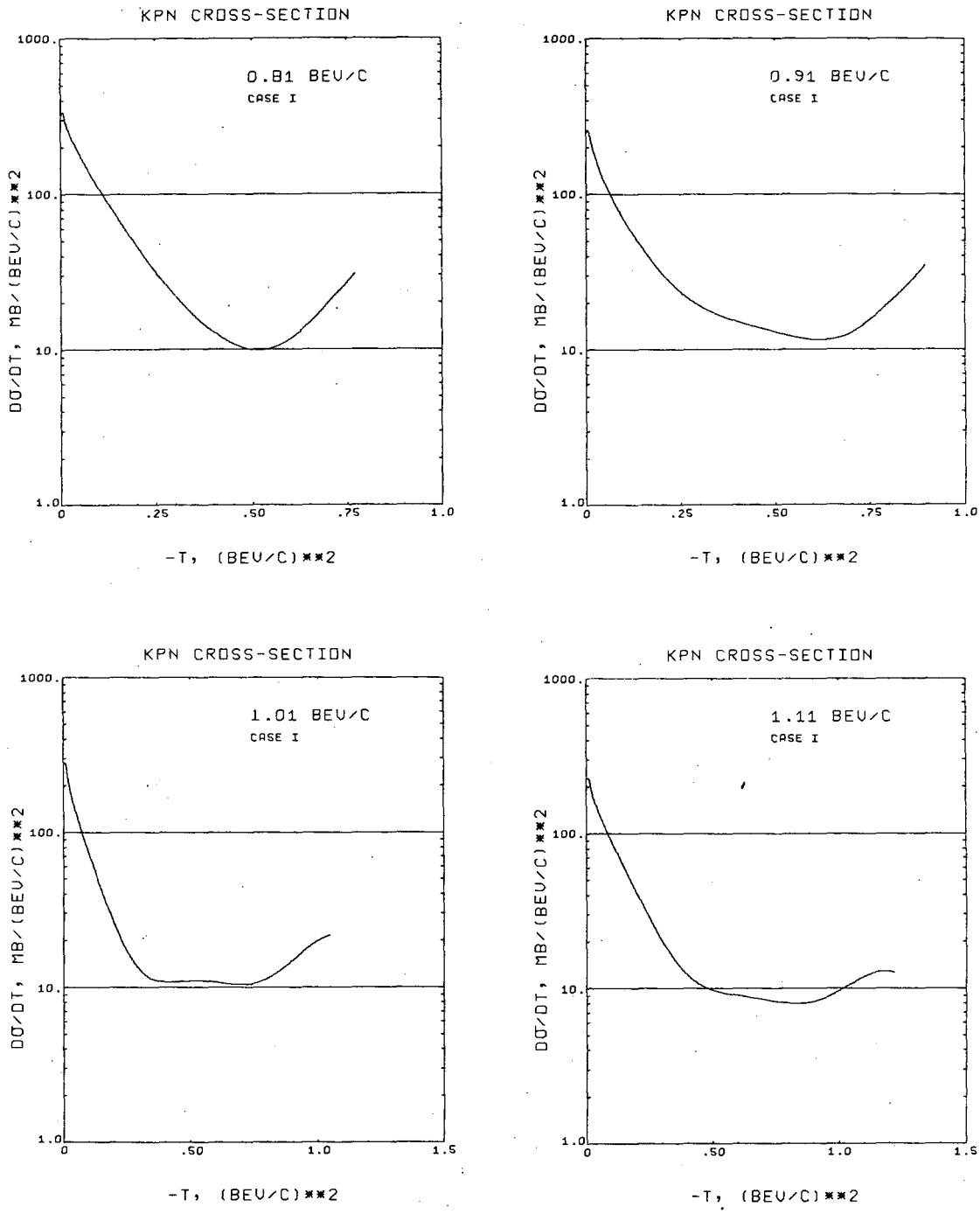

XBL 699-5689

Fig. 23. Calculated $K^- d \rightarrow K^- pn$ angular distributions with no cut on the proton momentum.

V. SUMMARY AND CONCLUSIONS

We have presented experimental angular distributions for the reactions $K^-d \to K^-d$ and $K^-d \to K^-pn$ at four incident K^- momenta. To analyze this data, use was made of Glauber's impact parameter formalism for K^--deuteron scattering. The break-up reaction cross-section formula was modified to take into account the proton momentum cut made in the scanning. We chose to do this by looking at diagrams corresponding to the break-up process. Using this method, we obtained the modifications to the cross-section formula arising from the proton momentum cut. In addition, we obtained modifications which arise from the difference in flux factors between K^--deuteron and K^--nucleon scattering and from the smearing of the nucleon cross-sections due to Fermi momentum. Finally, we extended this formalism to include spin dependence.

Using this formalism thus modified, we fitted our K^-d elastic scattering and break-up reaction data simultaneously. The deuteron cross-section formulae were expressed in terms of the K^-p and K^-n amplitudes. We input into these formulae the K^-p amplitudes from two models based on experiment. The K^-n amplitudes were parametrized with a variable background on top of fixed resonances. The background parameters were varied to get a fit to our data.

We have tried incorporating Fermi smearing and double scattering into our fits. Comparing the results, we found that the inclusion of Fermi smearing in the break-up reaction improved the χ^2. The effect of double scattering is small in this reaction, but is sizeable in the K^-d elastic scattering, becoming more important as -t gets large. The inclusion of double scattering also improved the fit in most cases.

Of the 4 combinations of fits, we tend to favor Case I. Though

Case II gave somewhat smaller χ^2 values, the fact that the K^-n elastic scattering distributions are lower at large angles than the experimental K^-n distributions obtained with a simple impulse approximation (see Fig. 22) makes Case II less attractive. The improvement in χ^2 in Case II comes from the freedom that Case II parameters have in the large angle region, which may contain uncertainties in the K^-p distributions. Case I does not have this freedom. As a result, it is less susceptible to the K^-p uncertainties in this region. The K^-n elastic distributions resulting from Case I also conform in shape to the experimental impulse approximation K^-n distributions, as shown in Fig. 22.

From our fits, we found that the total K^-d elastic cross-section σ_{Kd}^{el} and the K^-n total cross section σ_{Kn}^{tot} were independent of the K^-p and K^-n models we used. The reason for this is clear. Ultimately, these two quantities are tied through the optical theorem to the K^-d and K^-p total cross-sections, which we input and which are more precisely known. Consequently, these two quantities are less affected by the uncertainties present in our models. On the other hand, σ_{Kn}^{el} showed a marked model-dependence. From the values given in Table III, its dependence on the K^-p models is obvious. (Compare Cases I and II with cases III and IV.) Its dependence on the K^-n models is less clear cut. But from the difference in the two K^-n angular distributions (from which σ_{Kn}^{el} is obtained) shown on each graph in Fig. 22, we see that there is a dependence. As pointed out at the end of Sec. IV-E-4, the difference in the two distributions given by the solid and the dashed curves in Fig. 22 result from the K^-n amplitude compensating the K^-p amplitude to fit the K^-pn distributions at large angles. Thus we find that our determination of the K^-n amplitudes depends critically on the input K^-p models (which had no variable parameters). One way to remedy this is

to use actual experimental K^-p and/or charge exchange data and to do a simultaneous fit with both the K^-p and the K^-n amplitudes free to vary. The possibility of doing this is now being investigated.

APPENDIX A

We derive in this Appendix the expression for the scattering amplitude as given by Eq. III-2. The Schrödinger equation can be written as ($\hbar$=c=1)

$$(\nabla^2+k^2)\psi(\bar{r}) = U(\bar{r})\psi(\bar{r}) \quad , \tag{A-1}$$

where $k^2 = 2\mu E$, $U(\bar{r}) = 2\mu V(\bar{r})$, and $\mu = m_1 m_2/(m_1+m_2)$ is the reduced mass. The definition of the scattering amplitude $A(\bar{k}_f,\bar{k}_i)$ is given through the asymptotic wave function

$$\psi(\bar{r}) \xrightarrow{r\to\infty} e^{i\bar{k}_i\cdot\bar{r}} + A(\bar{k}_f,\bar{k}_i)\,\frac{e^{ikr}}{r} \quad , \tag{A-2}$$

where $\bar{k}_i$ is the incident momentum, $\bar{k}_f$ the final momentum, and $k = |\bar{k}_i| = |\bar{k}_f|$ (elastic scattering). We define a function $\nu(\bar{r})$ through

$$\psi(\bar{r}) = e^{i\bar{k}_i\cdot\bar{r}} + \nu(\bar{r})$$

Then Eq. A-2 implies

$$\nu(\bar{r}) \xrightarrow{r\to\infty} A(\bar{k}_f,\bar{k}_i)\,\frac{e^{ikr}}{r} \quad . \tag{A-3}$$

Eq. A-1 can now be written as

$$(\nabla^2+k^2)\,\nu(\bar{r}) = U(\bar{r})\,\psi(\bar{r}) \quad . \tag{A-4}$$

The Green's function for this equation is given by

$$G(\bar{r},\bar{r}') = -\frac{1}{4\pi}\,\frac{e^{ik|\bar{r}-\bar{r}'|}}{|\bar{r}-\bar{r}'|} \quad .$$

Using this, the solution $\nu(\bar{r})$ for Eq. A-4 is then given by

$$\nu(\bar{r}) = -\frac{1}{4\pi}\int d^3\bar{r}'\,\frac{e^{ik|\bar{r}-\bar{r}'|}}{|\bar{r}-\bar{r}'|}\,U(\bar{r}')\,\psi(\bar{r}') \quad . \tag{A-5}$$

For $r\to\infty$, $|\bar{r}-\bar{r}'| \to (r^2-2r\,r'\cos\theta)^{1/2} \to (r-r'\cos\theta)$, where $\cos\theta = \frac{\bar{r}\cdot\bar{r}'}{rr'}$.

Using this, Eq. A-5 becomes

$$\nu(\bar{r}) \xrightarrow{r\to\infty} -\frac{1}{4\pi}\frac{e^{ikr}}{r}\int d^3\bar{r}'\ e^{-ikr'\cos\theta}U(\bar{r}')\psi(\bar{r}') \quad .$$

Comparing with Eq. A-3, we get

$$A(\bar{k}_f,\bar{k}_i) = -\frac{1}{4\pi}\int d^3r'\ e^{-ikr'\cos\theta}\ U(\bar{r}')\psi(\bar{r}') \quad .$$

We note that $kr'\cos\theta = \bar{k}_f\cdot\bar{r}'$ (since θ is the angle between $\bar{r}'$ and $\bar{r}$, and $\bar{r}$ is the position vector of the scattered particle). Thus we finally arrive at Eq. III-2,

$$A(\bar{k}_f,\bar{k}_i) = -\frac{1}{4\pi}\int d^3\bar{r}'\ e^{\bar{k}_f\cdot\bar{r}'}U(\bar{r}')\psi(\bar{r}') \quad .$$

APPENDIX B

In this Appendix, we furnish the steps by which we go from Eq. III-8 to Eq. III-9. Rewriting Eq. III-8, we get

$$A_{fi}(\bar{q}) = \frac{ik}{2\pi}\int d^2\bar{b}\; e^{i\bar{q}\cdot\bar{b}} \int d^3\bar{r}\; \psi_f^*(\bar{r})\psi_i(\bar{r}) \quad x$$

$$x\left[\frac{1}{2\pi ik}\int d^2\bar{q}'\left\{e^{-i\bar{q}'\cdot(\bar{b}-\bar{s}/2)}\; A_n(\bar{q}')+e^{-i\bar{q}'\cdot(\bar{b}+\bar{s}/2)}\; A_p(\bar{q}')\right\}\right.$$

$$\left. - \frac{1}{(2\pi ik)^2}\int d^2\bar{q}'\, d^2q''\; A_n(\bar{q}')\; A_p(\bar{q}'')\; e^{-i\bar{b}\cdot(\bar{q}'+\bar{q}'')}\; e^{i(\bar{q}'-\bar{q}'')\cdot\bar{s}/2}\right].$$

Integrating over $\bar{b}$ gives

$$A_{fi}(\bar{q}) = \int d^3\bar{r}\; \psi_f^*(\bar{r})\psi_i(\bar{r}) \quad x$$

$$x\left[\int d^2\bar{q}'\; \delta^2(\bar{q}-\bar{q}')\left\{A_n(\bar{q}')\; e^{i\bar{q}\cdot\bar{s}/2} + A_p(\bar{q}')\; e^{-i\bar{q}'\cdot\bar{s}/2}\right\}\right.$$

$$\left. - \frac{1}{2\pi ik}\int d^2\bar{q}'\; d^2\bar{q}''\; A_n(\bar{q}')\; A_p(\bar{q}'')\; \delta^2(\bar{q}-\bar{q}'-\bar{q}'')\; e^{i(\bar{q}'-\bar{q}'')\cdot\bar{s}/2}\right].$$

Integrating out the δ-functions gives

$$A_{fi}(\bar{q}) = \int d^3\bar{r}\; \psi_f^*(\bar{r})\psi_i(\bar{r})\left[A_n(\bar{q})\; e^{i\bar{q}\cdot\bar{s}/2} + A_p(\bar{q})\; e^{-i\bar{q}\cdot\bar{s}/2}\right.$$

$$\left. - \frac{1}{2\pi ik}\int d^2\bar{q}'\; A_n(\bar{q}')\; A_p(\bar{q}-\bar{q}')\; e^{i\bar{s}\cdot(\bar{q}'-\bar{q}/2)}\right] \qquad \text{(B-1)}$$

We let $\varphi_f(\bar{p})$ and $\varphi_i(\bar{p})$ be the Fourier transform of $\psi_f(\bar{r})$ and $\psi_i(\bar{r})$, respectively. Again using the small angle scattering approximation $\bar{q}\cdot\bar{s} \cong \bar{q}\cdot\bar{r}$, we can rewrite Eq. B-1 as

$$A_{fi}(\bar{q}) = \frac{1}{(2\pi)3}\int d^3\bar{p}\; d^3\bar{p}'\; \varphi_f^*(\bar{p})\varphi_i(\bar{p}') \int d^3\bar{r}\; e^{-i\bar{r}\cdot(\bar{p}-\bar{p}')} \quad x$$

$$x \left[A_n(\bar{q})\; e^{i\bar{r}\cdot\bar{q}/2} + A_p(\bar{q})\; e^{-i\bar{r}\cdot\bar{q}/2} \right.$$

$$\left. - \frac{1}{2\pi ik}\int d^2\bar{q}'\; A_n(\bar{q}')\; A_p(\bar{q}-\bar{q}')\; e^{i\bar{r}\cdot(\bar{q}'-\bar{q}/2)} \right] .$$

Integrating over $\bar{r}$ gives 3-dimensional δ-functions which can be used to do the $\bar{p}'$ integration. Carrying this out, we have

$$A_{fi}(\bar{q}) = A_n(\bar{q}) \int d^3\bar{p}\; \varphi_f^*(\bar{p})\varphi_i(\bar{p}-\bar{q}/2) + A_p(\bar{q}) \int d^3\bar{p}\; \varphi_f^*(\bar{p})\varphi_i(\bar{p}+\bar{q}/2)$$

$$+ \frac{i}{2\pi k}\int d^2\bar{q}'\; A_n(\bar{q}')\; A_p(\bar{q}-\bar{q}') \int d^3\bar{p}\; \varphi_f^*(\bar{p})\varphi_i(\bar{p}-\bar{q}'-\bar{q}/2) \quad . \tag{B-2}$$

We define the overlap integral

$$G_{fi}(\bar{q}) = \int d^3\bar{p}\; \varphi_f^*(\bar{p})\; \varphi_i(\bar{p}-\bar{q}) \quad .$$

Then Eq. B-2, with a change of variables $\bar{q}'' = \bar{q}'-\bar{q}/2$, can be written as

$$A_{fi}(\bar{q}) = G_{fi}(\bar{q}/2)\; A_n(\bar{q}) + G_{fi}(-\bar{q}/2)\; A_p(\bar{q})$$

$$+ \frac{i}{2\pi k}\int d^2\bar{q}''\; G_{fi}(\bar{q}'')\; A_n(\bar{q}''+\bar{q}/2)\; A_p(-\bar{q}''+\bar{q}/2) \quad . \tag{B-3}$$

APPENDIX C

We derive in this Appendix the generalizations of Eqs. III-12, III-13, and III-18 to include spin dependence. Our starting point is Eq. III-9. We assume that the K^-d amplitude has the form

$$A_{fi}(\bar{q}) = M_1 + M_2 \quad ,$$

where

$$M_1 = G_{fi}(\bar{q}/2)\, A_n(\bar{q}) + G_{fi}(-\bar{q}/2)\, A_p(\bar{q}) \tag{C-1}$$

$$M_2 = \frac{i}{2\pi k}\int d^2\bar{q}'\; G_{fi}(\bar{q}')\, A_n(\bar{q}_+)\, A_p(\bar{q}_-) \; . \tag{C-2}$$

Here we have defined $\bar{q}_\pm = \pm\bar{q}' + \bar{q}/2$. The spin dependence of the nucleon amplitudes is assume to be

$$A_j(\bar{q}) = f_j(\bar{q}) + i\bar{\sigma}_j\cdot\hat{n}_q\, g_j(\bar{q}) \; , \qquad j = n,p$$

where $\hat{n}_q = \dfrac{\bar{k}_i x \bar{q}}{|\bar{k}_i x \bar{q}|}$ is the unit normal to the scattering plane defined by the incident momentum $\bar{k}_i$ and the momentum transfer vector $\bar{q}$. We use a hermitean representation for the Pauli matrices $\bar{\sigma}_j$. Each $\bar{\sigma}_j$ (for j=n,p) satisfy the two relations

$$\begin{aligned} &1) \quad [\sigma^\alpha, \sigma^\beta] = 2i\epsilon_{\alpha\beta\gamma}\sigma^\gamma \\ &2) \quad \sigma^\alpha\sigma^\beta = \delta_{\alpha\beta} + i\epsilon_{\alpha\beta\gamma}\sigma^\gamma \; . \end{aligned} \tag{C-3}$$

$\epsilon_{\alpha\beta\gamma}$ is the completely anti-symmetric tensor of rank 3. We use the convention that all Greek indices run from 1 to 3, and repeated Greek indices are summed over this range. From these two relations we get

$$\mathrm{Tr}\left[\sigma^{\alpha}\right] = 0$$

$$\mathrm{Tr}\left[\sigma^{\alpha}\sigma^{\beta}\right] = 2\delta_{\alpha\beta} \qquad \text{(C-4)}$$

$$\mathrm{Tr}\left[\sigma^{\alpha}\sigma^{\beta}\sigma^{\gamma}\right] = 2i\epsilon_{\alpha\beta\gamma} \quad .$$

The following relations are also needed;

$$\epsilon_{\alpha\beta\gamma}\ \epsilon_{\alpha\lambda\mu} = \delta_{\beta\lambda}\ \delta_{\gamma\mu} - \delta_{\beta\mu}\ \delta_{\gamma\lambda}$$

$$\epsilon_{\alpha\mu\nu}\ \epsilon_{\lambda\beta\mu}\ \epsilon_{\lambda\gamma\nu} = \epsilon_{\alpha\beta\gamma} \qquad \text{(C-5)}$$

$$\epsilon_{\alpha\beta\mu}\ \epsilon_{\alpha\beta\nu} = 2\delta_{\mu\nu} \ .$$

1. Elastic Scattering

We consider first elastic scattering. The cross-section is given by Eq. III-29 (we take f=i),

$$\left(\frac{d\sigma}{d\Omega}\right)_{el} = \frac{1}{3}\mathrm{Tr}\left[P_3 A^{+}_{ii}(\bar{q})\ P_3\ A_{ii}(\bar{q})\right]$$

$$= \frac{1}{3}\mathrm{Tr}\ (P_3 M_1 P_3 M_1) + \frac{2}{3}\ \mathrm{Re}\ \mathrm{Tr}(P_3 M_1^{+} P_3 M_2) + \frac{1}{3}\mathrm{Tr}(P_3 M_2^{+} P_3 M_2). \qquad \text{(C-6)}$$

The first term of this equation is the single scattering contribution. The second is the interference between single and double scattering. The third term is due purely to double scattering. We evaluate first the single scattering term

$$\left(\frac{d\sigma}{d\Omega}\right)^{S}_{el} = \frac{1}{3}\mathrm{Tr}\ (P_3 M_1^{+} P_3 M_1) \quad .$$

Using the hermitean conjugate of Eq. C-1, we can show that the commutator

$$\left[M_1^{+}, P_3\right] = \frac{1}{2}\left(g_n^{*} - g_p^{*}\right)\ \epsilon_{\alpha\beta\gamma}\ n_q^{\alpha}\ \sigma_p^{\beta}\ \sigma_n^{\gamma} \quad . \qquad \text{(C-7)}$$

We use the following short-hand notation:

$$f_n = G(\bar{q}/2)\, f_n(\bar{q}) \quad , \qquad f_p = G(-\bar{q}/2)\, f_p(\bar{q})$$
$$g_n = G(\bar{q}/2)\, g_n(\bar{q}) \quad , \qquad g_p = G(-\bar{q}/2)\, g_p(\bar{q}) \quad . \tag{C-8}$$

where $G(\bar{q}) = G_{ii}(\bar{q})$ is the deuteron form factor. We have used this notation in Eq. C-7. The asterisk appearing in this equation denote complex conjugation. We note also that a projection operator satisfy $P_3^2 = P_3$. Using this fact and Eq. C-7, we can write

$$\mathrm{Tr}(P_3 M_1^+ P_3 M_1) = \mathrm{Tr}(P_3 M_1^+ M_1) + \frac{g_n^* - g_p^*}{2} \epsilon_{\alpha\beta\gamma} n_q^\alpha \, \mathrm{Tr}(P_3 \sigma_p^\beta \sigma_n^\gamma M_1) \quad .$$

Using the relations given in Eqs. C-3, C-4, and C-5, we can show that

$$\frac{g_n^* - g_p^*}{2} \epsilon_{\alpha\beta\gamma} n_q^\alpha \, \mathrm{Tr}(P_3 \sigma_p^\beta \sigma_n^\gamma M_1) = -|g_n - g_p|^2 \quad . \tag{C-9}$$

With a similar procedure, we can show that

$$\mathrm{Tr}(P_3 M_1^+ M_1) = 3\,(|f_n + f_p|^2 + |g_n|^2 + |g_p|^2) + g_n^* g_p + g_n g_p^* \tag{C-10}$$

Adding Eqs. C-9 and C-10 yields the single scattering cross-section

$$\left(\frac{d\sigma}{d\Omega}\right)_{el}^{S} = |f_n + f_p|^2 + \frac{2}{3}\,|g_n + g_p|^2 \quad .$$

Written out explicitly, using the fact that $G(\bar{q}/2) = G(-\bar{q}/2)$, this equation becomes

$$\left(\frac{d\sigma}{d\Omega}\right)_{el}^{S} = G^2(\bar{q}/2) \left[|f_n(\bar{q}) + f_p(\bar{q})|^2 + \frac{2}{3}\,|g_n(\bar{q}) + g_p(\bar{q})|^2 \right] . \tag{C-11}$$

The interference between the single and double scattering is given

by the second term of Eq. C-6. We denote this term by

$$\left(\frac{d\sigma}{d\Omega}\right)_{el}^{SD} = \frac{2}{3}\,\mathrm{Re}\,\mathrm{Tr}(P_3 M_1^+ P_3 M_2) \quad . \tag{C-12}$$

Again we write, using Eq. C-8 and $P_3^{\,2} = P_3$,

$$\mathrm{Tr}(P_3 M_1^+ P_3 M_2) = \mathrm{Tr}(P_3 M_1^+ M_2) + \frac{(g_n^* - g_p^*)}{2}\,\epsilon_{\alpha\beta\gamma} n_q^{\alpha}\,\mathrm{Tr}(P_3 \sigma_p^{\beta}\sigma_n^{\gamma} M_2) \quad .$$

Evaluating the second term of this equation gives

$$\begin{aligned}\frac{(g_n^* - g_p^*)}{2}\,\epsilon_{\alpha\beta\gamma} n_q^{\alpha}\,\mathrm{Tr}(P_3\sigma_p^{\beta}\sigma_n^{\gamma}M_2) &= \frac{i}{2\pi k}\int d^2\bar{q}'\; G(\bar{q}')\;(g_n^* - g_p^*)\;\; x \\ x\Big[\, g_p(\bar{q}_-)\, f_n(\bar{q}_+)\, \hat{n}_q\cdot\hat{n}_{q_-} &- g_n(\bar{q}_+) f_p(\bar{q}_-)\hat{n}_q\cdot\hat{n}_{q_+} \\ + g_n(\bar{q}_+) g_p(\bar{q}_-)\hat{n}_q\cdot(\hat{n}_{q_+} x \hat{n}_{q_-})\Big] &\quad .\end{aligned} \tag{C-13}$$

Evaluating the first term gives

$$\begin{aligned}\mathrm{Tr}(P_3 M_1^+ M_2) = \frac{i}{2\pi k}\int d^2\bar{q}'\; G(\bar{q}')\Big[(f_n^* + f_p^*)\Big\{3 f_n(\bar{q}_+) f_p(\bar{q}_-) - g_n(\bar{q}_+) g_p(\bar{q}_-)\hat{n}_{q_+}\cdot\hat{n}_{q_-}\Big\} \\ + (3g_n^* + g_p^*) g_n(\bar{q}_+) f_p(\bar{q}_-)\hat{n}_q\cdot\hat{n}_{q_+} + (g_n^* + 3g_p^*) g_p(\bar{q}_-) f_n(\bar{q}_+)\hat{n}_q\cdot\hat{n}_{q_-} \\ - (g_n^* - g_p^*) g_n(\bar{q}_+) g_p(\bar{q}_-)\hat{n}_q\cdot(\hat{n}_{q_+} x \hat{n}_{q_-})\Big] .\end{aligned} \tag{C-14}$$

From Eqs. C-12, C-13, and C-14, we get the single and double-scattering interference contribution to the elastic scattering cross-section

$$\left(\frac{d\sigma}{d\Omega}\right)_{el}^{SD} = -\frac{G(\bar{q}/2)}{\pi k}\,\mathrm{Im}\int d^2\bar{q}'\, G(\bar{q}')\, M_{np}(\bar{q},\bar{q}') \quad , \tag{C-15}$$

where

$$\begin{aligned} M_{np} = (f_n^*(\bar{q}) + f_p^*(\bar{q}))\Big\{ f_n(\bar{q}_+) f_p(\bar{q}_-) - \frac{1}{3}\, g_n(\bar{q}_+) g_p(\bar{q}_-)\hat{n}_{q_+}\cdot\hat{n}_{q_-}\Big\} \\ + \frac{2}{3}\,(g_n^*(\bar{q}) + g_p^*(\bar{q}))\Big\{ g_n(\bar{q}_+) f_p(\bar{q}_-)\hat{n}_q\cdot\hat{n}_{q_+} + g_p(\bar{q}_-) f_n(\bar{q}_+)\hat{n}_q\cdot\hat{n}_{q_-}\Big\} \end{aligned}$$

2. Deuteron Break-up

The break-up reaction cross-section is given by Eq. III-33,

$$\left(\frac{d\sigma}{d\Omega}\right)_{Kpn} = \sum_f \frac{1}{3} \mathrm{Tr}\left[P_3 A^+_{fi}(\bar{q})\, A_{fi}(\bar{q})\right] \qquad (C\text{-}16)$$

$$= \frac{1}{3} \sum_f \mathrm{Tr}(P_3 M_1 M_1) + \frac{2}{3} \mathrm{Re} \sum_f \mathrm{Tr}(P_3 M_1^+ M_2) + \frac{1}{3} \sum_f \mathrm{Tr}(P_3 M_2^+ M_2) \ .$$

Again the three terms on the right correspond to single scattering, interference between single and double scattering, and pure double scattering, respectively. We denote the single scattering term by

$$\left(\frac{d\sigma}{d\Omega}\right)^S_{Kpn} = \frac{1}{3} \sum_f \mathrm{Tr}(P_3 M_1^+ M_1) \ . \qquad (C\text{-}17)$$

The spin structure of this equation is the same as Eq. C-10. However, rather than Eq. C-8, the amplitudes f_n, g_n, f_p, and g_p should be defined in the present case by

$$f_n = G_{fi}(\bar{q}/2)\, f_n(\bar{q}), \quad f_p = G_{fi}(-\bar{q}/2)\, f_p(\bar{q})$$

$$g_n = G_{fi}(\bar{q}/2)\, g_n(\bar{q}), \quad g_p = G_{fi}(-\bar{q}/2)\, g_p(\bar{q})$$

Hence, reading off from Eq. C-10, Eq. C-17 becomes explicitly

$$\left(\frac{d\sigma}{d\Omega}\right)^S_{Kpn} = (|f_n(\bar{q})|^2 + |g_n(\bar{q})|^2) \sum_f G^*_{fi}(\bar{q}/2)\, G_{fi}(\bar{q}/2)$$

$$+ (|f_p(\bar{q})|^2 + |g_p(\bar{q})|^2) \sum_f G^*_{fi}(-\bar{q}/2)\, G_{fi}(-\bar{q}/2) \qquad (C\text{-}18)$$

$$+ 2\mathrm{Re}\left[f_n(\bar{q}) f_p^*(\bar{q}) + \frac{1}{3} g_n(\bar{q}) g_p^*(\bar{q})\right] \sum_f G^*_{fi}(\bar{q}/2)\, G_{fi}(-\bar{q}/2).$$

Using the closure approximation, we have from Eq. III-17

$$\sum_f G^*_{fi}(\bar{q}/2)\, G_{fi}(\bar{q}/2) = \sum_f G^*_{fi}(-\bar{q}/2)\, G_{fi}(-\bar{q}/2) = G(0)$$

$$\sum_f G^*_{fi}(\bar{q}/2)\, G_{fi}(-\bar{q}/2) = G(\bar{q})$$

where $G(\bar{q})$ is the deuteron form factor. Thus Eq. C-18 can be re-written as

$$\left(\frac{d\sigma}{d\Omega}\right)^S_{Kpn} = G(0)\left[|f_n(\bar{q})|^2+|g_n(\bar{q})|^2\right] + G(0)\left[|f_p(\bar{q})|^2+|g_p(\bar{q})|^2\right] + 2G(\bar{q})\ \mathrm{Re}\left[f_n(\bar{q})f^*_p(\bar{q}) + \frac{1}{3}g_n(\bar{q})g^*_p(\bar{q})\right] \quad \text{(C-19)}$$

The first bracket in this equation arises from neutron single scattering, the second from proton single scattering, and the third from their interference.

Next we consider the second term of Eq. C-16. This is the interference between single and double scattering amplitudes. We denote this by

$$\left(\frac{d\sigma}{d\Omega}\right)^{SD}_{Kpn} = \frac{2}{3}\,\mathrm{Re}\sum_f \mathrm{Tr}(P_3 M_1^+ M_2) \quad \text{(C-20)}$$

Again we note that the spin structure of this equation is the same as Eq. C-14. In this case, we have to replace each $G(\bar{q})$ in Eq. C-14 by $G_{fi}(\bar{q})$. We get for the cross-section explicitly

$$\left(\frac{d\sigma}{d\Omega}\right)^{SD}_{Kpn} = -\frac{1}{\pi k}\,\mathrm{Im}\int d^2\bar{q}'\left[M_n(\bar{q},\bar{q}')\sum_f G^*_{fi}(\bar{q}/2)G_{fi}(\bar{q}') + M_p(\bar{q},\bar{q}')\sum_f G^*_{fi}(-\bar{q}/2)G_{fi}(\bar{q}')\right] \quad \text{(C-21)}$$

where $M_n(\bar{q},\bar{q}')$ and $M_p(\bar{q},\bar{q}')$ are defined by

$$M_n(\bar{q},\bar{q}') = f_n^*(\bar{q})\left[f_n(\bar{q}_+)f_p(\bar{q}_-) - \frac{1}{3}\, g_n(\bar{q}_+)g_p(\bar{q}_-)\hat{n}_{q_+}\cdot\hat{n}_{q_-}\right]$$

$$+g_n^*(\bar{q})\left[g_n(\bar{q}_+)f_p(\bar{q}_-)\hat{n}_q\cdot\hat{n}_{q_+} + \frac{1}{3}\, g_p(\bar{q}_-)f_n(\bar{q}_+)\hat{n}_q\cdot\hat{n}_{q_-}\right.$$

$$\left. + \frac{1}{3}\, g_n(\bar{q}_+)g_p(\bar{q}_-)\hat{n}_q\cdot(\hat{n}_{q_-}\times\hat{n}_{q_+})\right]$$

$$M_p(\bar{q},\bar{q}') = f_p^*(\bar{q})\left[f_n(\bar{q}_+)f_p(\bar{q}_-) - \frac{1}{3}\, g_n(\bar{q}_+)g_p(\bar{q}_-)\hat{n}_{q_+}\cdot\hat{n}_{q_-}\right]$$

$$+g_p^*(\bar{q})\left[g_p(\bar{q}_-)f_n(\bar{q}_+)\hat{n}_q\cdot\hat{n}_{q_-} + \frac{1}{3}\, g_n(\bar{q}_+)f_p(\bar{q}_-)\hat{n}_q\cdot\hat{n}_{q_+}\right.$$

$$\left. + \frac{1}{3}\, g_n(\bar{q}_+)g_p(\bar{q}_-)\hat{n}_q\cdot(\hat{n}_{q_+}\times\hat{n}_{q_-})\right] .$$

With the closure approximation relations, we can rewrite Eq. C-21 as

$$\left(\frac{d\sigma}{d\Omega}\right)^{SD}_{Kpn} = -\frac{1}{\pi k}\,\mathrm{Im}\int d^2\bar{q}'\left[G(\bar{q}_-)M_n(\bar{q},\bar{q}') + G(\bar{q}_+)M_p(\bar{q},\bar{q}')\right] \qquad \text{(C-22)}$$

3. Cross-Section Defect

The K^-d total cross-section is given by Eq. III-31,

$$\sigma_d = \frac{4\pi}{k}\,\mathrm{Im}\,\frac{1}{3}\,\mathrm{Tr}(P_3 A_{ii}(0)) \quad .$$

From Eq. C-1 and C-2 we get

$$\sigma_d = \sigma_n + \sigma_p - d\sigma \quad ,$$

where

$$d\sigma = \frac{4\pi}{k}\,\mathrm{Im}\,\frac{1}{3}\,\mathrm{Tr}(P_3 M_2(0)) \quad . \qquad \text{(C-23)}$$

From Eq. C-2

$$\mathrm{Tr}(P_3 M_2(0)) = \frac{-i}{2\pi k}\int d^2\bar{q}\; G(\bar{q})\;\mathrm{Tr}\left[P_3 A_n(\bar{q})\; A_p(-\bar{q})\right] \quad .$$

Using the techniques described above, we get

$$\mathrm{Tr}\left[P_3 A_n(\bar{q})\; A_p(-\bar{q})\right] = 3\left[f_n(\bar{q})f_p(-\bar{q}) - \hat{n}_{\bar{q}}\cdot\hat{n}_{-\bar{q}}\; g_n(\bar{q})g_p(-\bar{q})\right] .$$

Since $\hat{n}_{-\bar{q}} = -\hat{n}_{\bar{q}}$, we finally get for Eq. C-23

$$d\sigma = -\frac{2}{k^2}\int d^2\bar{q}\; G(\bar{q})\; \mathrm{Re}\left[f_n(\bar{q}) f_p(-\bar{q}) + \frac{1}{3}\, g_n(\bar{q}) g_p(-\bar{q}) \right]. \qquad \text{(C-24)}$$

ACKNOWLEDGMENTS

I thank Dr. George Kalmus for his guidance and support throughout the course of this work. The comments and advice of Professor Robert Poe have been invaluable. To Drs. James Louie, Jack Sahouria, and Wesley Smart I owe much for their help in the early part of this experiment. To the many members of the Powell-Birge group who helped with this experiment, I express my thanks. I especially appreciate the patience and skill with which Mrs. Sandy Paciotti and Mrs. Jane Kennedy typed this thesis.

This work was done under the auspices of the U.S. Atomic Energy Commission.

REFERENCES

1. R. B. Bell, R. W. Bland, M. G. Bowler, J. L. Brown, R. P. Ely, S. Y. Fung, G. Goldhaber, A. A. Hirata, J. A. Kadyk, J. Louie, C. T. Murphy, J. S. Sahouria, V. H. Seeger, W. M. Smart, and G. H. Trilling, A Variable Momentum Separated $K^{\pm}$ Beam at the Bevatron, UCRL-11527, 1964.

2. H. C. Albrecht, E. P. Binnall, R. W. Birge, M. H. Meyers and P. W. Weber, The COBWEB Data Reduction System, UCRL-18528 (Rev.), 1968.

3. H. S. White, S. S. Buckman, D. E. Hall, E. Hurwitz, L. B. Meissner, J. C. Smith, and F. R. Stannard, The FOG, CLOUDY, and FAIR Programs for Bubble Chamber Data Reduction, UCRL-9457, 1960.

4. J. Louie and J. S. Sahouria, P-B Group (LRL) Note PB-104-2, (April 1967).

5. B. Rossi, High Energy Particles, Prentice-Hall (1952), Ch. 2; F. Crawford, Use of Delta-Rays to Determine Particle Velocities, LRL, UCID-241 (1957).

6. D. V. Bugg, R. S. Gilmore, K. M. Knight, D. C. Salter, G. H. Stafford, E. J. N. Wilson, J. D. Davies, J. D. Dowell, P. M. Hattersley, R. J. Homes, A. W. O'Dell, A. A. Carter, R. J. Tapper, and K. F. Riley, Phys. Rev. 168, 1466 (1968).

7. J. L. Brown, Theoretical Index of Refraction in Various Hydrogen/Deuterium Experiments, LRL, Trilling-Goldhaber Technical Note TGT-29 (Oct. 1964).

8. W. M. Smart, Study of the Y_1^* Resonant Amplitudes Between 1660 and 1900 MeV in the Reaction $K^-n \rightarrow \Lambda\pi^-$, UCRL-17712 (Aug. 1967).

9. S. E. Derenzo and R. H. Hildebrand, The Estimation of Scanning Efficiencies for Experiments Using Visual Detectors, UCRL-18638 (Dec. 1968).

10. R. J. Glauber, in Lectures in Theoretical Physics, edited by W. E. Britten et. al, (Interscience Publishers, Inc., New York, 1959), Vol. I, pg. 315.

11. V. Franco and R. J. Glauber, Phys. Rev. 142, 1195 (1966).

12. C. Wilkin, High Energy Scattering from Nuclei, Brookhaven National Laboratory, BNL-11722 (1967).

13. T. Adachi and T. Kotani, Prog. of Theo. Phys. 39, 785 (1968), and references therein.

14. L. D. Landau and E. M. Lifshitz, Quantum Mechanics - Non-Relativistic Theory, (Pergamon Press, New York, 1965), pg. 19.

15. E. S. Abers, H. Burkhardt, V. L. Teplitz, and C. Wilkin, Nuovo Cimento 42, 365 (1966).

16. L. Bertocchi and A. Capella, Nuovo Cimento 51, 369 (1967).

17. G. Källén, Elementary Particle Physics (Addison-Wesley Publishing Co., Inc. 1964), Chapters 1 and 3.

18. E. Byckling and K. Kajamtie, Nucl. Phys. 39, 568 (1969); P. P. Srivastava and G. Sudarshan, Phys. Rev. 110, 756 (1958).

19. Chapter 3 of Ref. 17.

20. For a detailed discussion of this relation, see Ref. 16.

21. G. Fäldt and T. E. O. Ericson, Nucl. Phys. B8, 1 (1968).

22. M. J. Moravcsik, Nucl. Phys. 7, 113 (1958).

23. T. Lasinski, R. Levi-Setti, and E. Predazzi, Phys. Rev. 163, 1792 (1967).

24. R. Armenteros, P. Baillon, C. Breiman, M. Ferro-Luzzi, D. E. Plane, N. Schnitz, E. Burkhardt, H. Filthuth, E. Kluge, H. Oberlack, R. R. Ross, R. Barloutaud, P. Granet, J. Meyer, J. P. Porter, and J. Prevost, Nucl. Phys. B8, 195 (1968).

25. W. R. Holley, E. F. Beall, D. Keefe, L. T. Kerth, J. J. Thresher, C. L. Wang, and W. A. Wenzel, Phys. Rev. 154, 1273 (1967).

26. J. M. Blatt and V. F. Weisskopf, Theoretical Nuclear Physics, (John Wiley and Sons, New York, 1952), pg. 361.

27. W. A. Ross and D. W. G. S. Leith, A Simple Model of $\pi^- p$ Elastic Scattering Near 1 GeV/c, Stanford Linear Accelerator, SLAC-PUB-430 (1968).

28. M. Musette, Nucl. Phys. B4, 131 (1967). This is a special case of the general expansion considered in this reference. The choice of g_b being proportional to $\sqrt{-t}$ corresponds to having the spin-flip potential being proportional to $\bar{\sigma}\cdot\bar{L}$ in potential scattering. (See Ref. 30.)

29. N. Barash-Schmidt, G. Conforte, A. Barbaro-Galtieri, L. R. Price, M. Roos, A. H. Rosenfeld, P. Soding, and C. G. Wohl, Review of Particle Properties, UCRL-8030 (Jan. 1969).

30. N. Byers and C. N. Yang, Phys. Rev. 142, 476 (1966).

31. E. R. Beals, ZO BKY VARMIT, Lawrence Radiation Laboratory Computer Center Library Note, June 1966 (unpublished).

32. W. C. Davidon, Variable Metric Method for Minimization, Argonne National Laboratory Report ANL-5990 Rev., Nov. 1959 (unpublished).

33. See for example, Figs. 4 and 5 of Ref. 11.

34. R. Levi-Setti, Strange Baryon Resonances, Univ. of Chicago, Preprint EFI 69-78 (June, 1969). Rapporteur talk given at the Lund International Conference on Elementary Particles in Lund, Sweden.

TECHNICAL INFORMATION DIVISION
LAWRENCE RADIATION LABORATORY
UNIVERSITY OF CALIFORNIA
BERKELEY, CALIFORNIA 94720